University of Massachusetts Amherst

ScholarWorks@UMass Amherst

Doctoral Dissertations

Dissertations and Theses

October 2019

Top-Down and Bottom-Up Fabrication of Key Components in Miniature Energy Storage Devices

Wenhao Li

Recommended Citation

TOP-DOWN AND BOTTOM-UP FABRICATION OF KEY COMPONENTS IN MINIATURE
ENERGY STORAGE DEVICES

A Dissertation Presented

by

WENHAO LI

Submitted to the Graduate School of the

University of Massachusetts Amherst in partial fulfillment

of the requirements for the degree of

DOCTOR OF PHILOSOPHY

September 2019

Polymer Science and Engineering

**TOP-DOWN AND BOTTOM-UP FABRICATION OF KEY COMPONENTS IN
MINIATURE ENERGY STORAGE DEVICES**

A Dissertation Presented

by

WENHAO LI

Approved as to style and content by:

_____

James J. Watkins, Chair

_____

E. Bryan Coughlin, Member

_____

Dhandapani Venkataraman, Member

                                        _____

                                        E. Bryan Coughlin, Department Head

                                        Polymer Science and Engineering

DEDICATION

To the new adventure.

ACKNOWLEDGEMENTS

First and foremost, I would like to express my sincere gratitude to my Ph.D. advisor, Prof. James Watkins. Jim's guidance and encouragement made me a confident independent researcher. He gave me the freedom to nucleate my own research ideas, to contact any possible collaborator and to attend every relevant academic conference. I clearly remember our first meeting in 2014 when I was still at the phase of advisor selection. Jim drew on the white board a J-shaped curve, showing his expected correlation of a student's academic growth vs. time; an exponential growth appears after a certain turning point. Jim offered me the patience to learn and to accumulate knowledge, and every bit of resource to advance that turning point. I feel extremely fortunate to have worked with Jim. Besides research, Jim's help with my professional development is also beyond words. He granted me opportunities to present to industrial collaborators, introduced me to his friends, and most recently, he supported me to do a research internship over the summer 2019. I cannot thank him more for all these helps!

I would like to thank my two wonderful Thesis Committee members, Prof. Bryan Coughlin and Prof. DV. I am grateful for their valuable questions and suggestions. As both of them are great chemists, they provided insights from a different perspective that substantially helped my thesis study. I would also like to thank Prof. Laura Bradley. Laura is my collaborator, but I have already treated her as the fourth member on my Committee. I cannot thank her more for willing to collaborate with me. I valued our collaboration so much and it was my gold story in every interview I had! I was grateful for her patience to sit together with me and went over our manuscript word by word, line by line. She shared

great opportunities and introduced me to the iCVD community. Laura also gave me incredible support and great care in my job searching. I sincerely appreciate her help!

Over these years, I was lucky to have collaborated with many world-class scientists. I would like to thank Prof. Bo Iversen from Aarhus University and his student Troels Christiansen. Their hard work made the microbattery project possible. I met Prof. Bo twice in person. His advice and warm encouragement really helped me and the collaboration. Within the Watkins group, we had strong and active collaborations and great friendships, and I would like to thank all previous and current group members: Dr. Nick Colella, Dr. Rohit Kothari, Dr. Cheng Li, Dr. Shengkai Li, Dr. Irene Howell, Dr. Feyza Dunder, Dr. Yue Gai, Dr. Aditi Naik, Dr. Ben Yavitt, Dr. Yiliang Zhou, Dr. Dong-po Song, Dr. Hua-feng Fei, Dr. Janghoon Park, Dr. Jacobo Morere, Dr. David Leonardo Gonzales-Arellano, Gayathri Kopanati, Xiyu Hu, Vince Einck, Sravya Nuguri, Hsin-Jung (Hana) Yu, Ayush Bharjwaj, Atushi Ikoma, Dr. Uzo Okoroanyanwu and Dr. Yuying Tang. I would like to give special thanks to: Cheng- for being my first mentor, showing me experiments and laying a good foundation for my future research; Irene and Yue- for being wonderful office mates and for helping me with the first manuscript in my life; Aditi and Feyza- for giving me incredible advice for job searching and continuing to help me even after their graduation; Yiliang- for making me think independently and constantly questioning my ideas; He is arguably the most influential person in my Ph.D. time after Jim; Dong-po- for setting an excellent example; Huafeng- for all the in-depth discussions and his contagious passion for science; Janghoon- for the friendship, encouragement and help in both research and career.

I would like to thank the NSF Center of Hierarchical Manufacturing (CHM) and the Army Research Laboratory (ARL) for providing funding for my research studies. I

ABSTRACT

TOP-DOWN AND BOTTOM-UP FABRICATION OF KEY COMPONENTS IN
MINIATURE ENERGY STORAGE DEVICES

SEPTEMBER 2019

WENHAO LI, B.S., TSINGHUA UNIVERSITY

M.S., UNIVERSITY OF MASSACHUSETTS AMHERST

Ph.D., UNIVERSITY OF MASSACHUSETTS AMHERST

Directed by: Professor JAMES J. WATKINS

The advent of miniature electronic devices demands power sources of commensurate form factors. This spurs the research of micro energy storage devices, *e.g.*, 3D microbatteries. A 3D microbattery contains nonplanar microelectrodes with high aspect ratio and high surface area, separated by a nanoscale electrolyte. The device takes up a total volume as small as 10 mm^3, allowing it to serve on a chip and to provide power *in-situ*. The marriage of nanotechnology and electrochemical energy storage makes microbattery research a fascinating field with both scientific excitement and application prospect. However, successful fabrication of well-functioned key components and the assembly of them require careful choice of both materials and processing technologies, which explains the rarity of reports on fully assembled 3D microbattery devices. In this Thesis, we

exploited both top-down and bottom-up methods to produce nanostructured functional materials as either microelectrodes or nanoscale electrolytes.

Project 1 introduces nanoimprinting as a promising strategy toward scalable fabrication of woodpile-like 3D microelectrodes out of well-dispersed TiO_2 nanoparticles. Using sequential imprinting, we created electrode structures with different aspect ratios and correlated them to the improved charge storage capacity. One step forward, we applied imprinting to other electrode materials. In Project 2, we imprinted microelectrode using customized, ultrafine $LiMn_2O_4$ (LMO) and $Li_4Ti_5O_{12}$ (LTO) nanoparticles. A dopamine-containing copolymer electrolyte was developed to enable the layer-by-layer assembly of microbattery full device. The synergistic effect of nanosized materials and micropatterning resulted in batteries with very high volumetric energy and power densities.

Project 3 explores using vapor phase chemistry to deposit copolymer thin films onto 3D nanostructures and subsequently doping the neat dielectric films into "shrink-wrap" electrolytes. Correlations between deposition parameters, copolymer composition and the resultant dielectric and conducting properties were built. In the last project, we harnessed the self-assembly of bottlebrush block copolymers to template phenolic resin precursor and obtained nanoporous carbon electrodes that show promising performance in electrostatic double layer capacitors (EDLCs). By mixing electroactive Fe_2O_3 nanoparticles into the precursors, the electrodes become high-capacity lithium-ion battery anodes and more importantly, the precursor can be imprinted and undergo rapid photothermal curing. The combination of bottom-up assembly, top-down patterning and rapid curing makes them attractive for a variety of applications.

TABLE OF CONTENTS

XI

LIST OF TABLES

LIST OF FIGURES

XIII

CHAPTER 1

INTRODUCTION

1.1 Microfabrication Technologies

Top-down and bottom-up methods are two major approaches of micro/nanostructure fabrication.[1-2] The top-down approach refers to subtractive processes-materials are removed by slicing or etching from the bulk to result in the intended shapes and dimensions. On the other hand, the bottom-up approach refers to the device "creating itself" by self-assembly. Over the years, both approaches have seen tremendous development. The following sections intend to give introduction on some of the top-down and bottom-up technologies that are applied in this Thesis study.

1.1.1 Soft Imprint Lithography

Fabrication of small structures in micro- and nanoscale is essential to modern science and plays a critical role in information technologies,[3] energy conversion and storage,[4-5] optics and display,[6] and biomedical researches.[7] Photolithography has long been the dominant lithographic technology in the realm. Nonetheless, some major disadvantages should be noted: 1) Complex facilities are required for high-energy radiation to produce ultrafine structures. 2) Patterning on nonplanar surfaces is not straightforward. 3) Photolithography is compatible with very limited chemistry, primarily confined to specific types of photoactive polymers called the photoresists. This adds complexity to the patterning of nanoscale functional materials. Moreover, scalability and cost should be taken into serious consideration as well. Gordon Moore, founder of Intel, suggested that the number of transistors on an integrated circuit (IC) would double every 18 months, known to public as Moore's Law.[8] It is less known however, that the cost associated with facilities

to enable miniaturization scales at a similar rate to the feature downscaling; this is sometimes referred to as Moore's second law.[6]

To circumvent these limitations, cost-effective, non-photolithographic microfabrication received extensive studies in the past two decades. Soft lithography appears to be a promising candidate, which includes microcontact printing,[9-10] microtransfer printing,[11-13] micromolding in capillaries (MIMIC),[14] replica molding,[15-16] etc. The word "soft" refers to the key component in all these techniques - an elastomeric stamp, or mold, that is used to transfer patterns to the substrates via contact or embossing, the latter one is also denoted as imprinting. The prototyping procedure of soft lithography is shown in Figure 1.1a, and the typical imprinting and MIMIC processes are illustrated in Figure 1.1b and Figure 1.1c.
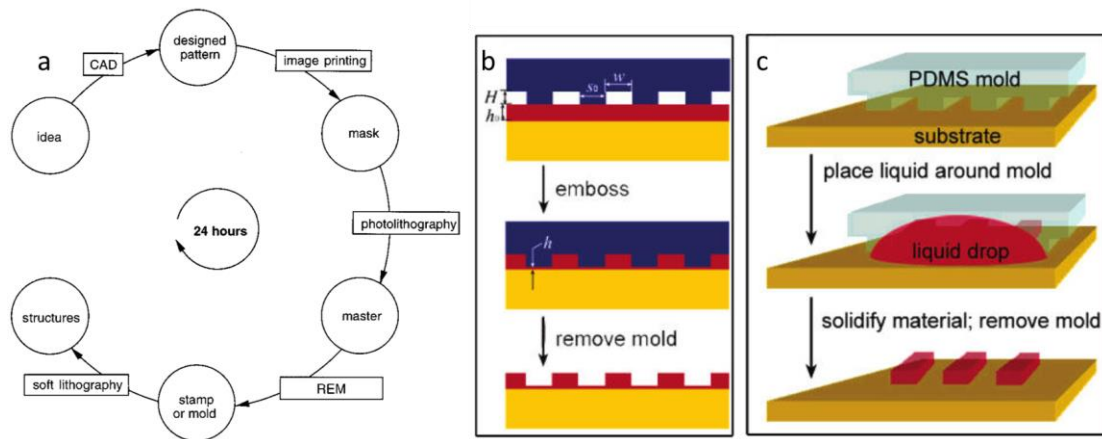
Figure 1.1 (a) prototyping workflow of a typical soft lithography process. (b) schematic illustration of nanoimprinting of polymer resins. (c) schematic illustration of MIMIC process. Reproduced from reference [6, 8].

Poly(dimethylsiloxane) (PDMS) is the most frequently used elastomer due to 1) low modulus for conformal contact on nonideal surfaces, like curved substrates; 2) low surface tension (~ 20 N m^{-1}) for easy demolding; 3) optical transparency to light wavelength down to 300 nm and 4) durability for tens of times of use. In this thesis study,

the approach we applied is called solvent-assisted imprint lithography, which is comparable to MIMIC in that functional materials in fluid (ink) fills the stamp by capillary flow, but different in that patterning starts from a continuous liquid film and that embossing is also included. We refer to some of the design principles used in MIMIC to guide our ink design, substrate modification and stamp surface treatment. Ink viscosity (η), surface energies (γ) at ink-stamp, ink-substrate interfaces and the stamp dimensions (x, y, z) play dominant roles in the capillary filling process. The feasibility and the rate of mold filling can be roughly described by Equations (1.1) and (1.2).[14]

$$\Delta G \cong -x\Delta z\gamma_{LV}(3\cos\theta + \cos\theta') \qquad (1.1)$$

$$\frac{dz}{dt} = \frac{R(\gamma_{SV} - \gamma_{SL})}{4\eta z} \qquad (1.2)$$

Here ΔG refers to the Gibbs free energy change of the mold filling process and θ, θ' are contact angles at the ink/PDMS and ink/substrate interfaces. R is the hydraulic ratio. It is obvious that in addition to formulate low viscosity inks, plasma or UV-ozone treatment to turn substrate more hydrophilic (decrease θ') is favorable. Although capillary flow rate decreases as channel dimensions in mold decrease from micro- to nanoscale range, combining capillary flow and embossing ensures full mold filling.

1.1.2 Initiated Chemical Vapor Deposition

Chemical vapor deposition (CVD) is a powerful method for surface engineering and has been extensively applied to deposit a variety of inorganic thin films onto substrates of interest.[17] The growth of high-quality films from a molecular level, and directly from the substrates, represents a bottom-up technique for microstructure fabrications. It is thus highly desirable to extend the technique to organic materials to fully capture the rich

3

chemistries of monomers. Compared to polymer thin films coating from solution phase, vapor phase chemistry offers notable advantages for depositing insoluble, crosslinked polymers with minimal residual impurities (like solvents). To date, CVD techniques for polymers can be classified based on the polymerization mechanism: step growth and chain growth polymerization. For step growth deposition, one famous example is parylene.[18] The self-initiated deposition results in dense films with controlled thicknesses, which have seen broad applications in dielectrics and packaging.[19-21] Oxidative CVD (oCVD) is another example, primarily used for conjugated polymer thin film deposition.[22] On the other hand, chain growth deposition includes plasma enhanced CVD (PECVD) and initiated CVD (iCVD);[23] the latter one is the focus of this thesis study.

As a free-radical polymerization method, iCVD comprises major kinetic steps of initiation, propagation and termination. Over the years, a variety of initiators have been successfully applied to the iCVD process, including tert-butyl peroxide (TBPO),[24] tert-amyl peroxide (TAPO),[25] perfluoro-octane sulfonyl fluoride (PFOS),[26] etc. The weak bonds, for example, the O-O bond in peroxides, can be readily cleaved to generate primary radicals. A typical iCVD chamber is shown in Figure 1.2. During deposition, a mixture vapor comprising the initiator and monomer (sometimes comonomers) flows into the vacuum chamber, passing through an array of metal filament, which is typically heated to 200-300 ℃ via Joule heating. Primary radicals generated by thermal decomposition of the initiator, together with the monomer will be physically absorbed onto a low temperature (ca. 20-70 ℃) sample stage and starts deposition (polymerization). Obviously, volatility is required for monomers, analogous to the solubility of monomers in solution polymerization. The most distinct feature of iCVD is the dual-phase reaction. It has been well documented

4

by Gleason and coworkers that thermal fragmentation of initiators takes place in the gas phase while chain propagation and termination occur almost exclusively on the substrate.[24, 27] This is because of the significant volatility, or saturated vapor pressure difference between initiator and monomer, resulting in high monomer concentration ([M]) only on the cooled sample stage. The decoupling of gas phase diffusion and surface reaction enables iCVD to generate conformal polymer films onto 2D and 3D substrates. Once the monomer is absorbed onto the sample stage, reaction kinetics can be well compared to the classical bulk polymerization; difference is that [M] is not determined by the feed in gas flow, but by the adsorption volume (V_{ad}) on substrate instead. Previous studies reveal that V_{ad} is dominated by a crucial parameter, P_M/P_{sat}, which is the monomer partial pressure over the saturated pressure at a given temperature. P_M/P_{sat} serves as the primary parameter to design and optimize new iCVD processes. Based on the discussion and equations above, it is easy to understand that metal filament temperature, monomer flow rate and the sample stage temperature all impact the deposition rate and the polymer molecular weight. For detailed investigation on iCVD kinetics, we direct the readers to the two foundation works by Lau and Gleason.[24, 27]
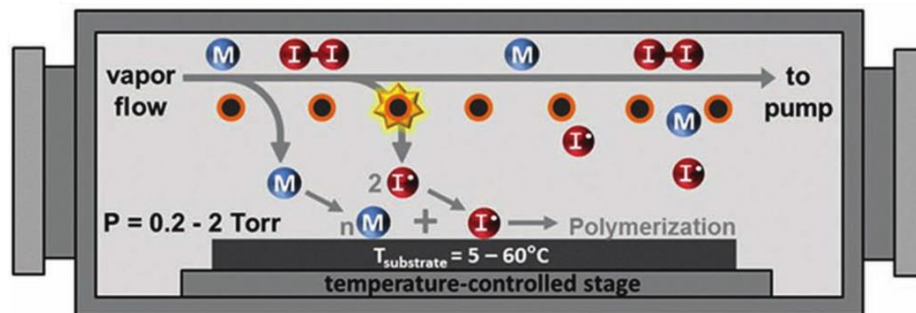
Figure 1.2 Schematic illustration of a typical iCVD chamber and operation parameters. Reproduced from reference [23].

1.1.3 Block Copolymer Templated Synthesis

Templated synthesis has seen great success in fabricating materials with ordered, hierarchical nanostructures and subsequent applications in separation,[28] catalysis,[11, 29] photonics,[30-31] and energy storage.[32-33] Templates can be classified into hard and soft types, depending on whether or not they have a predefined geometry.[34] For hard templates, inorganic materials like silica beads,[35] and organics like polystyrene colloids,[36] led to ordered porous materials with pore size covering the full spectrum of nanopores, from micro- (1-2 nm), meso-(2-50 nm) to macropores (50 nm and above). On the other hand, soft templates denote those without predefined geometries, but will self-assemble into well-defined nanostructures when mixing with the precursors of interest, representing an important bottom-up approach. Small molecule surfactants such as hexadecyl trimethylammonium bromide (CTAB) is amongst the most studied soft templates to fabricate microporous materials.[37] Besides, polymers, especially block copolymers (BCPs) are promising candidates, due to the rich library of available chemistries and morphologies.

Block copolymers are macromolecules containing two or more polymeric subunits (denoted as "blocks") with chemically distinct monomer sequences. The blocks are immiscible but covalently connected at one end, resulting in interesting microphase separation and rich nanoscale morphologies. Over the past two decades, morphological studies on block copolymers, especially linear BCPs, received great attention from both academia and industry.[38-41] Figure 1.3 summarizes the major morphologies of linear diblock copolymers. including lamellae, cylinders, spheres and gyroids, depending on the segregation strength (χN) and volume fraction (f) of the diblock copolymers.[42-43] It is highly desirable to harness the self-assembly of BCPs to fabricate ordered nanomaterials.

6

In general, the templating is facilitated by the favorable interaction, e.g. π-π conjugation and hydrogen bonding,[40, 44-46] between precursor and one block of BCPs. The result is that precursors primarily enter one domain with favorable interactions, forming controlled, uneven distribution in designated microphases. For example, poly(ethylene oxide) (PEO) has strong hydrogen bonding with hydrophilic precursors like phenol formaldehyde resin (or else "resol") and tetraethyl orthosilicate (TEOS).[32, 47-48] And thus using PEO containing diblock and triblock copolymers have been widely used to obtain hybrid precursors with resol and TEOS selectively distributed in PEO domain, leading to porous and gyroidal carbon and silica upon pyrolysis.
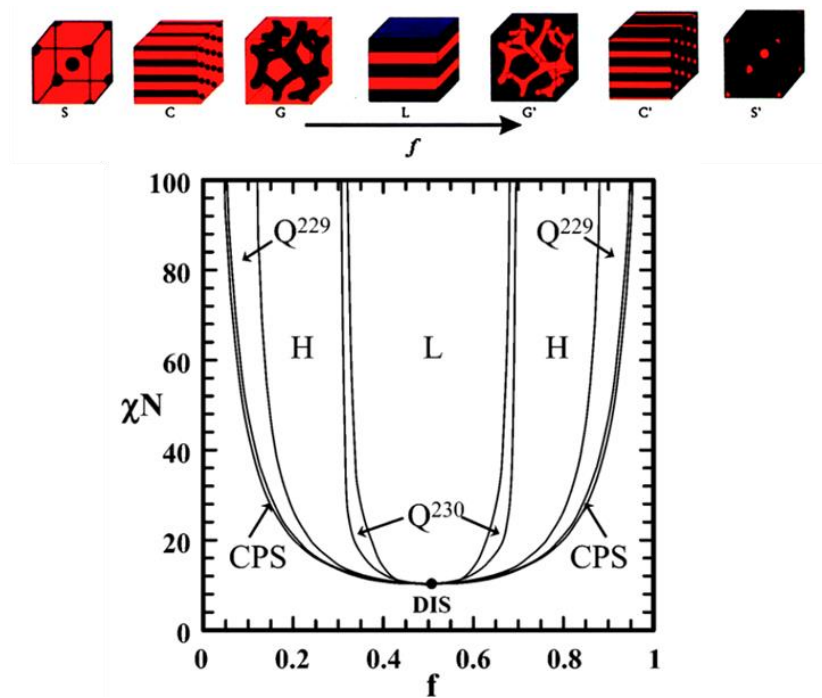
Figure 1.3 Theoretical phase diagram of diblock copolymers. Reproduced from reference [42-43].

In addition to linear BCPs, other polymer architectures are also actively studied, among which the bottlebrush block copolymers (BBCPs) received great attention in recent years. BBCPs are comb-like macromolecules with densely grafted polymeric side chains

7

of distinct chemical functionalities. These polymers are typically synthesized by ring opening metathesis polymerization (ROMP) of norbornene based macromonomers.[49-51] The synthetic strategy readily generates BBCPs with much higher molecular weight (M_w) than the linear analogs, which makes BBCPs promising soft templates for functional materials with larger feature size beyond 100 nm. Another distinct feature is their significantly reduced chain entanglements due to the stretched backbones conformation, leading to lower energy barriers for structural reorganization and rapid self-assembly. Previously, our group has demonstrated a series of works on using BBCPs for rapid templating resol,[52] polyhedral oligomeric silsesquioxane (POSS),[53] and functional nanoparticles (ZrO_2, CdSe, Au, etc).[44, 54-56] These works laid the foundation for this thesis study and holds potential for large scale continuous manufacturing, like the Roll-to-Roll (R2R) manufacturing.

1.2 Miniature Electrochemical Energy Storage

Electrochemical energy storage holds great promise as a clean alternative to fossil fuels. Batteries and electrochemical capacitors have been key areas of research in the past two decades. The following sections will focus on introducing key components, characterizations and performance metrics of electrochemical energy storage devices. More specifically, we will introduce considerations for designing miniature batteries, *i.e.* 3D microbatteries, which is the primary targeted application in this Thesis.

1.2.1 Basics of Batteries and Supercapacitors

All batteries contain two electrodes connected by an ionically conductive media called an electrolyte. Due to the chemical potential difference between the two electrodes, once connected to an external circuit, electrons flow from the relatively negative potential

electrode (anode) to the more positive potential electrode (cathode) while ions are transported in the electrolyte to maintain the charge balance. This process is defined as discharging. If the battery can return to its initial state by applying a voltage of the opposite direction, the battery is a rechargeable, or secondary battery. Two key factors are of particular interest when comparing battery performances. Energy density is denoted as the electrical energy that the material can deliver per mass or per volume. This is in large part determined by the chemistry of the electrochemical couple. For device comparison however, materials loading and packing density are also critical to achieve a high volumetric and areal energy density. Another factor is the power density, which indicates how fast the device can charge and discharge. Similar to energy density, power density depends on both the intrinsic properties of materials and the device architecture engineering because ionic transport length and electrode porosity affects the diffusion process.[57] Besides, Coulombic efficiency, referring to the ratio of discharge to charge capacity, targets ideally at 100%. Deviation from unity indicates the presence of side reactions, *e.g.* solid electrolyte interphase (SEI) formation.[58]

The complexity (choice of materials plus managing interfaces) leads to much slower development of battery technologies relative to technology innovation in other fields, *e.g.* microchip manufacturing, although demands for energy storage and data storage are equally urgent. D. Rolison mentioned an interesting theory to explain why battery development lags far behind microchip manufacturing.[59] If yearly performance improvement follows $1/2^n$, where n is the number of transport functions. For microchips, the performance is determined by the transport of electronic charge carrier (electron and hole), which can be improved by shortening the charge carrier traveling distance thus n

9

equals to 1. In other words, performance can be doubled in every two years (Moore's Law). In a battery however, three transport behaviors are involved: electronic transport in solid state, ionic transport in solid or liquid state, and mass transport (n=3), resulting in a 12.5% improvement per year- roughly matches the 10% improvement rate (for energy density) from the industrial statistics.

Over the years, hundreds of battery chemistries are developed in order to improve the performance metrics.[60] Some of the representatives are shown in Figure 1.4. Among them, lithium-ion batteries (LIBs) received tremendous attention due to its unparallel combination of gravimetric energy and power densities.[61-64] First commercialized by Sony in 1991, LIB owns its names to the exchange of Li^+ between graphite anode and the layered oxide cathode ($Li_{1-x}T^MO_2$) during the charge-discharge operation, where T^M is a transition metal. Polymers play important roles in LIB researches, especially in studies on binders and electrolytes.[65-69] Highly elastic, and even self-healing polymers have been used as binding materials to accommodate the large volumetric expansion of high capacity anode materials during operation.[67, 70] On the other hand, polymer electrolytes based on polyethers, *e.g.* poly(ethylene oxide) (PEO), have been studied extensively.[71] Dependence of ionic conductivity on PEO molecular weight, choice of doping salts, functional fillers and plasticizers are well summarized in separate review papers.[65, 72-74]
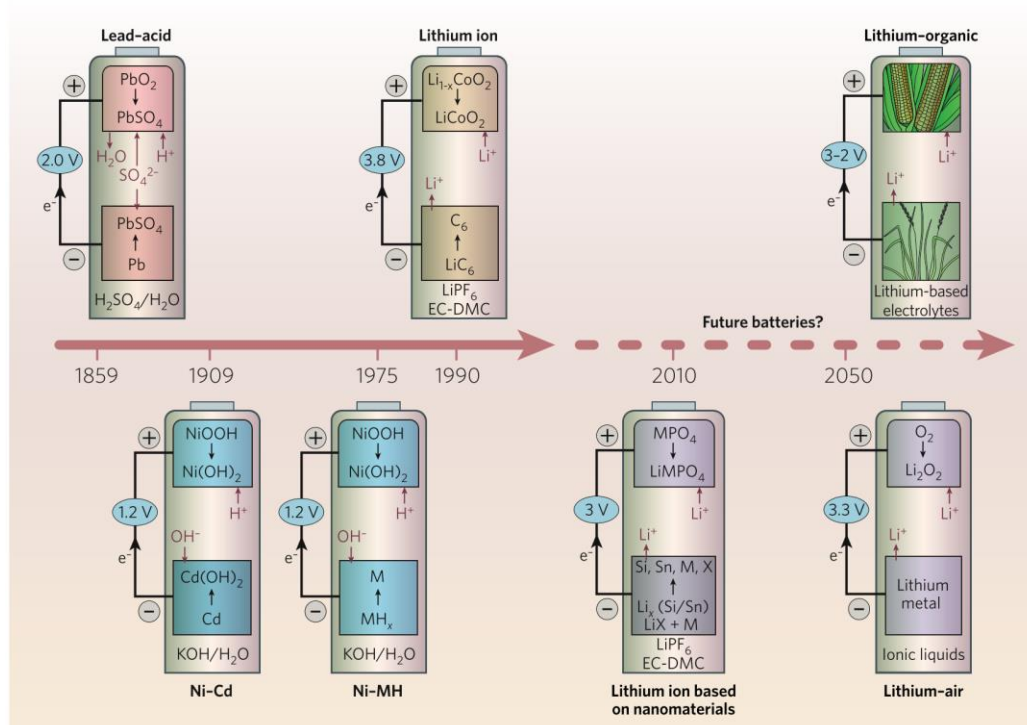
Figure 1.4 Representative secondary battery chemistries and the developing years. Reproduced from reference [60].

Supercapacitor is another important form of electrochemical energy storage. Many considerations are shared for a supercapacitor and for a battery, like the pursuit of high energy and power densities. As the major charge storage mechanism is electrostatic double layer capacitance (EDLC), instead of the diffusion-controlled chemical reactions as in a battery, supercapacitor is prone to have a higher power density but a lower energy density relative to a battery. This makes supercapacitors particularly attractive in applications where pulse power is demanded. Recently, pseudocapacitance, resulted from the rapid reactions at the electrode surface, emerges as a promising research field to combine a battery's energy and a supercapacitor's power.[75-76]
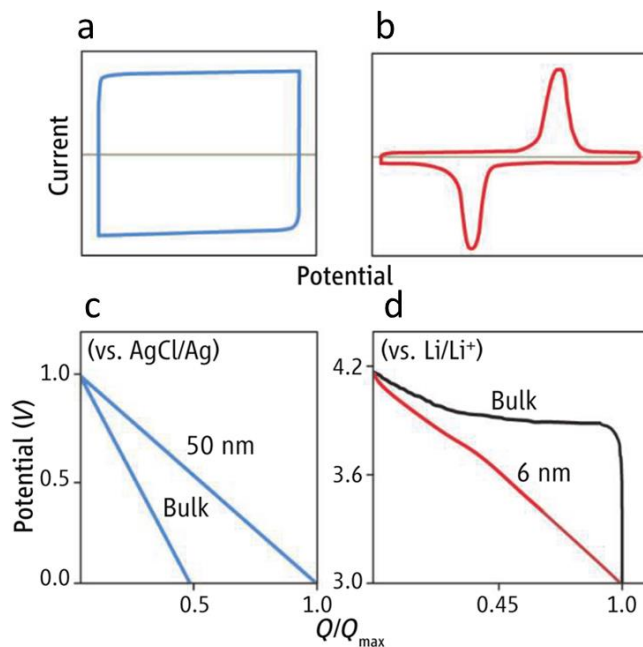
Figure 1.5 Cyclic voltammograms of typical (a) supercapacitors and (b) batteries. Galvanostatic discharging profiles of (c) supercapacitors and (d) batteries; the difference in discharging profiles of bulk and nanoscale materials are also highlighted. Reproduced from reference [77].

Three major techniques are applied to characterize the electrochemical systems: cyclic voltammetry (CV) for the investigation of electrode redox and any side reactions, galvanostatic charge-discharge (GCD) for measuring specific capacities and Coulombic efficiency, and the electrochemical impedance spectroscopy (EIS) to probe charge transfer resistance and diffusion behaviors. Typical CV and GCD profiles of batteries and supercapacitors are shown in Figure 1.5a to 1.5d. It should be noted that nanosizing of active materials generates higher surface area, lower tortuosity, which results in interesting phenomenon, as shown in Figure 1.5c and 1.5d. For surface-controlled systems like supercapacitors, nanostructured electrodes typically lead to higher charge storage capacity. For batteries, GCD profile sees a transition from plateau to linear response and in general, an improvement in rate capability although Coulombic efficiency may decrease due to more side reactions at the electrode surface.

1.2.2 Three-Dimensional Microbatteries

The primary motivation of making batteries of small form factors is to drive the development of self-powered microelectromechanical systems (MEMS), and to obtain the all-on-one-chip type of device. The absence of wiring between components on-chip and external power supplies avoids signal noises associated with interconnection and greatly improves portability. Conventionally, microbatteries refer to electrochemical cells with laminated structure comprising thin layers of cathode, anode and separator. This 2D architecture meets challenge when footprint area is highly limited on a chip. The bitter balance between energy and power densities in 2D microbatteries calls for more efficient use of the third dimension.
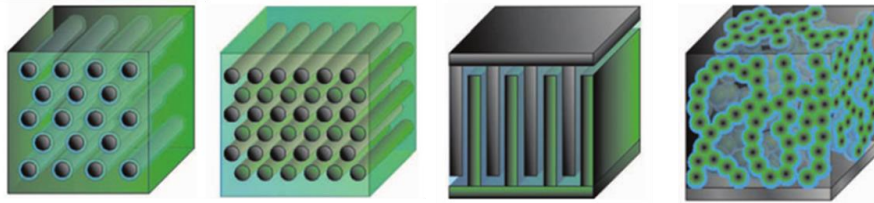
Figure 1.6 Schematic illustration of four prospective3D architectures for microscale rechargeable batteries. From left to right: interdigitated cylindrical electrode array; rod array of anode with cathode backfilled the remaining free volume; interdigitated plate array; aperiodic "sponge" architecture. Reproduced from reference [78].

The key concept of 3D microbatteries, which was summarized by D. Rolison, B. Dunn, J. Long and H. White,[5, 78] is to design electrodes with nonplanar, complex geometries to maximize energy density, and to reconfigure cell architectures enabling transport between electrodes to be one-dimensional at the microscopic level (ideally nanoscale); this is crucial to increase power density. Figure 1.6 demonstrates some of the prospective 3D architectures for microbatteries. Different from 2D configurations, two major concerns are unique: 1) nonuniform current density distribution and 2) nanoscale separation of cathode and anode. Nonuniform current distribution is undesirable as it may

13

cause varied degree of reaction at electrode surfaces, resulting in premature finishing of a charge or discharge process.[79] The distribution highly depends on electrode form factors and battery cell architecture. A dimensionless number U is proposed to indicate the current distribution uniformity in 3D microbattery cells with micropillar electrodes in Equation (1.3), where r, L refer to the micropillar diameter and length; w, h refer to the plate's width and height. And μ, σ, and C correspond to Li^+ mobility, electrode's electronic conductivity and volumetric capacity.

$$U = \left(\frac{r^2}{L^2}\right)\left(\frac{\mu}{\sigma}\right)\left(\frac{1}{C}\right) \qquad (1.3)$$

Equation (1.3) indicates that high aspect ratio (L/2r) features provide more uniform current distribution in a microbattery cell.

Nanoscale separation is desirable in that it decreases the ion transport distance in a charge-discharge cycle. However, the lower limit of separator thickness should be determined by the electron tunneling effect, electrical field strength at cathode and anode, and conductivity (both electronic and ionic) of the separator/electrolyte. It is believed that above 10 nm, electron tunneling between electrode surfaces is negligible, while below 1 nm, electrodes tend to simultaneously discharge via tunneling.[78] In real practice however, separation length may need to well exceed 10 nm. This is because on one hand, electronic conductivity of a 10 nm separating material must be at least 10^{-15} S cm^{-1} to limit a leaking current within 0.02 μA cm^{-2}, predicted by Sun *et al*;[80] very few dielectrics meet this requirement. On the other hand, dielectric breakdown, which is rarely discussed in macroscopic electrochemical cells, should be considered with care for nanoscale separators. The electrical field strength over a 10 nm film in a 3V-operating Li-ion cell is as high as

14

3×10^5 V m^{-1}! This is about one order of magnitude higher than the breakdown strength of poly(ethylene). Moreover, the number of solvated ions in nanoscale separator could be small, resulting in a capacitor-like device with nonionic dielectric in between.[78, 81] The coupling of materials choice and deposition strategy on nonplanar surfaces makes nanoscale electrolyte a challenging yet fascinating research field.

CHAPTER 2

DIRECT IMPRINTING OF WOODPILE-LIKE 3D ELECTRODES FOR

LITHIUM-ION MICROBATTERIES

2.1 Introduction

The advent of small devices, from microelectromechanical systems (MEMSs),[1] to more recently, nanoelectromechanical systems (NEMSs), [2]requires power sources with commensurate dimensions. The use of on-chip batteries, e.g. micro- and even nanobatteries, effectively avoids interconnection problems and unnecessary signal noise encountered by devices that are externally powered.[78] The downscaling of battery size will significantly enhance the overall portability and drive MEMS/NEMS toward fully autonomous devices.

A primary challenge for constructing small batteries is to fine-tune the electrode 3D architectures in order to enable both high capacity and high power using a limited footprint area.[82] To date, several techniques have been applied to create such electrodes including colloidal templating,[83-85] vapor deposition on 3D substrates,[81, 86-88] and direct ink writing.[89-90] Though these methods result in delicate electrode fabrication, some key issues remain to be solved. First, the dimensions of most of the reported electrodes are on the order of tens of microns. Further downscaling to sub-micrometer scale will enhance the reaction-diffusion kinetics however, the cost of fabrication using traditional subtractive clean room processing techniques soars as dimensions are driven to the smaller dimensions. Moreover, from a commercial point of view, any chosen fabrication technique needs to be facile, scalable and cost-effective. Current methods either require multi-step processing, extensive post-treatments or are restricted to relatively low throughput manufacturing as limited by the deposition chamber size or the writing speed.

Nanoimprint lithography (NIL) is widely considered to be a relatively low-cost, high-resolution and high-throughput surface patterning technique.[8, 91-92] Materials that can be patterned range from self-assembled monolayers (SAMs),[93] polymers and colloidal materials,[94-95] to inorganic sol-gel materials.[96] More recently, a number of reports have explored NIL to directly pattern inorganic nanoparticles/tubes into various architectures.[11, 13, 97] For example, well dispersed gold and indium tin oxide (ITO) nanoparticles can be directly molded into designed patterns via solvent-assisted NIL.[98-99] Nevertheless, due to the low modulus of elastomeric stamps,[100] insufficient mass transfer,[14] and the shrinkage upon solvent drying, the aspect ratio of the imprinted structures are generally small especially for non-polymer imprinting.[16, 101] This makes NIL more of a 2D patterning technique and limits its use in 3D electrode fabrication. Recently our group has designed a general imprinting approach to 3D metal oxide nanostructures, including the woodpile structure.[102] We utilized inks comprised predominantly of crystalline nanoparticles and sequential imprint-planarization cycles, followed by removal of sacrificial planarization layers through heating. This "stack-up" protocol enables the attainment of 3D architectures with high, and importantly, user-defined aspect ratios.

Here, we presented a rapid and scalable approach for the fabrication of high-performance TiO_2 woodpile nanoelectrodes for lithium-ion battery (LIB) using solvent-assisted NIL. The electrodes demonstrate superior rate capability and exhibited a specific capacity of 250.9 mAhg^{-1}, which is among the highest reported. As the number of stacked layers increases, the electrode's areal capacity exhibits a proportional enhancement, demonstrating great potential as an on-chip power source. To the best of our knowledge, this is the first report on 3D battery electrode fabricated by direct NIL of electroactive

nanoparticles. The compatibility of NIL with the current micro/nanofabrication process make it potentially a platform technology toward scaled production and integration of nanobatteries into MEMS/NEMS.

2.2 Experimental Section

2.2.1 Fabrication of PDMS Mold

Patterned PDMS stamps were fabricated by casting the prepolymer mixture against silicon master molds with a line grating pattern (linewidth ~ 425 nm; pitch~ 950 nm; height~ 480 nm). The prepolymer mixture (10:1 weight ratio of Sylgard 184 silicone elastomer base and curing agent) was mixed and degassed in vacuum oven for 20 min at room temperature. Then the mixture was poured onto the master mold and placed at 70 ℃ for 5 h in an oven. After curing, PDMS stamps were obtained via peeling off from master mold.

2.2.2 Preparation of TiO$_2$ Nanoparticle Ink

To obtain TiO$_2$ nanoparticle ink, a commercial titanium oxide (anatase, 20 wt%) nanoparticle dispersion in 1, 2 propanediol (US Research Nanomaterials, Inc.) was mixed with 1, 2 propanediol and methanol in 1:1:5 weight ratio. This mixture dispersion was further vortex-mixed and sonicated for a few minutes to obtain a stable, well-dispersed ink. Particle size and distribution were checked by TEM (JEOL 2000FX) and Malvern Nano Zetasizer.

2.2.3 Fabrication of Woodpile Structure and the Planar Control Samples

Silicon dioxide wafer substrates were sonicated in ethanol and acetone for 5 min. Then, these substrates were washed with deionized water, and dried under nitrogen gas. A Ti/Au (5 nm/50 nm) bilayer was deposited on the silicon dioxide wafer with a designed

pattern, controlled by a customized shadow mask. The TiO_2 nanoparticle ink was spin-coated onto the silicon dioxide substrate (3000 rpm, 90 s) in a glove box with a 5 % relative humidity environment. Then, PDMS stamp was placed on the ink and dried on the hot plate at 55 °C for 5 min. After drying, PDMS stamp was peeled off and the patterned film was obtained. A UV-crosslinkable thiol-ene acrylate prepolymer (NOA60, Norland Products Inc.) was used for planarization. After imprinting the first layer, the patterned structure was first pretreated with UV-ozone for 15 min. Then two layers of NOA60 (10 wt% in propylene glycol monomethyl ether acetate) were deposited by consecutively spin coating at 1000 rpm for 1 min and curing. The imprinting-planarization process was simply repeated for the desired number of layers. Finally, TiO_2 with designed layers was calcined at 750 °C for 5 min. Structure dimensions were checked under SEM (Magellan 400). All control samples were fabricated by multi-time spin coating and thermal annealing. The film was thermally annealed at lower temperature (400 ℃) for 5 min after each spin coating except for the last time that the sample was calcined at 750 ℃ for 5 min like the woodpiles. Film thickness and porosity were checked by ellipsometry.

2.2.4 Electrochemical Tests

All electrochemical measurements were conducted in the half-cell configuration, assembled in an argon glove box. $LiClO_4$ (1M, in EC/DMC=1/1v) was used as the liquid electrolyte. A piece of lithium foil served as both the counter and reference electrode. Charge and discharge profiles of the electrodes were measured by galvanostatic tests (Maccor 4304) under different C-rates, within a voltage window of 1.0-3.0 V. Extended cycling tests were performed with voltage window of 0.4-3.0 V. Control samples of un-

patterned TiO$_2$ films with varied thickness were tested under same conditions and used for comparison.

2.3 Results and Discussion

The TiO$_2$ ink used in this study was first engineered to provide imprintability. Nanoparticle size, dispersity, solid concentration, and ink viscosity are among the key factors. Here, the imprint ink was made from a 20 wt% commercial TiO$_2$ dispersion in 1, 2-propanediol. Transmission electron microscopy (TEM) shows that the particle size is below 10 nm (Figure 2.1a). This is comparable with the dynamic light scattering (DLS) measurement where the number- and volume-averaged particle sizes are 13.6 and 15.7 nm (Figure 2.1b). The slight difference results mainly from the inclusion of solvation effect and ligands in DLS. The ink was then diluted in a 1,2-propanediol/methanol mixture solvent to have a 3 wt% solid concentration. The incorporation of methanol is critical in three ways: 1). Methanol lowers the ink viscosity and improves wettability to facilitate film formation; 2). The low boiling-point nature (b.p. 64.7℃) leads to fast evaporation during spin coating and quickly concentrates the ink while the high boiling-point 1,2-propanadiol (b.p. 188.2℃) provides reasonable fluidity for molding; 3). The evaporation induced composition change of ink does not lead to severe particle aggregation as a result of good miscibility. As shown in Figure 2.1c, the ink exhibits very low viscosity of 1.8 mPa·s which is close to the viscosity of the mixture solvent (1.37 mPa·s at 25 ℃). This relatively low concentration and viscosity is critical to mold filling and residual layer-free imprinting. The ink was stable with negligible precipitation observed over several months (zeta potential measured to be +13.4 mV). In fact, with 5-min sonication, ink stored for extended periods of time can be used as successfully as fresh ink in the imprinting process.

The electron diffraction (ED) pattern of the TiO₂ nanoparticles (Figure 2.1d) demonstrates a series of distinct diffraction rings, indicative of the polycrystalline feature and is indexed to anatase phase. The calculated d-spacing of the (101) planes is 0.36 nm as confirmed by high resolution TEM imaging (Figure 2.1e).
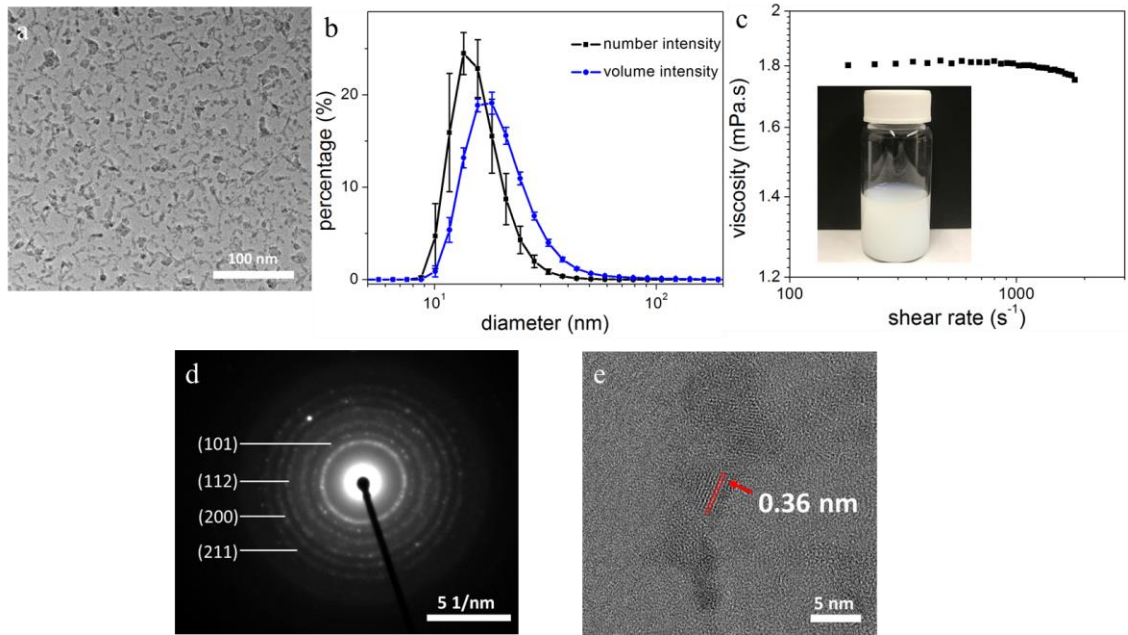
Figure 2.1 (a) TEM image of TiO₂ nanoparticles showing particle size below 10 nm. (b) DLS measurement of nanoparticle size in 1,2-propanediol/methanol mixture solvent at room temperature. (c) Shear viscosity of the TiO₂ ink measured at room temperature under shear rate between 100-1000 s⁻¹. (inset: optical image of the well-dispersed TiO₂ ink). (d) Electron diffraction pattern of TiO₂ nanoparticles. (e). High resolution TEM image showing TiO₂ crystal lattice.

The fabrication process of the multilayered TiO₂ electrode is depicted in Figure 2.2. The effective footprint area was defined to be 1.5×1.5 cm². To do this, a bilayer of Ti/Au (5 nm/50 nm) current collector was e-beam evaporated onto the silicon dioxide wafer through a shadow mask (Figure 2.3). The current collector is connected to the contact pad by a thin trace of gold, the dimensions of which are negligible relative to the current collection area. The imprinting followed a typical spin coating-molding-demolding process. The patterned TiO₂ structure solidifies as excessive solvent permeates through poly

21

(dimethyl siloxane) (PDMS) stamp upon heating. The structure is robust even before calcination due to the strong cohesive forces between TiO_2 particles. This allowed quick demolding in less than 5 min. In order to make multilayered structures, we introduced the planarization step. A commercial thiol-ene based acrylate photoresist (NOA60, Norland, Inc) is selected as the planarization material. During spin coating, it fills the trenches between TiO_2 line patterns, forming a solid, planar surface upon UV exposure, which then acts as the new substrate. By repeating steps of imprinting and planarization, additional layers can be readily stacked onto previous ones in an orthogonal orientation. Conceivably, as the structure volume increases with the number of stacked layers, a nearly constant surface-to-volume ratio is maintained. The woodpile architecture was obtained after a short time calcination in air at 750 ℃ for 5 min, during which the organic planarization layer was completely removed. The neck formation and ripening of particles enhance the mechanical strength of the architecture and create nanoscale voids within TiO_2 lines, which favors ion transfer.[103] The porosity is estimated to be 31.3% based on the difference of refractive index from bulk TiO_2 (decreased from 2.49 to 1.82).
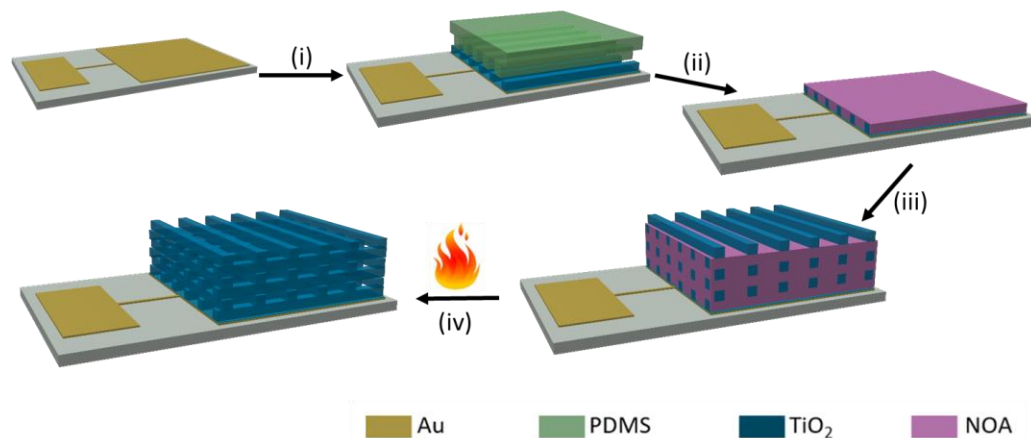
Figure 2.2 Schematic illustration of the TiO₂ woodpile fabrication process. (i) Single layer imprinting. TiO₂ ink spin coated on gold charge collector followed by PDMS stamp molding-drying-demolding process. (ii) Planarization with cross-linkable thiol-ene based acrylate resin. (iii) Multilayer structure fabrication by repeating (i) and (ii). (iv) Woodpile electrode obtained after calcination.
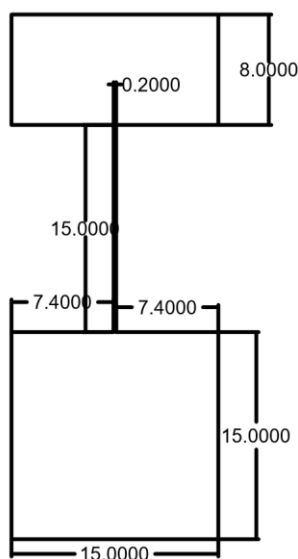
Figure 2.3 Shadow mask design for depositing current collector (unit: mm).

Scanning electron microscopy (SEM) and atomic force microscopy (AFM) of the attained single layer imprint show that well-defined line pattern of approximately 200 nm in width and height (Figure 2.4a, 2.4b) is obtained, generating an aspect ratio of 1. Barely any residual layer was observed. The deviation from stamp dimension results from the shrinkage caused by solvent evaporation and calcination. The dimensions remained

consistent in the multilayered woodpile structure (Figure 2.4c to 2.4g). Consequently, stacking up to 2, 3, 4 and 6 layers resulted in effective aspect ratios of 2, 3, 4 and 6 respectively. Notably, the line shapes were well maintained even though they spanned wide gaps over the underlying layers. X-ray diffraction (XRD) indicates that after calcination, the sub-10 nm TiO_2 particles merged into bigger crystallites confirmed by the sharper (101) peak (Figure 2.4h). The crystallite size is calculated to increase from 3.8 nm to 23.6 nm. In addition, we noticed that small amount of TiO_2 converted from anatase to rutile phase. Note that both phases are electroactive and possess similar theoretical specific capacities (~335 $mAhg^{-1}$) when nanoscale materials are used,[104-105] no extra effort on crystal phase refinement was offered.

To demonstrate the readiness of scaled fabrication, an inch-scale imprint was made (Figure 2.4i). The optical color results from the light interaction with the periodic patterns on the substrate. To evaluate the electrochemical performance of the imprinted electrodes, a Li-TiO_2 half-cell was assembled by immersing the TiO_2 woodpile into liquid electrolyte and using lithium foil as counter electrode (Figure 2.5a). Figure 2.5b shows the cyclic voltammogram (CV) of a 6-layer TiO_2 woodpile electrode at different scan rates. At 0.1 mVs^{-1}, characteristic cathodic peak at 1.74V and anodic peak at 2.04V were observed, corresponding to Li^+ insertion and extraction ($xLi^+ + TiO_2 \leftrightarrow Li_xTiO_2$). By correlating peak current (i) to scan rates (v) (Figure 2.5c), we find that $i \propto v^{0.5}$, indicating diffusion controlled kinetics.[106] As scan rate increased to 10 mVs^{-1}, cathodic and anodic peak shifted slightly to1.65 V and 2.1 V. This scan rate-dependence is indicative of the deviation from Nernstian system in the fast scan region. Note that the woodpile architecture provides sufficient pathways for ion transport. We believe the kinetic limitation arises from either

24

electron transport across electrode or from the relatively slow ion diffusion within TiO_2 particles.
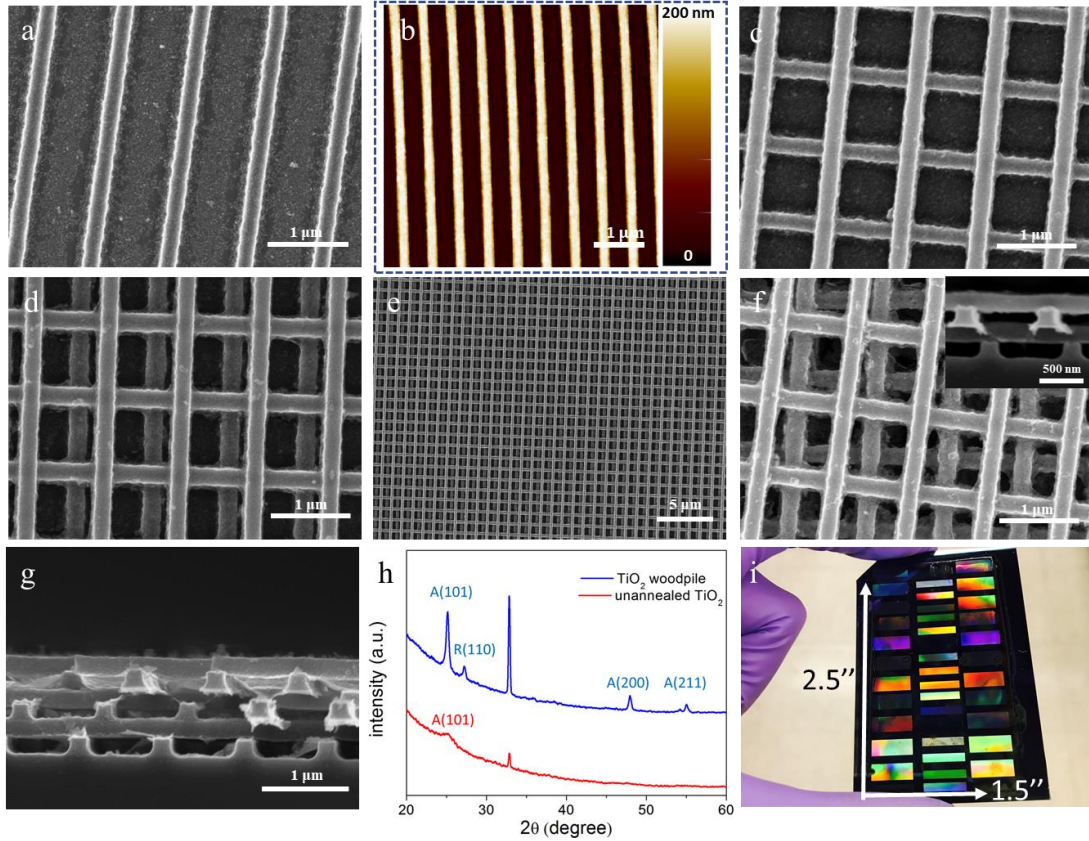
Figure 2.4 Characterizations of the calcined imprinted structures. (a, b) SEM top view and AFM height profile of the single layer imprint. (c, d) SEM top views of 2-layer and 3-layer woodpile structure. (e) Zoom-out view of the 3-layer woodpile structure. (f) SEM top view of 4-layer woodpile structure (inset: cross sectional view). (g) SEM cross section of the 6-layer woodpile structure. (h) XRD measurement of TiO_2 before and after calcination. (i) Photograph of a larger area, 1.5''× 2.5'' imprint.

To demonstrate sequential imprinting as an efficient way to enhance areal capacity, a series of un-patterned TiO_2 film electrodes with comparable loading and porosity were fabricated as control samples. For example, a TiO_2 film made by 6 spin coating-calcination cycles is used to compare with the 6-layer woodpile. As shown in Figure 2.5d, areal capacity of woodpile electrodes increases linearly with the stacking of layers. The imprinted electrodes exhibit areal capacities of 3.6, 7.1, 11.4, 15.5 and 21.3 $\mu Ahcm^{-2}$ for

1-, 2-, 3-, 4- and 6-layer electrode respectively under discharge current density of 500 mAg$^-$^{1}. This confirms that the woodpile stacking is effective towards multiplied capacity. Conceivably, when normalized to the mass loading of TiO$_2$, woodpile electrodes with one to six layers possess identical specific capacity of approximately 250.9 mAhg^{-1}, corresponding to 0.74 Li uptake per formula unit. This value is larger than the bulk anatase TiO$_2$ lattice, which at most accommodates 0.5 Li per formula unit, but it is not unexpected. Prior literature has revealed that decreasing particle size to the nanoscale induces size-dependent expansion Li uptake capacity and that the maximum Li uptake was reported to approach 1.0 per formula unit for particle sizes approaching 11 nm.[104] Differential capacity curves of charge and discharge (Figure 2.5e) of woodpile electrode shows sharp and single peaks at 1.74 V and 2.10 V. This corresponds well with the CV measurement, indicating the redox reaction occurs predominantly at these two potentials. In contrast, for planar TiO$_2$ electrodes, increasing film thickness failed to achieve proportional enhancement of areal capacity (Figure 2.5f). A 6-layer film generates less than quadruple amount of capacity of a single layer. This indicates a significant waste of TiO$_2$ due to inefficient material packing. The difference can be explained in terms of the reaction-diffusion kinetics,[107] the impact of which may not be evident when structure dimensions are small, as shown by the overlap of discharging profiles of patterned and un-patterned single layers. Nevertheless, when thickness increases, the slow diffusion rate of Li-ion across the electrode becomes significant. As a result, ion insertion into the inner regions of the TiO$_2$ film is impeded and only the top layer is effective. On the contrary, woodpile architecture circumvents this limitation by maintaining a constant surface-to-volume ratio

and providing an infiltrated ionic pathway into the structure. This finding demonstrates the potential of using TiO_2 woodpile as a high-performance on-chip nanoelectrode.
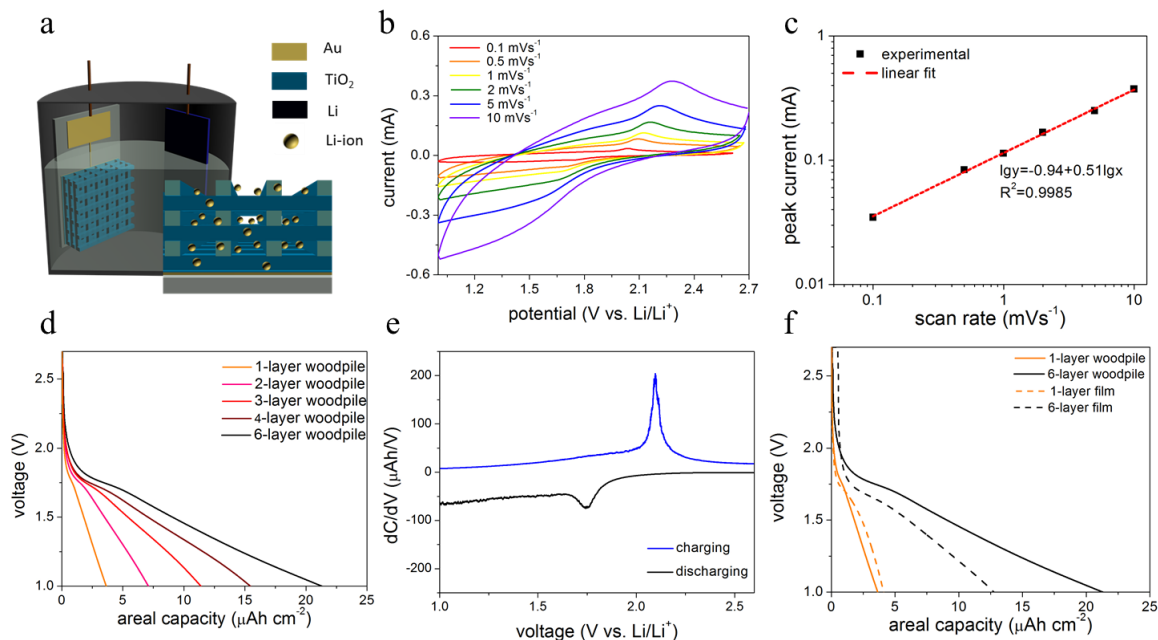
Figure 2.5 Electrochemical performance of TiO_2 woodpiles and control samples. (a) Electrochemical test set-up and illustrative view of electrolyte permeation into woodpile structure. (b) CVs of a 6-layer TiO_2 woodpile electrode under scan rates of 0.1, 0.5, 1.0, 2.0, 5.0 and 10 mVs^{-1}. (c) Plot of scan rate dependence of anodic peak current. (d) Galvanostatic discharge profiles of imprinted architectures with 1, 2, 3, 4 and 6 layers under current density 500 mA g^{-1}. (e) Differential charge/discharge capacity curves of TiO_2 woodpile electrode. (f) Comparison of capacity enhancement in TiO_2 woodpiles and in planar films.

The imprinted woodpile architecture becomes even more advantageous when performance under higher discharge rates is investigated. We define discharge current density of 1 C as 335 mA g^{-1}. As shown in Figure 2.6a, at 3 C (~ 1000 mA g^{-1}), the planar TiO_2 electrode lost half of its capacity while the woodpile electrode demonstrated a capacity retention of 75%. From 1000 mAg^{-1} to higher discharge rates, the woodpile electrode consistently exhibited doubled to tripled capacity retention relative to the planar electrode. Even at rate as high as 15 C (5000 mA g^{-1}), the woodpile electrode is able to deliver 25% of its initial capacity whereas the flat sample suffers almost complete capacity

degradation. Notice that the absolute values of their initial capacities at 500 mAg^{-1} are offset by a factor of 1.7 (Figure 2.5f), the woodpile exhibits 3-5 folds improvement of the actual areal capacity. Figure 2.6b compares the specific capacity and the discharge current density with TiO$_2$ electrodes reported from recent literature.[104-105, 108-115] The selected works mainly focus on nanostructured TiO$_2$ (e.g. nanotube, nanocage, hollow shell, etc) or composites of TiO$_2$ and conductive additives including carbon nanotubes (CNTs) and graphene. It is worth noting that although we used commercially available particles and added no carbonaceous additives, these relatively simple and scalable woodpile structures achieved comparable-to-better electrochemical performance relative to the best-in-class reports. This comparison highlights the impact of nanoscale patterning on electrode's performance.
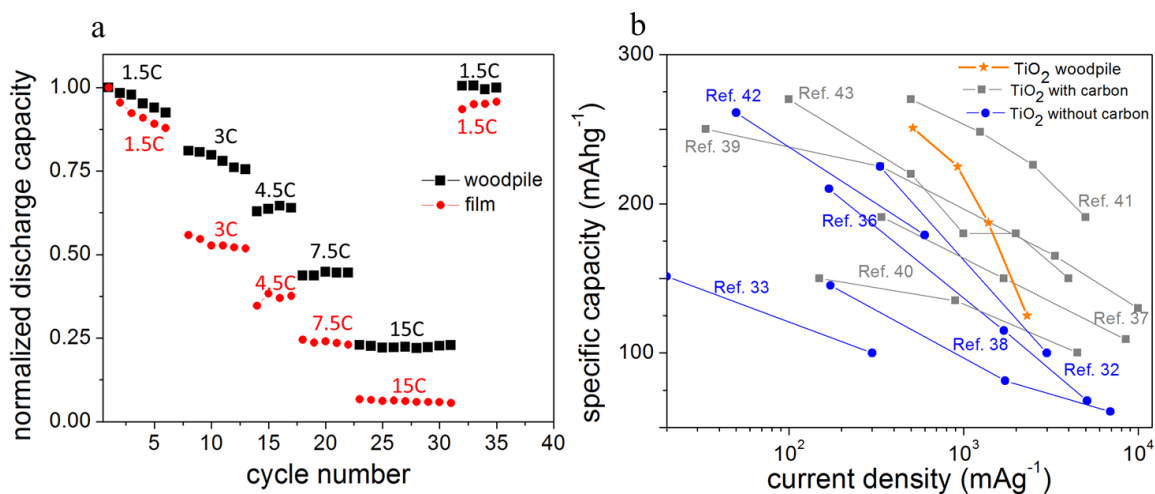
Figure 2.6 Rate capability and electrochemical performance comparison. (a) Capacity retention of 6-layer woodpile electrode and control film sample under discharge rates from 1.5 C (500 mAg^{-1}) to 15 C (5000 mAg^{-1}). (b) Comparison of specific capacity and cycling current density of the 6-layer woodpile electrode with recently reported TiO$_2$ electrodes. Voltage windows of all tests are between 1.0-3.0 V versus Li$^+$/Li.

Remarkably, the woodpile electrode demonstrated stable performance even during harsh testing conditions, such as the 15 C discharging. To further investigate the stability of the

imprinted electrode, we extended the lower cut-off voltage to 0.4 V. As shown in Figure 2.7a, the woodpile electrodes still followed linear relationship as stacking of layers increased and demonstrated expanded capacity values. Areal capacity of 6-layer electrode increased from 21.3 $\mu Ahcm^{-2}$ to 35.1 $\mu Ahcm^{-2}$, resulting in specific capacity as high as 413.4 $mAhg^{-1}$, which is even larger than the theoretical value of 335 $mAhg^{-1}$. The exact reason is not conclusive yet, but we propose that surface charge storage mechanisms may be involved. The randomly oriented small TiO_2 crystallites provide nanovoids to adsorb additional Li^+, which is similar to the "house of cards" model used to explain larger Li^+ storage capacity in amorphous carbon (relative to graphite).[58, 116-117] In fact, Ferris *et al* recently reported that an anomalous extension of voltage window was also observed in nanosupercapacitors.[118] The atypical electrochemical properties in nanodevices need more fundamental investigation. In this extended voltage window, TiO_2 is likely to suffer over-discharge and may go through irreversible structural changes. Surprisingly, the imprinted TiO_2 woodpile electrode could be stably cycled under current densities from 500-5000 mAg^{-1} (Figure 2.7b). This may be attributed to the thermal treatment and the nanoscale line pattern for facile strain release.
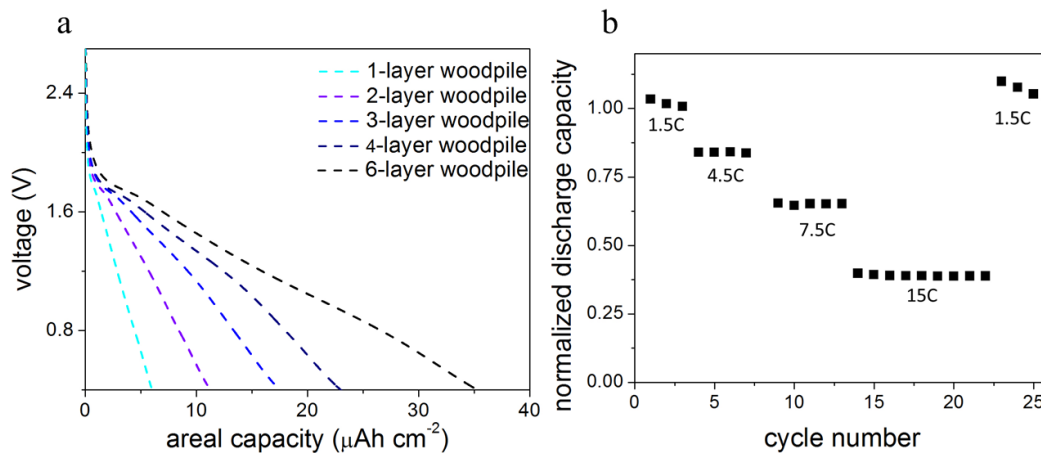
Figure 2.7 Electrochemical tests of woodpile electrodes in extended voltage window from 0.4 V-3.0 V versus Li$^+$/Li. (a) Expanded areal capacities of 1-layer to 6-layer structures. (b) Capacity retention of 6-layer woodpile electrode under discharge rates from 500-5000 mAg^{-1} in the extended voltage window.

It can be clearly seen in Figure 2.8a that the woodpile remained intact after the test without evident cracks or delamination. It is noted however, that compared to the untested woodpiles, the surface structure of the tested samples became coarser and line width changed from 200 nm to 380 nm (Figure 2.8b). This results from the volume change of TiO$_2$ and forming of the solid electrolyte interphase (SEI). It has been reported that SEI tends to form on TiO$_2$ surface at lower potential.[119] To determine the surface elemental composition, electrodes after testing were rinsed in propylene carbonate (PC) to clean the residual liquid electrolyte and dried in an oven. Energy-dispersive X-ray spectroscopy (EDX) shows that besides Ti and O, Cl and C also existed (Figure 2.8c). A more detailed X-ray photoelectron spectroscopy (XPS) elemental scan reveals that the atomic ratio of O: Li: Cl: C is 52.4%: 27.3%:17.0%: 3.1% (Figure 2.8d to 2.8g). As the penetration depth (less than 20 nm) of XPS is much smaller than EDX, barely any signal from Ti was collected, which is indicative of complete coverage of TiO$_2$ under the surface SEI layer. In fact, capacity fade can result from continuous cracking and reformation of the SEI. The

stable performance of the woodpile electrodes confirms that the SEI was intact during the tests.
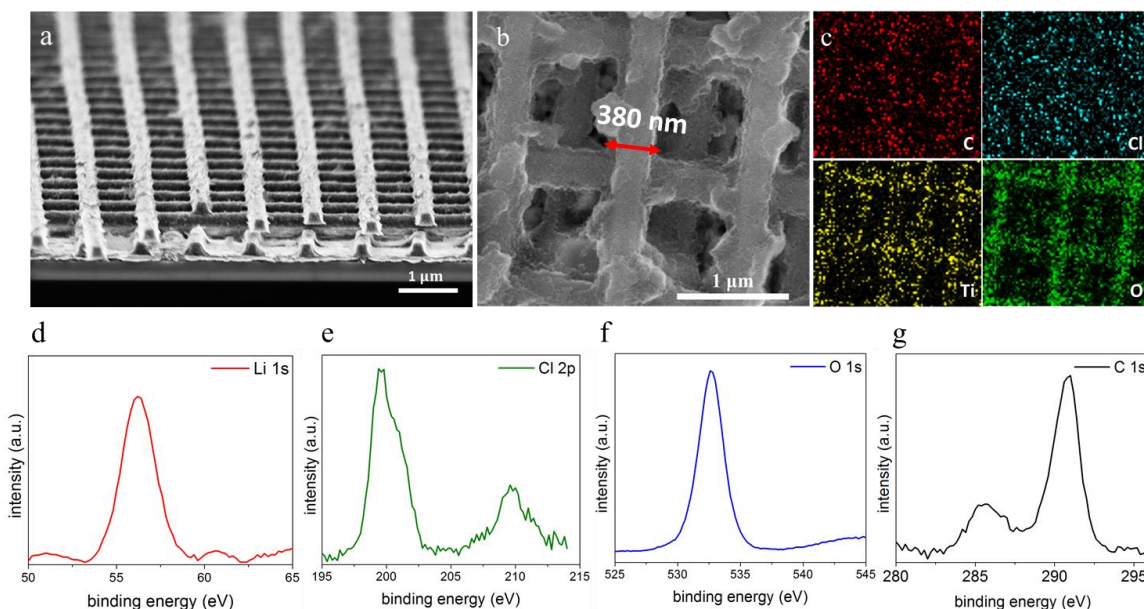
Figure 2.8 SEM imaging and elemental analysis of the woodpile electrodes after electrochemical tests. (a) Cross-sectional view of a 3-layer woodpile after cycling. (b) Zoom-in view of a 3-layer woodpile showing the structure's dimension and surface morphology changes. (c) EDX measurement of the woodpile. (d-g) XPS elemental scan of Li 1s, Cl 2p, O 1s and C 1s.

2.4 Conclusions and Future Work

In summary, we fabricated the 3D TiO_2 woodpile electrodes comprised designated numbers of stacked layers for lithium-ion nanobatteries using solvent-assisted NIL. This technique allows scalable fabrication of delicate electrode architectures with nanoscale resolution and yields specific capacities as high as 250.9 mAhg^{-1} and stable performance even over an extended voltage window. In addition, the sequential imprinting enabled the areal capacity to be readily multiplied while maintaining superior rate capability. In this work, we demonstrated up to 6 layers of stackings. Conceivably, by using the method described, even thicker electrodes can be fabricated. The upper limit is determined by the mechanical strength and conductivity of the electroactive material. As a solution-based,

31

additive manufacturing method, it is possible to avoid such limitations by formulating composite inks to improve rheological, mechanical and electrical properties. The method here is general and may inspire investigations into patterning a broad array of electroactive materials.

CHAPTER 3

FULLY INTEGRATED, HIGH-POWER 3D MICROBATTERIES FROM

IMPRINTED ELECTRODES AND COPOLYMER GEL ELECTROLYTES

3.1 Introduction

The emerging interest in "autonomous" microelectrochemical systems (MEMS) calls for miniaturized energy storage to achieve on-chip power supply. One primary requirement for such a device is to deliver high power within a confined volume (<10 mm^3).[4] While microsupercapacitors possess favorable power density, few have energy density approaching that of a microbattery, which suffers the opposite challenge.[120] Here, we report a fully integrated three-dimensional (3D) lithium-ion microbattery that provides supercapacitor-like, high-power density constructed from imprinted microelectrodes array.

To overcome the trade-off between power and energy, the 3D microbattery concept was proposed.[78] In brief, the electrochemical performance in such device is enhanced by increasing the electrode surface area and active material loading in the off-plane dimension. Until now, a number of techniques have been reported to obtain delicate microelectrode architectures. These methods include vertically-aligned nanotube/wall synthesis from gas and liquid phase,[121-122] thin film deposition on conductive 3D scaffolds,[88, 123] colloidal templating,[83] and direct ink writing.[90] Despite the progress in electrode fabrication, many of these studies stopped at half-cell demonstrations while only few reports are available on integrated 3D batteries that take full advantage of the electrodes 3D structures.[84, 89, 124-128] It is with rigorous material requirements and processing complexity to integrate elements with complicated 3D topography and feature dimensions spanning from tens of nanometers to millimeter scales. Two aspects are of key significance to construct a fully assembled,

high-performance microbattery, namely (1) a design of cell configuration that is easy to integrate and (2) the effective transfer of high-quality electroactive materials into battery cell architecture.

To date, many reported microbatteries adopt the coplanar configuration,[89, 126-128] wherein the interdigitated cathode and anode are aligned next to each other on a charge collector pre-patterned on an insulating substrate. The making of such configuration normally requires alignment/micro-positioning system which adds challenge to scaled, high-throughput fabrication. Alternatively, the stacked 3D electrochemical cell made from layer-by-layer (LBL) coating/deposition is free from any form of alignment.[107] Moreover, stacked configurations can potentially double the areal power and energy densities as footprint area is defined by single electrode. However, the electrochemical performances of previously reported stacked microbatteries leave great space for improvement.[81] Structural inhomogeneities, together with the material's low ionic and electronic conductivities compromise the merits of the 3D design and prevent the battery from achieving high power density. In this work, we managed to avoid these issues by decoupling the material synthesis and post-synthesis fabrication.

In general, active materials may be transferred into microsystems by *in situ* synthesis (e.g. CVD and electrodeposition) and particle-based patterning.[120] The latter strategy is to transfer already synthesized functional nanoparticles into miniaturized cell from well-dispersed suspension (ink). Conceivably, the decoupling of synthesis and post-synthesis processing opens a wider window for optimizing nanoparticle crystal structure and size,[129] morphology,[130] elemental composition and other properties, e.g. conductivity, by forming composites.[131] Among the various patterning techniques, imprint lithography

appears as a promising candidate that combines the merits of additive manufacturing and scaled production. It is a collection of techniques based on molding with an elastomeric stamp.[9] The versatility of patternable materials, from polymers to inorganics,[102, 132] makes it a convenient tool for scalable 2D/3D patterning and device fabrication e.g. antimicrobial surfaces,[133] wavelength-selective thermal emitter,[134] and plasmonic 3D gratings.[135] The utilization of imprint lithography in microbattery fabrication is highly beneficial yet surprisingly rare. It becomes especially advantageous when the critical dimension of targeted electrode structure is sub-micron as this resolution starts to challenge techniques like inkjet printing and 3D printing.[136] Recently, we demonstrated a series of woodpile-like 3D microelectrodes directly imprinted from TiO_2 nanoparticle dispersion which exhibited significantly improved capacity and rate capability.[137]

In this work, we synthesized sub-10 nm $LiMn_2O_4$ (LMO) and $Li_4Ti_5O_{12}$ (LTO) nanoparticles with refined crystalline structure through green, solvothermal synthesis. In addition, a non-crystalline random copolymer, poly (dopamine acrylamide)-co-poly (ethylene glycol) methyl ether methacrylate (PDMA-co-PEG$_{500}$) was developed as the separator and subsequently as a gel polymer electrolyte (GPE) after complexation with $LiClO_4$ liquid electrolyte. LMO nanoparticles were imprinted into 3D microelectrode and the stacked full cell was constructed by coating the electrode with polymer and LTO ink in a LBL manner. By carefully engineering material synthesis and processing, the microbattery in this work demonstrated robust cycling performance and a supercapacitor-like power density up to 855.5 $\mu Wcm^{-2}\mu m^{-1}$. To the best of our knowledge, this is the first report of the fabrication of fully integrated 3D microbatteries by direct imprinting using crystalline nanoparticle-based inks.

3.2 Experimental Section

3.2.1 LMO and LTO synthesis

The LMO particles were synthesized via a hydrothermal synthesis method in stainless steel autoclaves with a 190 mL teflon reaction chamber. Teflon inserts were removed from the autoclaves and placed on magnetic stirrers. A 100 mL 0.1 M LiOH solution (LiOH·H_2O (*p.a.* Bie&Berntsen A/S)) was added to the insert and 1.217 g $KMnO_4$ (*p.a.* Merck) was dissolved under mild stirring. When the $KMnO_4$ was completely dissolved, 1.2 mL of ethanol was added to the solution. The magnet was removed from the insert and the insert was sealed in the autoclave and placed in a preheated oven at 180°C for 5 hours. The autoclaves were cooled naturally overnight. The product was washed and centrifuged three times in water/ethanol mixtures and dried naturally.

The LTO particles were synthesized via a hydrothermal flow synthesis method using the same setup and method as described by Laumann *et al.*[138] In short, a 4:5 Li:Ti precursor with 5% Li excess was made by dissolving 0.745 g of Li metal in absolute ethanol and mixing it with 37 mL of titanium (IV) isopropoxide (97%, Sigma Aldrich). The mixture was then diluted with 300 mL of isopropanol, and this final mixture was used as the precursor solution. The precursor solvent was then passed through the hydrothermal flow reactor, with deionized water as preheated solvent and a reactor temperature of 425 °C. The product was collected and washed in the same way as the LMO particles.

3.2.2 Synchrotron PXRD measurements

Synchrotron PXRD data were collected on the large Debye–Scherrer image plate diffractometer at beamline BL44B2, SPring8, Japan, using $\lambda = 0.499715$ Å. The powders were filled in 0.2 mm glass capillaries. The samples were spun and cooled to 120 K during

measurements. A CeO$_2$ standard was measured to determine the instrumental broadening in order to obtain reliable crystallite sizes.

3.2.3 LMO and LTO ink preparation

LMO ink was made by first dispersing LMO and minimal 4-hydroxybenzoic acid in a mixed solvent of N-methyl-2-pyrrolidone and methanol (1/1 by weight). The mixture was then bath sonicated for half an hour followed with probe ultrasonication for 1hour, resulting in a fine, oil-like black ink. Ink concentration was further doubled (to around 10 wt%) via nitrogen flow blowing away methanol. LTO ink was made by dispersing LTO nanopowder together with mesoporous carbon (d<500 nm, Sigma-Aldrich) in solvent (DI water/ethanol/ethylene glycol 16/8/1 by volume). The mixture was then bath sonicated for 30 min. Aqueous polymer binder poly (vinylpyrrolidone) (Mw=58 kg mol^{-1}, Sigma-Aldrich) was then added into the dispersion followed with ball milling for additional 1 hour. Ink viscosity was characterized by m-VROC rheometer.

3.2.4 Cathode imprinting

Silicon master molds of pattern A, B, and C (Figure 3.1) were used to transfer pattern to PDMS stamps based on standard Sylgard 184 (Dow Corning) and crosslinker. ITO coated glass substrates were treated for 15 min under UV-ozone. LMO ink was spin coated onto the substrate at 600 rpm for 30 s, followed with PDMS stamp molding. After that, samples were soft baked at 70 ℃ followed with demolding. Finally, the samples were thermally annealed at 400 ℃ for 2 hours in nitrogen flow.
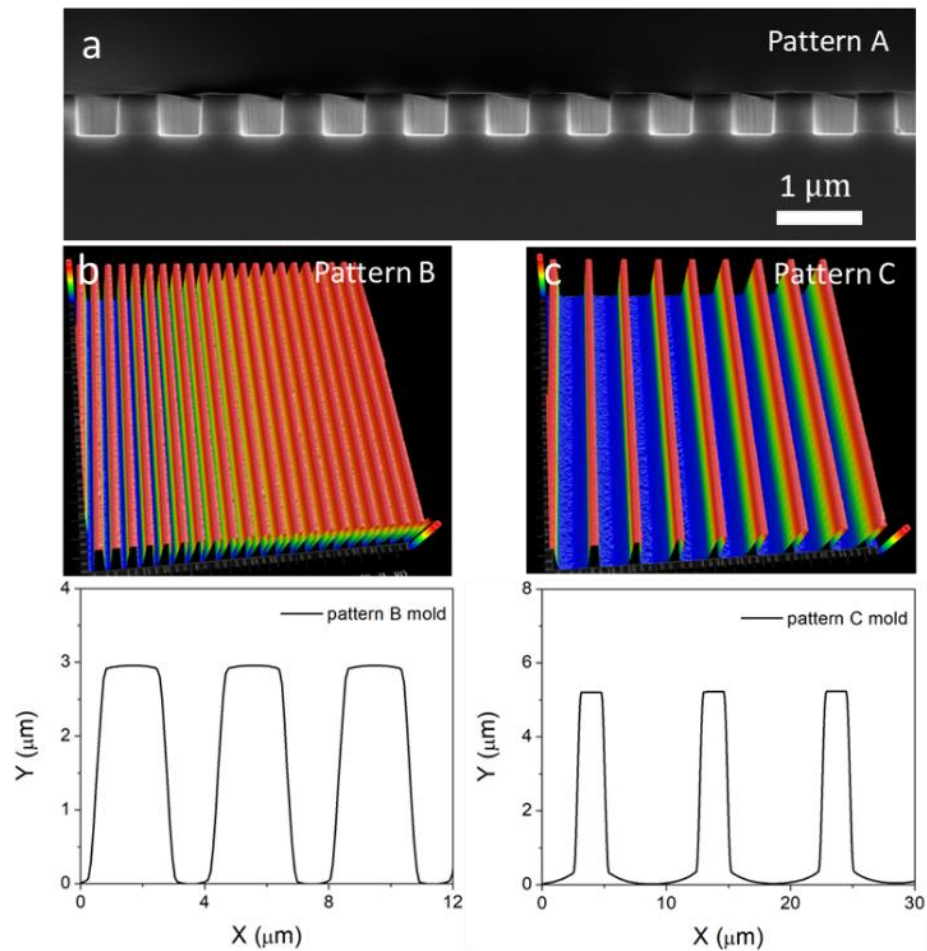
Figure 3.1 Characterization of silicon master mold dimensions. (a) cross-sectional SEM image of pattern A mold. (b) and (c) optical profilometry of pattern B and pattern C molds and the dimensional profiles.

3.2.5 PDMA-co-PEG$_{500}$ synthesis

Dopamine acrylamide (DMA) was synthesized and purified based on a reported method.[139] To synthesize PDMA-co-PEG$_{500}$, poly (ethylene glycol) methyl ether methacrylate (PEG$_{500}$, M_w=500 gmol^{-1}, Sigma-Aldrich) was passed through basic Al$_2$O$_3$ column to remove the inhibitor. DMA (1.1 g), PEG$_{500}$ (5.0 g) and azobisisobutyronitrile (AIBN, 0.11 g) were dissolved in 15 ml DMF in a 50 ml Schlenk flask. The system was degassed through three freeze-pump-thaw cycles and stirred overnight at 60 ℃. The polymer was precipitated in ethyl ether three times and was dried in oven. The molecular

weight was measured by MALS-GPC. Molar ratio of comonomers in PDMA-*co*-PEG$_{500}$ was characterized by ^{1}H-NMR. The degree of crystallization was measured by DSC between -60 ℃ and 110 ℃ with a scanning rate of 5 ℃ min^{-1}.

3.2.6 Microbattery assembly

PDMA-co-PEG$_{500}$ was dissolved in ethanol and formed 20 mg ml^{-1} solutions. Before coating, the imprinted LMO cathodes were subjected to 15 s oxygen plasma treatment. For a 1 cm^2 imprint, 25 µL of the copolymer solution was drop casted onto the imprinted cathode in a glove box with controlled humidity (< 3%). The coated samples were dried at room temperature followed by annealing at 70 ℃ for 30 min. The LTO ink was then spin coated at 1000 rpm for 1 min to complete the battery architecture. The assembled full cells were dried in vacuum oven at 60 ℃ for 2 hours to eliminate any protonic solvent. Upper aluminum charge collector (100 nm) was thermally evaporated onto LTO. The battery active footprint is defined by the overlapping area of cathode and anode charge collectors and is regulated to 20 mm^2.

3.2.7 Electrochemical characterization

All measurements were carried out in argon atmosphere. Data was collected on Maccor 440 and CHI660 electrochemical workstation. The ionic conductivity of PDMA-*co*-PEG$_{500}$/ LiClO$_4$ gel electrolyte was measured with Electrochemical Impedance Spectroscopy (EIS) in SS|GPE|SS configuration. To do this, 300 µL polymer solution (20 mgml^{-1}) was casted onto a piece of circular SS (diameter 0.5''). Film thickness was estimated to be 40 µm by assuming polymer density to be approximately 1.2 mgcm^{-3}. A drop of fresh liquid electrolyte was added to the dried film and the GPE was sandwiched between two pieces of SS spacers. All components were then sealed in a Swagelok cell.

EIS was conducted with potential amplitude of 10 mV between frequencies from 1 MHz

and 1Hz. Ionic conductivity is calculated based on Equation (3.1):

$$\sigma = \frac{L}{A \cdot R_b}$$
(3.1)

where σ, L, A and R_b are ionic conductivity, film thickness, SS area and bulk resistance.

For cyclic voltammetry and half-cell test of LMO microelectrode, the electrode was

immersed in 1M $LiClO_4$ in EC/DMC (1:1 v). A piece of lithium metal served as

counter/reference electrode. For full cell test, a drop of fresh electrolyte was added onto

the assembled microbattery. The microbattery was cycled between 1.4 V-3.0 V under

multiple C rates. EIS measurement of full cell was conducted in a frequency range from

100 kHz to 1 Hz, with an AC amplitude of 50 mV on Gamry 600 electrochemical

workstation.

3.3 Results and Discussion

In this work, LMO/LTO is chosen as the demonstrative electrochemical pair. The

well-defined electrochemistry enables us to more easily separates the influence of materials

system from that of the 3D structuring. In addition, both materials go through minimal

volumetric changes during the charge and discharge process,[61] which facilitates stable

cycling. Figure 3.2a shows the high-resolution transmission electron microscopic (TEM)

image of LMO nanoparticles. The particles are sub-10 nm in size. Elemental mapping by

energy-dispersive X-ray spectroscopy (EDX) shows that Mn and O are distributed

uniformly throughout the sample (Fig. 3.2b). Similarly, TEM imaging and elemental

mapping of the LTO nanoparticles are shown in Fig. 3.2c and 3.2d. To better characterized

the particle size and crystal structure, the nanoparticles were analyzed by Powder X-ray

diffraction (PXRD) in combination with Rietveld refinement using the MAUD software.[140] $LiMn_2O_4$ and $LiTi_5O_{12}$ spinel structures were used for modelling,[141-142] and the fits are shown in Fig. 3.2e and 3.2f. Both datasets show clear Bragg diffraction peaks indicating good crystallinity with significant peak broadening caused by the small crystallites. Both refinements yielded average crystallites sizes of ca. 6 nm with good agreement factors. The small particle size reduces ion diffusion length (L_{ion}), which greatly shortens the diffusion time (τ) and benefits the rate capability based on Equation (3.2),[57]

$$\tau = \frac{L_{ion}^2}{D_{ion}} \qquad\qquad (3.2)$$

The LMO data shows no indication of a bimodal particle size distribution or the common Mn_3O_4 impurity.[143] A minor impurity was observed in LTO diffraction patterns, the effect of which may be negligible. The electron diffraction (ED) patterns of LMO and LTO nanoparticles demonstrate a series of distinct diffraction rings, indicative of the polycrystalline features (Figure 3.3).
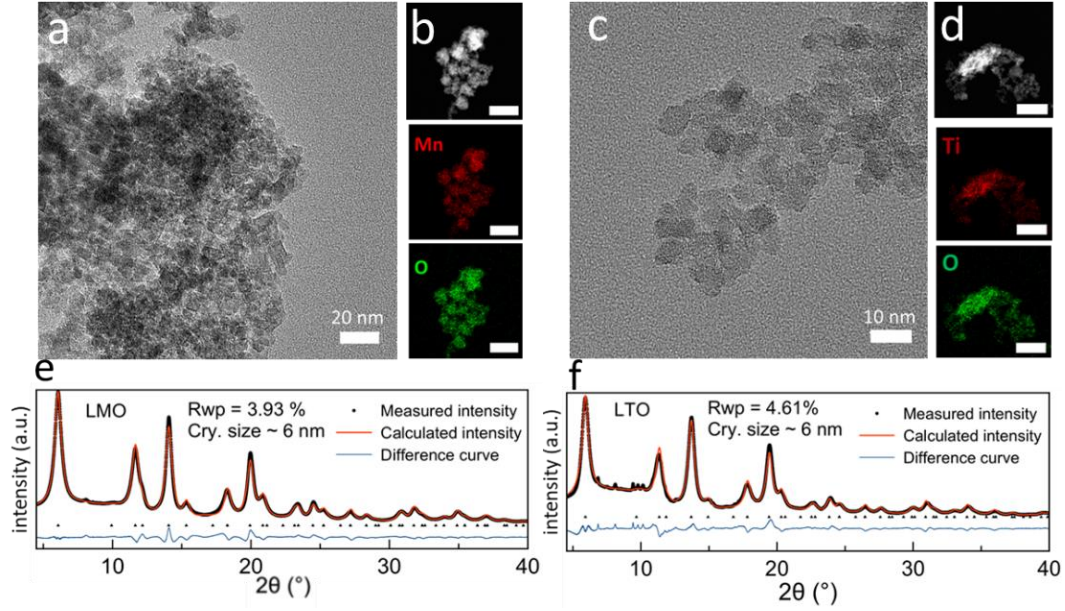
Figure 3.2 Characterizations of synthesized LMO, LTO nanoparticles. (a) TEM image and (b) EDX elemental mapping of LMO nanoparticles. Scale bar 300 nm. (c) TEM image and (d) EDX elemental mapping of LTO nanoparticles. Scale bar 300 nm. (e), (f) Rietveld refinements of LMO and LTO particles.

In this work, we fabricated the battery into interdigitated microcathode/anode array structure as illustrated in Figure 3.4. The interdigitated microelectrode array is analogous to a series of 2D batteries connected in parallel and transport between electrodes remains nearly one-dimensional when end effect is neglected. This will prevent the nonuniform current distribution within the electrochemical cell, which may lead to premature end of lithiation and delithiation.[5] A dimensionless number U is proposed (Equation (3.3)) to quantitatively measure uniformity of current,[78]

$$U = \left(\frac{w}{h}\right)^2 \left(\frac{\mu}{\sigma}\right) \left(\frac{1}{C}\right) \qquad (3.3)$$

where w and h are the width and height of the electrode as depicted in Fig. 3.4a. μ and σ are the mobility of Li$^+$ and electronic conductivity of electrode. C is the volumetric energy capacity. Clearly, both geometry and material properties have significant impacts. By

using higher aspect ratio (h/w) electrode and increasing its electronic conductivity, a smaller U, corresponding to more uniform current distribution in battery can be achieved.
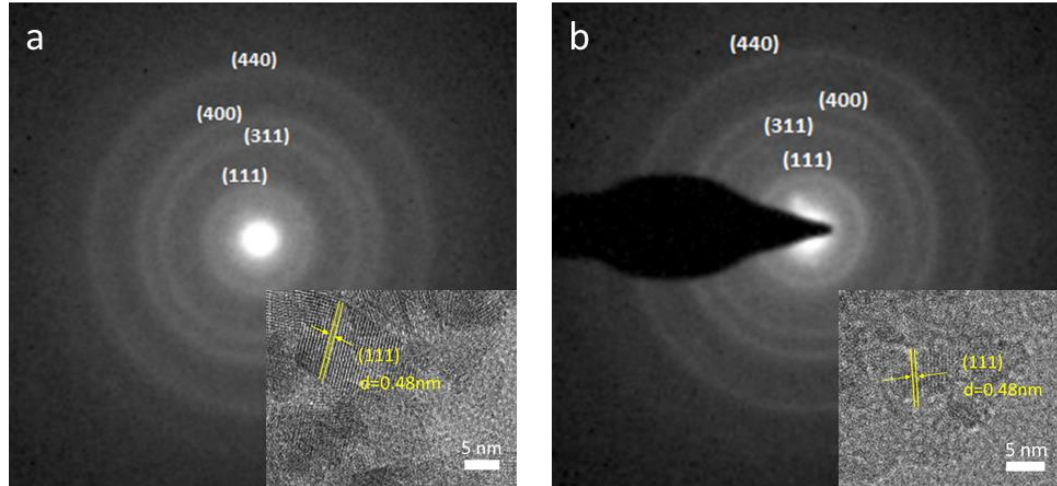
Figure 3.3 Electron diffraction (ED) pattern and high resolution TEM image of (a) LMO and (b) LTO nanoparticles.

The fabrication strategy is depicted in Figure 3.4b. To start, LMO microelectrodes are imprinted on an indium tin oxide (ITO) coated glass substrate using solvent-assisted imprinting (i). ITO serves as cathode charge collector. After thermal annealing in N_2 flow, the cathode array is coated LBL with drop casted PDMA-*co*-PEG$_{500}$ as separator/GPE (ii), and with an LTO/mesoporous carbon composite as counter electrode (iii). Finally, a thin layer of Al was thermally evaporated on top as anode charge collector (vi). The device active footprint is defined by the overlapping area of the two charge collectors and is 20 mm^2.
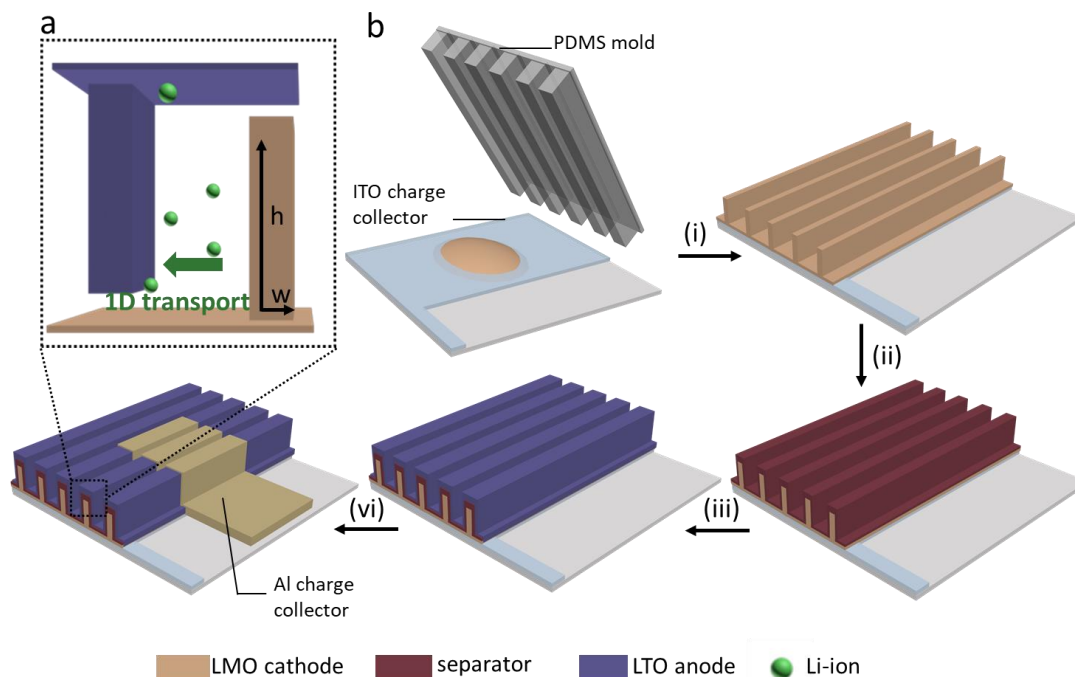
Figure 3.4 Schematic illustration of 1D transport in the interdigitated microelectrode array (a) and microbattery fabrication (b): (i) microcathode array fabrication via solvent-assisted capillary micromolding. (ii) Drop coating of PDMA-*co*-PEG$_{500}$ separator. (iii) Coating of LTO/mesoporous carbon counter electrode. (vi) Evaporation of Al charge collector.

To imprint the microcathode array, LMO nanoparticles were first dispersed in N-methyl-2-pyrrolidone. Optimum solid concentration and viscosity are crucial to provide imprintability. The as-synthesized LMO and LTO nanoparticles are both hydrophilic due to the abundance of surface -OH groups. LMO nanoparticles were stabilized by minimal 4-hydroxyl benzoic acid and the ink was stable for months (Figure 3.5a inset). The ink solid concentration was 10 wt% as confirmed by thermal gravimetric analysis (TGA). The ink possesses good fluidity and a low viscosity in the range of 1.8-3.2 mPa · s, which is on the same order of its solvent (1.6 mPa · s at room temperature). This is critical to efficient mass transfer in the capillary molding process,[14] especially when higher aspect ratio structures are targeted. Interestingly, the LMO ink exhibits a slight tendency of shear-thickening as shear rates exceed 10^2 s^{-1}. In a particulate suspension system, the onset shear

rate leading to shear thickening behavior, termed as critical shear rate, is dependent on particle size distribution, and bigger particles lead to smaller critical shear rates.[144] Dynamic light scattering (DLS) in Figure 3.5b shows that the volume- and number-averaged particle size in NMP are between 100-200 nm, which is much larger than individual particles observed under TEM, indicating that LMO nanoparticles may be stabilized in solvent as clusters. This might be a reason that the critical shear rate is smaller than expected for a dispersion of 6 nm particles. It is also noted that shear thickening only occurs when the suspensions are deflocculated. In other words, the interaction between stabilized clusters are nonaggregating. This may also explain the good stability of the imprint ink. Similarly, LTO was formulated with mesoporous carbon nanopowder and poly vinylpyrrolidone (PVP) in water/ethanol/ethylene glycol mixture solvent with a solid concentration of 10 wt%.
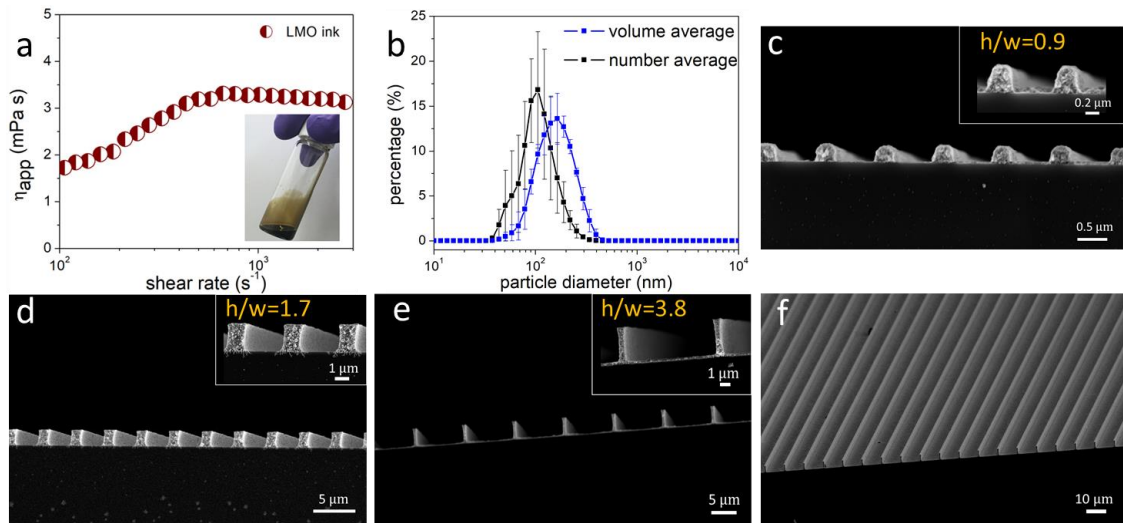
Figure 3.5 LMO Ink characterization and SEM images of imprinted structures. (a) Ink viscosity as a function of shear rates. (b) DLS measurement of LMO nanoparticles size distribution in NMP. (c) to (e) Cross-sectional SEM images of imprints of pattern A, B and C. Insets show the zoom-in images of imprinted features. (f) Top view of pattern C imprint on a larger scale.

In soft lithography, structure dimensions can be readily tuned by changing the dimensions of the master molds. Here, three sets of master molds were used. Their dimensions are 0.5 μm (w)-0.5 μm (h)-1.0 μm (p) (pattern A), 2 μm (w)-3 μm (h)-4 μm (p) (pattern B) and 2 μm (w)-5 μm (h)-10 μm (p) (pattern C) respectively (Figure 3.1). To imprint, LMO ink was cast onto substrate by mild spin coating followed by molding with a PDMS stamp. Drawn by capillary force, the ink rapidly filled the microchannels in the stamp. As solvent gradually permeated through PDMS upon soft bake, LMO microelectrode structure solidified for easy demolding. The imprints were further annealed in N_2 flow at 400 ℃ for 2 hours. During the process, any remaining organics degraded and left thin trace of carbon. In addition, the connectivity between LMO nanoparticles was strengthened and helped maintain structural integrity. The structures of imprinted LMO microelectrodes were characterized by scanning electron microscope (SEM) and are shown in Figure 3.5c to 3.5e. The final dimensions of pattern A, B and C are 0.42 μm (w)-0.39 μm (h)-0.97 μm (p), 1.1 μm (w)-1.9 μm (h)-3.9 μm (p) and 0.8 μm (w)-3.1 μm (h)-9.6 μm (p) respectively. The structure dimensions are generally smaller than their PDMS master molds due to volume shrinkage from solvent evaporation and thermal annealing.[102] Resultant aspect ratios of the imprinted A, B and C pattern are 0.9, 1.7 and 3.8. Based on previous discussion ($U \propto (\frac{h}{w})^{-2}$), pattern C should provide the most favourable performance among the three, although it imposes the biggest fabrication challenges for assembly. For demonstration purposes, we fabricated fully integrated microbattery with pattern C. Fig. 3f shows the electrode's top surface. The imprinted features have good structural registration regardless of the volume shrinkage, confirmed by the almost unchanged pitch size. Temperature series analysis of LMO by PXRD (Figure 3.6) shows

crystallite growth by the sharpening of diffraction peaks and no phase transition was detected.
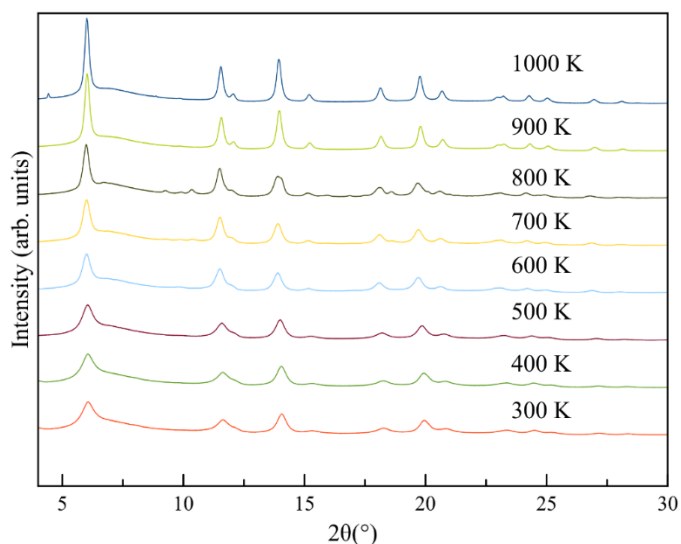
Figure 3.6 Temperature series PXRD analysis of LMO nanoparticles from 300 to 1000 K. No phase transition is observed.

Before integration, the electrochemical performance of the imprinted microelectrode (1 cm^2 footprint) was checked in a half-cell test, wherein lithium metal served as the counter/reference electrode. Figure 3.7a shows the cyclic voltammogram (CV) of LMO microelectrode under scan rates from 0.5 mV s^{-1} to 5 mV s^{-1}. At 0.5 mV s^{-1}, two distinct cathodic peaks at 4.13 and 4.0 V are observed, which agrees well with the two-step insertion of Li$^+$ into the LiMn$_2$O$_4$ matrix. Accordingly, anodic peaks at 4.02 V and 4.15 V correspond to the stepwise Li$^+$ extraction. The well-defined peak splitting can be attributed to the good crystallinity of LMO nanoparticles. It is noted that the potential difference between anodic and cathodic peak positions is small and only minor shifts are observed as scan rate increases. Both indicate good reversibility at the imprinted cathode. Although a small amount of organic acid was applied during ink formulation, we didn't observe

evidence of Li^+ loss from CV measurement,[145] as microelectrodes were imprinted from fresh inks. The galvanostatic discharging profiles of LMO microelectrode at different C rates are shown in Figure 3.7b. Here 1 C stands for complete discharging in 1 hour and n C corresponds to current density n times of 1 C. To highlight the significance of 3D patterning, a control sample was made from the same ink, spin coated at the same speed without patterning. Their normalized (to 1 C) capacities at different C rates are plotted in Figure 3.7c. The imprinted microelectrode demonstrates superior capacity retention and performs favorably relative to its nonpatterned counterpart. Under current density as high as 100 C, the nonpatterned electrode almost failed to deliver any meaningful capacity while the microelectrode still retained 50% of its 1 C performance. The electrode structure was stable as confirmed by the recovery of capacity when current was reduced back to 3 C. The difference may be attributed to easier bulk diffusion of Li^+ in the patterned system, which agrees with previous reports.[137, 146] The electrochemical properties of the LTO nanoparticles were also characterized by cyclic voltammetry and galvanostatic charge/discharge, where good reactivity was demonstrated by distinct redox peaks at 1.45 V and 1.72 V with reversible capacity of 151.6 mAhg^{-1}. (Figure 3.8).
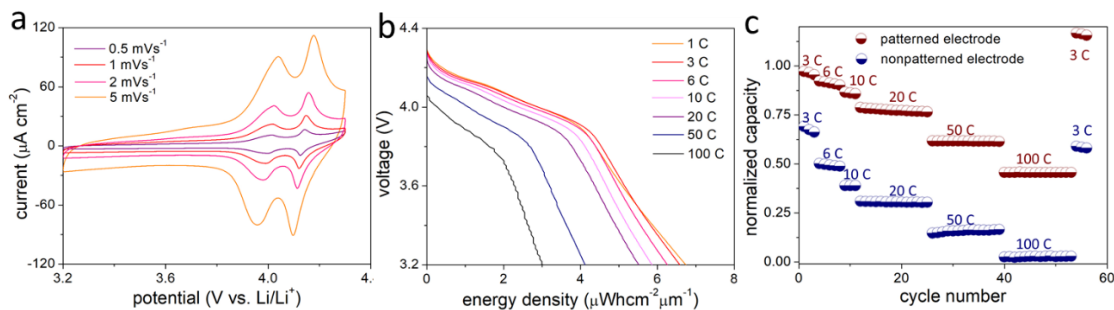
Figure 3.7 Electrochemical characterizations of imprinted LMO cathode. (a) Cyclic voltammogram of LMO electrode at various scan rates. (b) Discharging profiles of LMO electrode under different C rates between 3.2-4.4 V. (c) Comparison of rate capability of patterned and nonpatterned LMO electrodes.

One challenge for assembling a stacked microbattery architecture is to choose the appropriate separator and coating strategy. It is important that separator forms a robust and full coverage layer on the cathode array to ensure stable operation without shorting. In addition, it should facilitate rapid ion transport to achieve high-power performance.
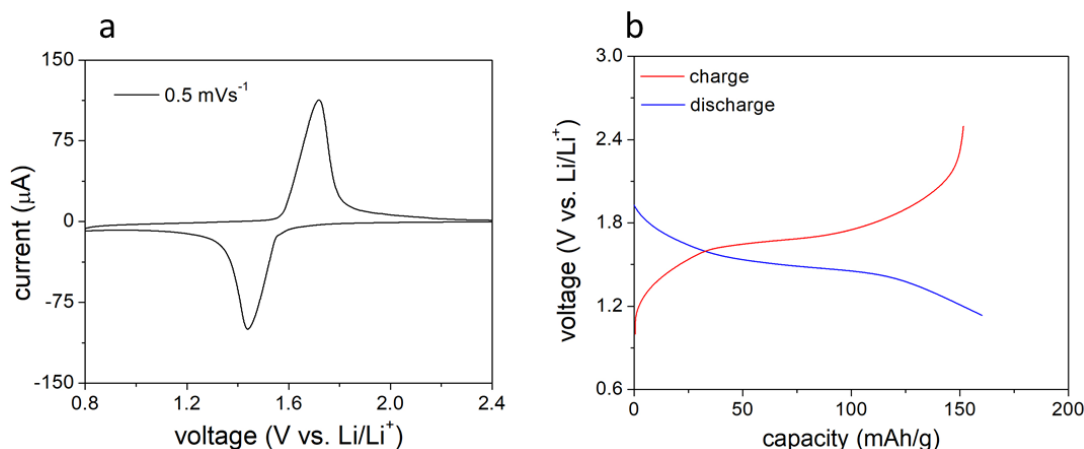
Figure 3.8 Electrochemical characterization of LTO nanoparticles. (a) cyclic voltammetry of LTO. (b) galvanostatic charge and discharge profiles in a Swagelok cell.

In this work, we synthesized PDMA-*co*-PEG$_{500}$ copolymer as the separator and subsequently the matrix for GPE after complexation with LiClO$_4$ (EC/DMC) liquid electrolyte. The design of this copolymer is based on the considerations of both coating properties and ionic conductivity. The chemical structure and synthesis steps are shown in Figure 3.9a. The copolymer has a molecular weight of 750 kgmol^{-1} and the molar ratio of DMA to PEG$_{500}$ is approximately 1:2.6, as confirmed by gel permeation chromatography (GPC) and ^{1}H NMR (Figure 3.10).
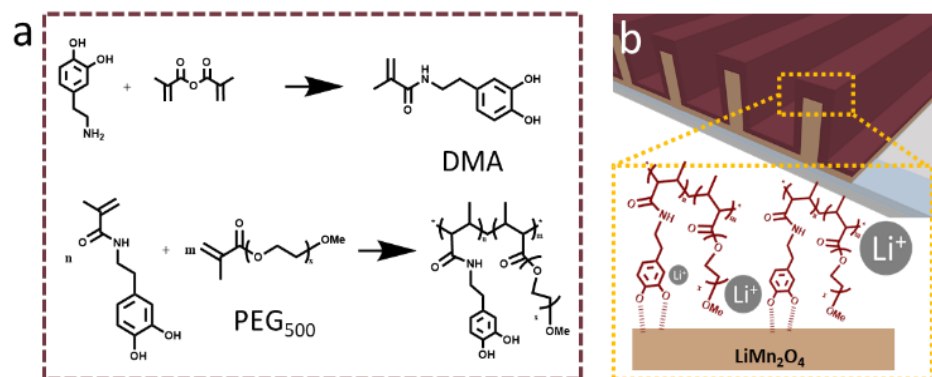
Figure 3.9 (a) Synthesis of PDMA-*co*-PEG₅₀₀ copolymer and (b) schematic illustration of catechol binding with metal oxide surface.
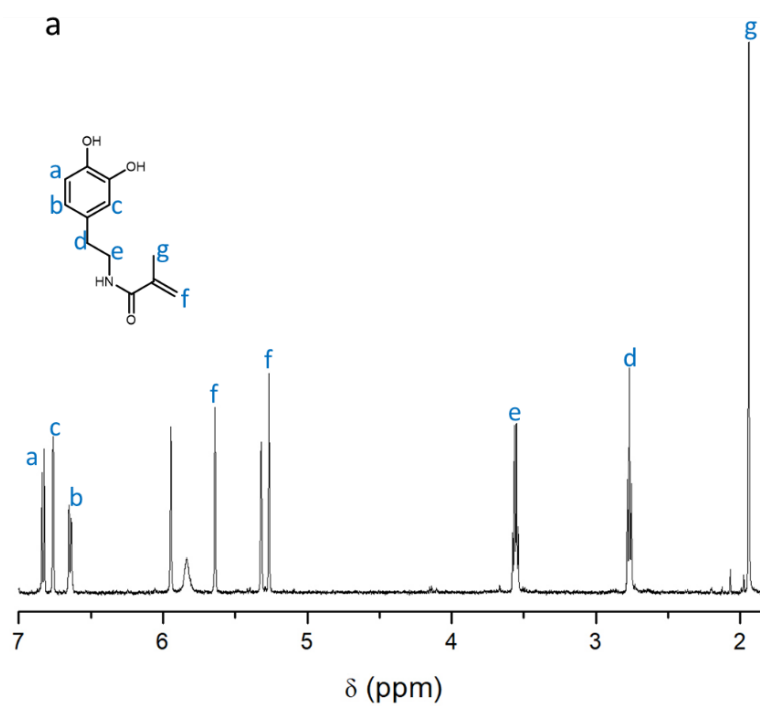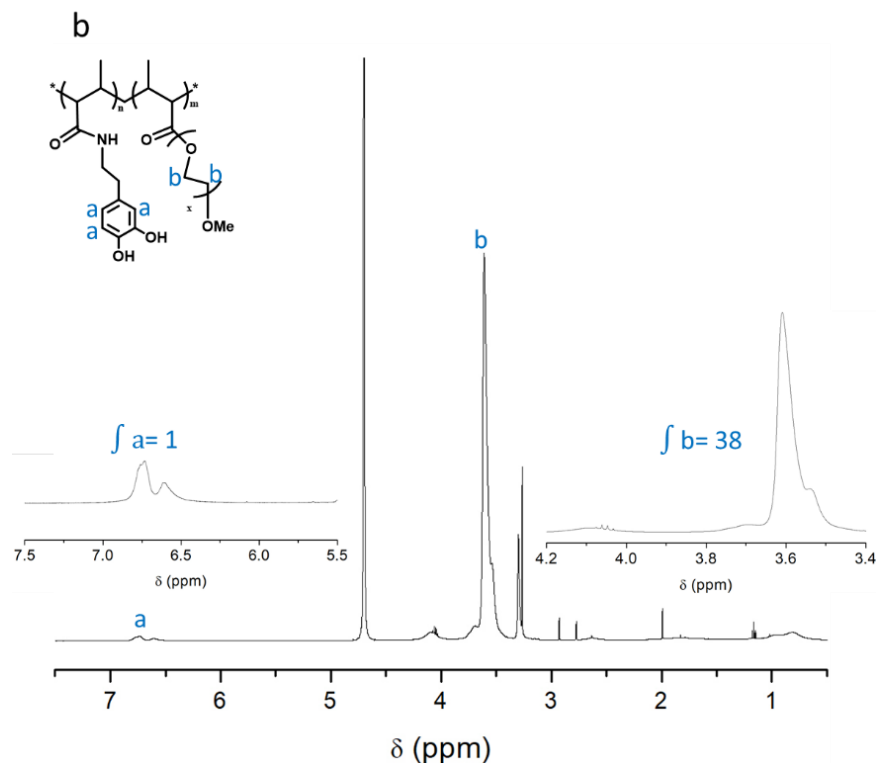
Figure 3.10 ^{1}H NMR spectrum of (a) DMA monomer and (b) PDMA-co-PEG$_{500}$ copolymer. Integrated peak area of a to b is 1 to 38 (MasterRenova), corresponding to molar ratio n(DMA): n (PEG$_{500}$) of 1:2.6. Note that the feeding ratio of these two comonomers is approximately 1:2. There slight deviation between the feeding ratio and final composition is acceptable as a result of monomer reactivity difference.

The incorporation of dopamine methyl acrylamide is inspired by the superior adhesion of polydopamine to versatile surfaces.[147] Specifically, the strong interaction between catechol and metal oxide surfaces enables intimate contact of separator and cathode as depicted in Figure 3.9b. To demonstrate the binding between copolymer and LMO, we compared the IR absorption peaks of neat LMO particles, PDMA-*co*-PEG$_{500}$, and the polymer binded particles. As shown in Figure 3.11a, the emerging of distinct absorption at 1100 cm^{-1} on polymer binded LMO corresponds to C-OH stretching in catechol. Characteristic absorption from ester C=O at 1720 cm^{-1} can be also seen on particles after polymer coating. Interestingly, signs of polymer C-O stretching peaks (1248-1281 cm^{-1})

merging into one band after coated on LMO particles are observed, indicating that bidentate binding of catechol onto LMO surface may exist.[148]
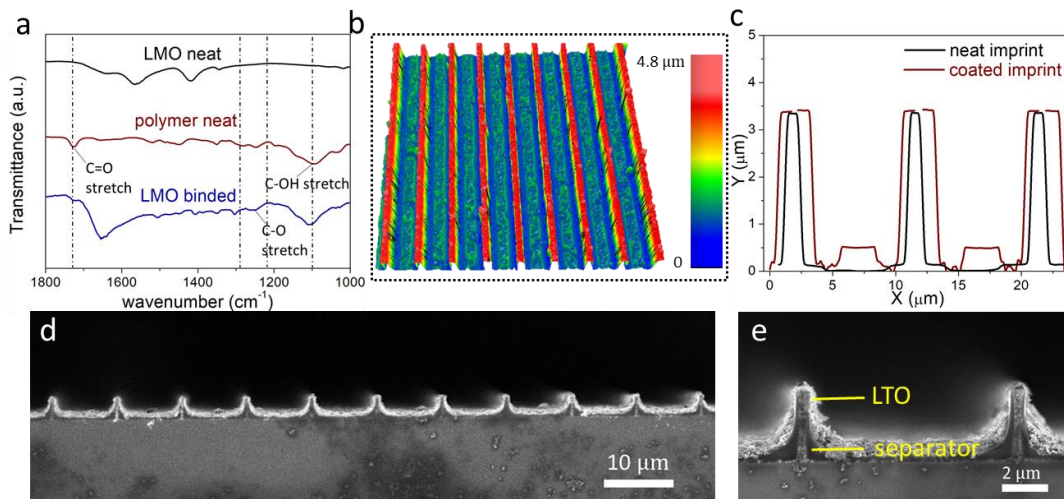
Figure 3.11 Characterizations of PDMA-*co*-PEG$_{500}$ copolymer and the coated microelectrode architectures. (a) IR spectra of neat LMO nanoparticles, PDMA-*co*-PEG$_{500}$ copolymer and the polymer coated nanoparticles. (b) Optical profilometry image of separator coated cathode array. (c) Height profiles of cathode array before and after separator coating. (d) Cross-sectional SEM image of fully assembled microbattery. (e) Zoom-in SEM image of integrated microbattery architecture.

To coat polymer onto LMO microelectrodes, PDMA-*co*-PEG$_{500}$ was dissolved in ethanol and the deposition was done by simple drop cast. The surface morphology and height profile after coating were imaged by optical profilometry and are shown in Figure 3.11b and 3.11c. As ethanol evaporated by mild heating (60℃), the copolymer covered the LMO microelectrodes on both the top surface and vertical side wall. We attribute this to the "sticky" feature of dopamine containing polymers.[149] Moreover, the electrode's aspect ratio was well maintained. We notice however, that the polymer coating is not completely conformal. Thickness varies from 60 nm on top to 1 μm on the side wall. This is due to effects of gravity during the coating. To improve coating conformality in the future, vapor phase polymerization and controlled spray coating may be viable routes and are under

investigation. In fact, the length of electron tunneling is in the order of 1 nm and Long *et al* reported that with 10 nm separator film, electron tunneling between surfaces may be negligible.[78] We have far exceeded this thickness and direct shorting should be avoided.

The battery was fully integrated using an LTO/mesoporous carbon suspension spin coated on top of the separator structure as counter electrode. SEM cross-sectional images of the full cell are shown in Figure 3.11d and 3.11e. No thermal treatment was needed for LTO because the nanoparticle possessed the desired crystal structure as synthesized. The final height of microbattery was approximately 3.5 μm and the cell volume was 0.07 mm^3, which included the volume of electrode plates and the space in between. This device-based volume is used for the calculation of energy and power densities. Notably, no surface treatments, e.g. oxygen plasma or UV-ozone were needed before LTO coating as PDMA-co-PEG$_{500}$ is hydrophilic in nature. The contact angle with water is 34°, which is comparable to polydopamine.[150] This is important regarding film integrity as oxygen plasma is destructive to most polymers and may induce defects in coating.

Conventionally, a GPE is prepared by casting polymer/liquid electrolyte mixture into a thin film. However, in our cell configuration, lithiation of GPE is completed by adding liquid electrolyte on top of the assembled microbattery. This allows us to deal with the moisture-sensitive electrolyte only at the last step. This strategy, on the other hand, places stricter requirement on polymer crystallinity. Conceivably, conventional polymer matrices, e.g. PVDF and high molecular weight (> 20 kg mol^{-1}) linear PEO, are not suitable as liquid electrolyte hardly permeates the crystalline film at room temperature. In this work, the copolymer that is comprised of low molecular weight (500 g mol^{-1}) PEG side chains on polymethacrylate backbone, avoids the problem with its non-crystalline feature.

Impedance plots of lithiated copolymer film together with two controls, a commercial Celgard 2500 separator and a PVDF film are shown in Figure 3.12a. The tests were conducted by using stainless steel (SS) as blocking electrodes. A large semicircle in high-frequency region is observed in PVDF-based GPE, corresponding to grain boundary effects in non-homogeneous, crystallized phases. After overnight soaking, bulk resistance of PVDF-GPE slightly decreased as indicated by the shrinkage of semicircle diameter. This is a sign of the sluggish permeation of liquid electrolyte. On the contrary, the complete disappearance of semicircle in PDMA-co-PEG$_{500}$ impedance plot is indicative of non-crystallinity,[151] which is consistent with the DSC measurement. The impedance profile resembles the liquid electrolyte in microporous Celgard separator. The ionic conductivity is estimated to be 0.03 mS cm^{-1} at room temperature. The conductivity value is 2 to 3 magnitudes larger than previously reported nanoscale electrolytes and may well compensate for the coating thickness variation.[152-153]

Electrochemical performances of integrated microbattery were characterized galvanostatically between 3.0-1.4 V. A drop of fresh liquid electrolyte was added on top of the battery in an argon-filled glovebox and the microbattery was sealed in a plastic container. Two copper clips were connected to ITO and Al charge collector. Figure 3.12b shows a microbattery wired to an outer circuit lighting up a red LED. Voltage profiles of a microbattery charged and discharged at 5 C current are shown in Figure 3.12c. The profiles demonstrate distinct plateaus between 2.3 V and 2.9 V, which corresponds well with the electrochemistry based on LMO/LTO redox pair. A two-stage process can be observed in both charging and discharging. The process is clearly shown from the differential capacity curves (Figure 3.12d).
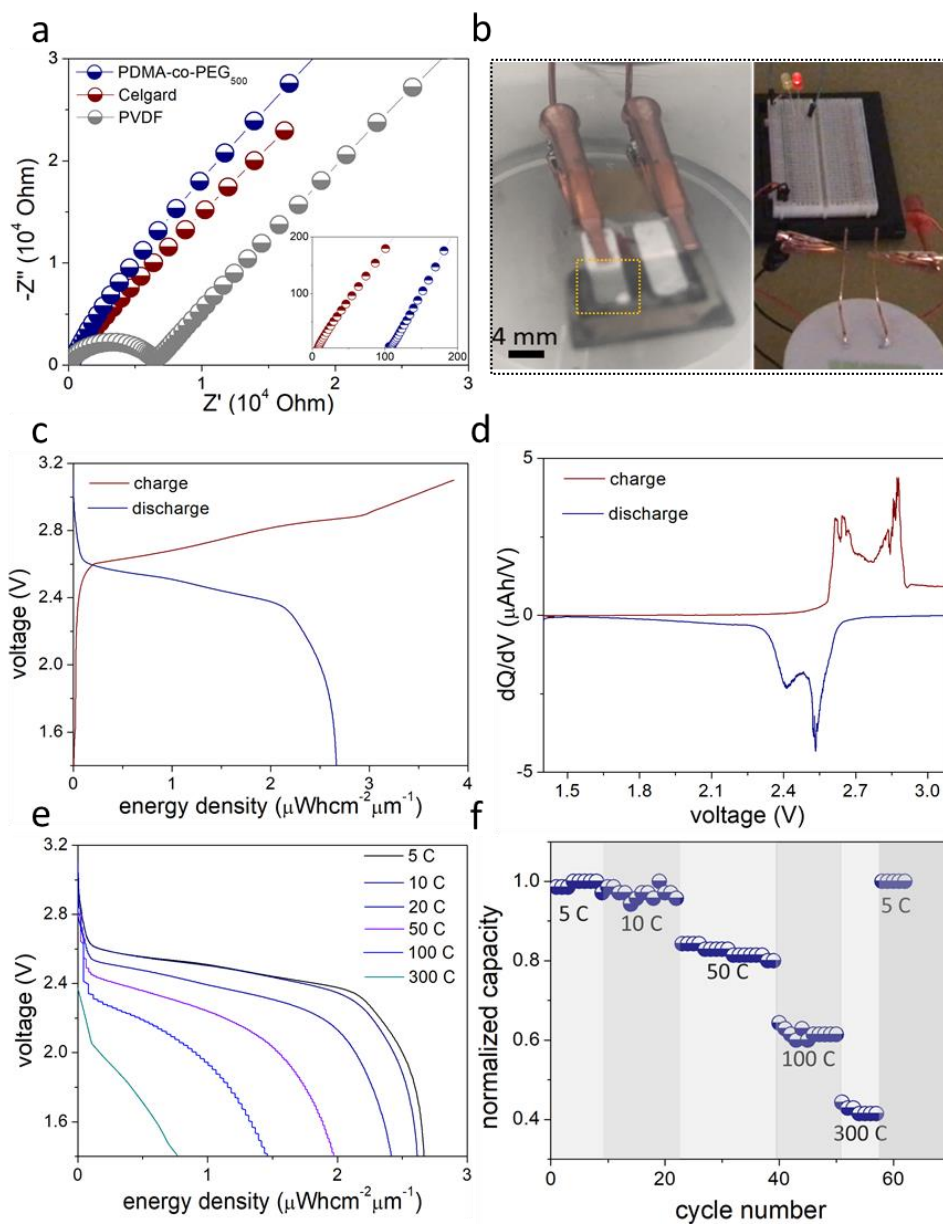
Figure 3.12 Electrochemical characterizations of microbattery. (a) Impedance spectra of Celgard, PDMA-*co*-PEG$_{500}$ and PVDF in SS|GPE|SS symmetric cell. (b) Optical image of the assembled microbattery lighting up a red LED. (c) Charging/discharging profiles of microbattery at 5 C. (d) Differential capacity curves of microbattery charging and discharging. (e) Discharging profiles of microbattery under increasing C rates from 5 C to 300 C. (e) Normalized (to 5 C) discharging capacity as a function of cycle number.

Sharp peaks at 2.64 V, 2.86 V in charging and 2.41 V, 2.53 V in discharging correspond to

Li$^+$ insertion/extraction, which is consistent with cyclic voltammetry of the LMO

microelectrode. AC impedance measurement of full cell was conducted, and the charge

resistance was approximately 0.5 kΩ after 5 cycles (Figure 3.13a). The impedance profile shows semicircular features in the high frequency region, corresponding to charge transfer resistance, and a spur in the lower frequency region resulting from diffusion related Warburg impedance. In our system, the separation length of the two electrodes is much smaller than conventional battery system and thus we modified our equivalent circuit model (Figure 3.13a inset) accordingly by including the bounded Warburg impedance and the double layer capacitance. The charge transfer resistance increased to 1.3 kΩ after 100 cycles, which may be induced by the weakened contact between LTO and the evaporated Al layer as the cycling test proceeded. The formation of SEI at multiple interfaces may also cause the resistance to increase. At 5 C, the microbattery possesses a volumetric energy density of 2.7 μWhcm$^{-2}\mu$m^{-1}. We notice that in charging, a larger storage energy density of 3.8 μWhcm$^{-2}\mu$m^{-1} is obtained. The Coulombic efficiency of the process started at 80.4% and later stabilized at 88.7% (Figure 3.13b). We suspect that the efficiency deviation from 100% may result from a minor leaking current. XPS measurement confirmed that after copolymer coating, surface elements changed from Li, Mn, O to C, N, O, indicating full coverage with a separator thickness exceeding the electron tunneling length and direct shorting may be avoided. But the electrodes may still interact through either "soft contact" as a result of separator dimension change or overlapping of the electrodes' electrical double layers when they are in close proximity. This issue may be solved by optimizing the coating strategy to ensure coating conformality and thickness control. We exclude the possibility of side reactions from the differential curve shown in Figure 3.12d, as no peaks corresponding to side reactions can be observed. Figure 3.12e shows the voltage profiles of microbattery charged at 5 C and discharged at different current densities. At 10 C

56

discharging, the microbattery shows little capacity decay, demonstrating an almost overlapped voltage profile and an energy density of 2.6 μWhcm^{-2}μm^{-1}. Notably, the voltage profiles from 5 C to 100 C all demonstrate distinct plateaus, indicating good diffusion-reaction kinetics. At 300 C, the battery still retains 28.8% of its 5 C energy (equivalent of 40% capacity retention) and generates a power density as high as 855.5 μWcm^{-2}μm^{-1}. Figure 3.12f presents the normalized discharge capacities at varied C rates as a function of cycle numbers. The microbattery exhibits strong rate capability and almost full capacity retention when going back to lower rate discharging, indicative of robust cycling ability.
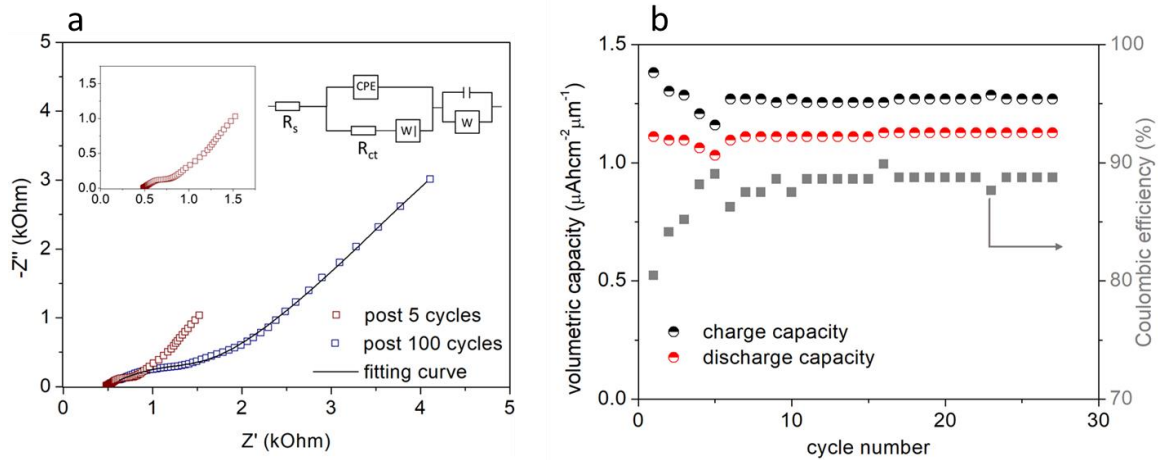
Figure 3.13 (a) EIS of full microbattery after 5 times and 100 times cycling tests. (b) Volumetric capacity and Coulombic efficiency as a function of cycle number.

The Ragone plot in Figure 3.14 compares the volumetric energy and power density of our microbattery with other micro energy-storage devices reported from recent literatures.[89, 123, 126-127, 154-158] It can be clearly seen that microbatteries generally have higher energy density but suffer from drastic energy fading as power goes up. On the contrary, microsupercapacitors are able to generate high power and good capacity retention but provide much smaller energy density. The microbattery presented in this work is among some of the rare reports of micro energy storage systems that possess battery-level energy

density and high-power density comparable to some of the best supercapacitors. We believe that the high-power performance of the microbattery is attributed to the synergetic effects from delicate preparation of electrode nanoparticles, the 3D engineering of imprinted electrodes, the unique copolymer gel electrolyte and its intimate contact with the electrodes.
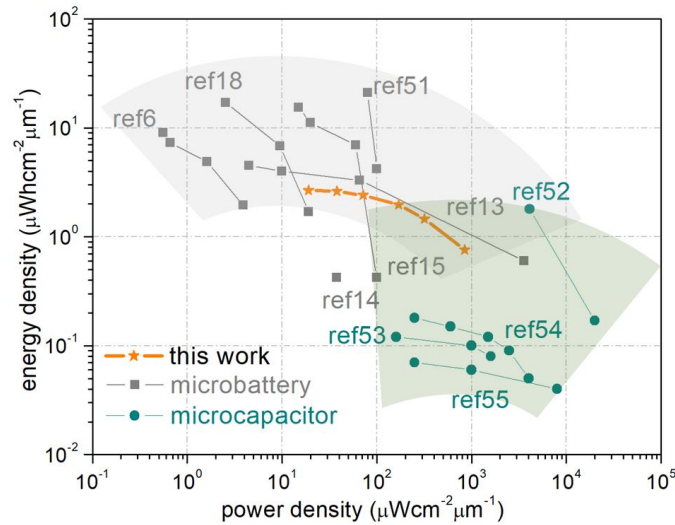
Figure 3.14 Comparison of volumetric energy and power densities of this work to reported micro energy storage devices (microbatteries and microsupercapacitors) from recent literatures in a Ragone plot.

3.4 Conclusions and Future Work

In summary, we have demonstrated a 3D lithium-ion microbattery based on imprinted microelectrodes and integrated through layer-by-layer stacking. The delicate size of LMO, LTO nanocrystals, together with the well-engineered device architecture, enables the battery to display supercapacitor-like power density. A remaining challenge as discussed, is the conformal coating of a solid/gel electrolyte on 3D electrode which effectively avoids electrode contact and facilitates fast ionic transport at the same time. This calls for further investigation in the materials selection and coating strategy. In addition, the energy density of microbattery may be improved further by imprinting with

molds of even higher aspect ratios, and denser microarrays. The facile fabrication of electrodes and layer-by-layer integration described here can be potentially extended to other electrochemical systems.

CHAPTER 4

INITIATED CHEMICAL VAPOR DEPOSITION OF COPOLYMER THIN FILMS AS MICROBATTERY ELECTROLYTES

4.1 Introduction

Microbatteries based on 3D electrode architectures have potential to serve as integrated power sources for autonomous microscale devices. Nonplanar electrode geometries enable high active material loadings and large surface-to-volume ratios, resulting in simultaneously enhanced energy and power densities.[78, 159-160] Over the years, 3D electrodes of different forms have been reported, including vertically aligned nanowires/pillars,[88] multilayered stacks,[137] and nanoporous monoliths.[32] However, the long-standing challenge of conformal, defect-free coating of nanoscale electrolytes with good ionic conductivities onto 3D electrodes renders the successful integration of microbattery full cells elusive. Both the coating strategy and the choice of materials must be addressed to meet this challenge.

Polymer films can be converted into gel and solid-state ionic conductors for lithium-ion batteries by solution-based doping with lithium salts.[161] Successful demonstrations have been reported using stepwise strategies of applying a polymer coating that is subsequently doped. For example, poly(methyl methacrylate) (PMMA) and SU-8 based gel polymer electrolytes (GPEs) on micropillar/line arrays were achieved with cleanroom lithographic techniques.[162-163] Solution casting of polymer electrolytes functionalized with hydroxyl groups are also shown as a viable route to achieve complete coverage on 3D electrode architectures.[80, 160] To realize form factor-free deposition of polymers onto arbitrary 3D geometries, poly(phenylene oxide) (PPO) and a poly(1,3,5-

trivinyl-1,3,5-trimethylcyclotrisiloxane) (PV3D3) were electrodeposited to achieve self-limiting coatings on porous electrodes,[84, 164-165] but the moderate ionic conductivity (10^{-10} S cm^{-1}) leaves significant space for further improvement. In the realm of conformal polymer coatings, initiated chemical vapor deposition (iCVD) has attracted attention as a platform deposition technique because of its precise control of film thickness, low-temperature operation, and compatibility with a wide range of functional monomers.[23] Previously, Gleason and co-workers reported an ultrathin, poly(1,3,5,7-trtravinyl-1,3,5,7-tetramethylcyclotetrasiloxane) (PV4D4) based SPE from iCVD with ionic conductivities in the order of 10^{-8}-10^{-7} S cm^{-1}.[152, 166]

To date, the field has almost exclusively studied homopolymer matrices for use in nanoscale SPEs, which imposes rigorous requirements on one monomer species to meet challenges from both coating and ionic conduction. These requirements limit the choice of monomers and narrow the tunability window of the resultant polymer matrices with respect to the cross-linking density, polarity, and chain mobility. For macroscopic SPEs, polymer blends, *e.g.* PEO/PMMA and poly(acrylonitrile) (PAN)/polyethylene imine, were shown to improve conductivity significantly from their single component matrix counterparts.[73-74, 167] Inspired by this result, we utilized the iCVD method to fabricate a class of 3D conformally coated, nanoscale SPEs based on a series of copolymer thin films with LiTFSI doping. Our design principles are that one monomer is multifunctional providing the necessary cross-links to stabilize the copolymer films during solution doping, while a second monomer is systematically incorporated to fine-tune the chemical and physical properties and, consequently, ionic conductivity.

Here, we selected ethylene glycol diacrylate (EGDA) as the cross-linker due to its well-studied reaction kinetics in iCVD and more importantly,[168-169] its chemical similarity to some of the benchmark precursors used in SPEs and GPEs, such as trimethylolpropane ethoxylate triacrylate (ETPTA).[170-171] The low volatility of ETPTA prevents its use in iCVD directly. Hydroxyethyl methacrylate (HEMA) is used as the comonomer to decrease the film cross-linking density. In addition, the presence of the hydroxyl groups promotes strong interaction with anions, thus enhancing the dissociation of lithium salts.[167] Utilizing copolymer matrices enables decoupling the cross-linking agent from the comonomer that tunes the chemical composition and physical properties, which ultimately optimizes ionic conduction in nanoscale SPEs.

4.2 Experimental Section

4.2.1 Initiated Chemical Vapor Deposition of Copolymer Thin Films

Copolymer thin films were deposited using a custom-built iCVD chamber (GVD Corp.). Substrates were placed on a temperature-controlled stage, maintained at 26 ℃. All chemicals, *i.e.* tert-butyl peroxide initiator (Sigma-Aldrich, 98%), HEMA (Acros Organics, 97%) and EGDA (Acros Organics, 90%), were used as received without purification. Deposition conditions including precursor flow rates, reactor pressure, and the corresponding deposition rate are specified in Table 4.1. The temperature of the heating filament array was maintained at approximately 200 ℃, and the deposition thickness was monitored by *in-situ* interferometry.

Table 4.1. iCVD deposition conditions for poly(HEMA-*co*-EGDA).

sample	HEMA (mol%)	f_{TBPO} (sccm)	f_{HEMA} (sccm)	f_{EGDA} (sccm)	P (mTorr)	P_{HEMA}/P_{sat}	P_{EGDA}/P_{sat}	dep. rate (nm/min)
CP10	9.0 ± 1.8	1.0	0.8	2.8	120	0.15	0.72	30
CP40	37.0 ± 5.7	0.8	0.8	2.0	120	0.20	0.65	18
CP55	55.7 ± 3.5	1.2	2.3	2.2	80	0.24	0.30	12
CP85	85.9 ± 3.9	1.0	2.0	1.1	80	0.29	0.21	14
CP95	95.3 ± 4.2	1.0	2.5	0.8	80	0.34	0.14	13

4.2.2 Imprinting of TiO₂ Based 3D Nanostructures

The fabrication of TiO$_2$ 3D structures was reported by us previously.[102] In brief, a commercial TiO$_2$ (US Research Nanomaterials, Inc) dispersion with 15 nm nanoparticles in 1,2-propanediol was first diluted with additional 1,2-propanediol and methanol in a 1:1:5 weight ratio to achieve approximately a 3.0 wt% solid concentration. The diluted ink was spin coated onto cleaned silicon wafer, followed by molding with a poly(dimethyl siloxane) (PDMS) stamp with predesigned patterns, *e.g*., the reverse patterns of nanopore, nanoposts, etc. After a short-time soft baking to remove residual solvent, the 3D patterns were obtained upon demolding.

4.2.3 Physical Characterization

FT-IR analysis was performed on copolymer collected from the iCVD deposition chamber using a PerkinElmer FT-IR spectrometer with a universal ATR sampling accessory. Surface morphologies of the CP and CSE series were imaged by a Dimension 3100 AFM. Cross-sectional imaging and EDX analysis of CSE films were carried out on a Magellan 400 SEM facility. Film thickness was measured with a Dektak 150 surface profiler. TGA was performed between room temperature and 600 ℃ under nitrogen (ramping rate at 10 ℃ min^{-1}) and the DSC analysis was conducted between -60 ℃ and 150 ℃ (scanning rate 10 ℃ min^{-1}). The dielectric constant was measured with an impedance

meter (Keithley Inc.) between 10^2 to 10^5 Hz, with an AC amplitude of 50 mV in a N_2 filled glovebox. Electronic conductivities of the copolymer thin films were measured on a CHI660 electrochemical workstation by a cyclic voltage scan between 0.1 V and -0.1 V.

4.2.4 Preparation and characterization copolymer solid-state electrolytes

Copolymer films with different composition that were deposited on ITO substrates were dried overnight at 85 ℃ under vacuum. Gold electrodes (50 nm thickness) with shadow mask-defined contact area (6 mm^2) were thermally evaporated (1-2 nm min^{-1}) onto the polymer films. These samples were then transferred into an Argon-filled glove box and soaked in a LiTFSI solution (0.3 M in acetonitrile) overnight to induce salt doping. Thin film solid-state electrolytes were obtained after drying the film on a hot plate (120 ℃, 1 h) to remove any residual solvent. Electrochemical impedance spectroscopy (EIS) was performed on a Gamry 600 electrochemical test station between 10^6 Hz to 1 Hz, with AC amplitude of 50 mV and 0 V bias.

4.3 Results and Discussion

The fabrication of copolymer electrolytes is depicted in Figure 4.1a. Indium tin oxide (ITO) coated glass and imprinted TiO_2 3D electrodes are placed together in the iCVD chamber to produce 2D and 3D coated thin films. Experimental details for imprinting 3D substrates and depositing the copolymer thin films via iCVD are described in the Supporting Information. The copolymer film composition was systematically varied by adjusting deposition parameters in the iCVD process. As documented previously, deposition rate depends on monomer adsorption to the substrate surface, which can be described by the ratio of the monomer partial pressure to the saturated pressure (P_M/P_{sat}).[24] The copolymer composition was systematically varied by tuning the P_M/P_{sat} values of

HEMA and EGDA (Table 4.1). FT-IR spectra of copolymer films with different composition are shown in Figure 4.1b. Characteristic absorption peaks indicate the retention of hydroxyl groups (3400 cm^{-1}) in HEMA and carbonyl groups (1710 cm^{-1}) present in both HEMA and EGDA.[168] The concentration of HEMA was calculated based on the absorption peak areas (A) using Equation 4.1:
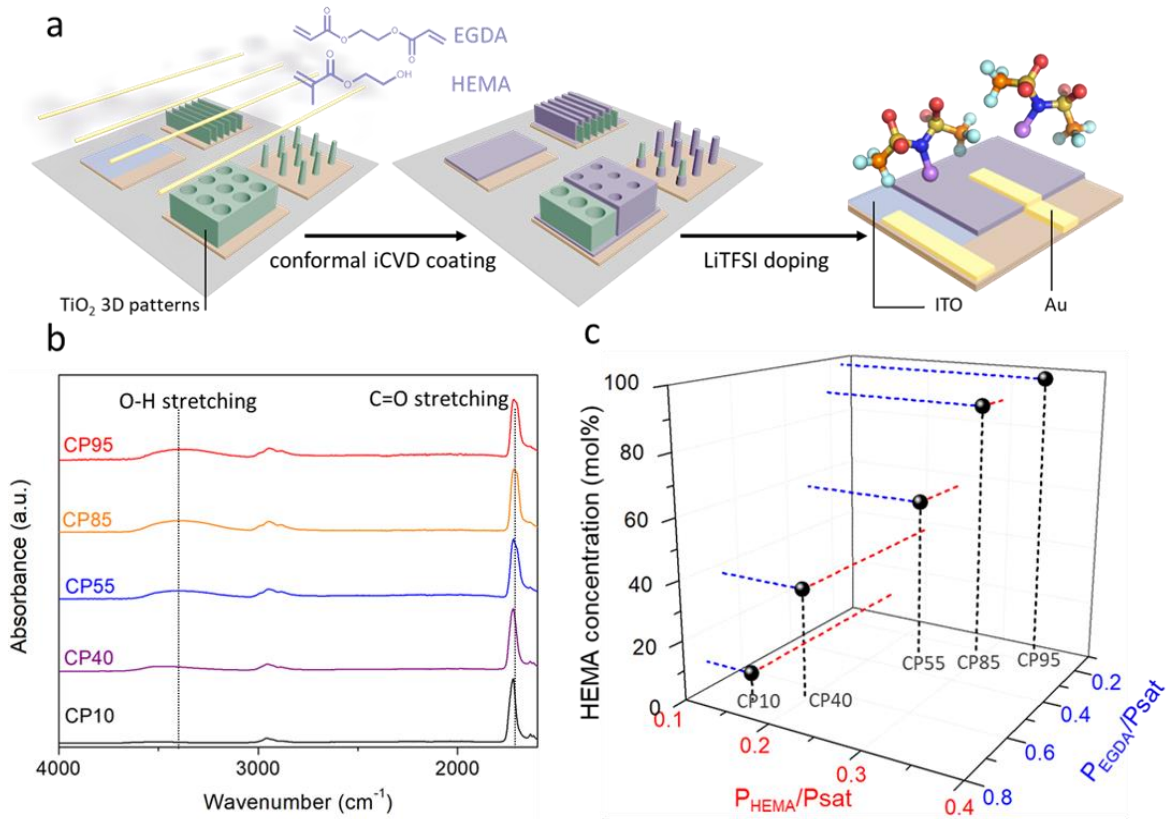
Figure 4.1 (a) Schematic illustration of solid-state copolymer electrolytes preparation and the conformal coating of copolymers on 3D substrates. (b) FT-IR absorbance spectra of poly(HEMA-*co*-EGDA) films with different compositions. The wide band centered at 3400 cm^{-1} and the sharp peak at 1710 cm^{-1} correspond to O-H and C=O stretching respectively. (c) HEMA concentration in deposited copolymer films as a function of P_M/P_{sat} for HEMA and for EGDA. The red and blue projections specify the compositional change with P_{HEMA}/P_{sat} and P_{EGDA}/P_{sat}, respectively.

$$\frac{[HEMA]}{[HEMA]+[EGDA]} = \frac{rA_{O-H}}{rA_{O-H}+(A_{C=O}-rA_{O-H})/2} \tag{4.1}$$

where r is defined as $A_{C=O}/A_{O-H}$ in homopolymer poly(HEMA). We obtained a series of copolymer films, containing 9.0 ± 1.8, 37.0 ± 5.7, 55.7 ± 3.5, 85.9 ± 3.9 and 95.3 ± 4.2 mol% HEMA, referred to as CP10, CP40, CP55, CP85 and CP95, respectively (Figure 1c). TGA analysis of the copolymer series provides additional evidence for compositional change (Figure 4.2) as the onset decomposition temperature gradually decreases from 350 to 200 °C with increasing HEMA concentration.
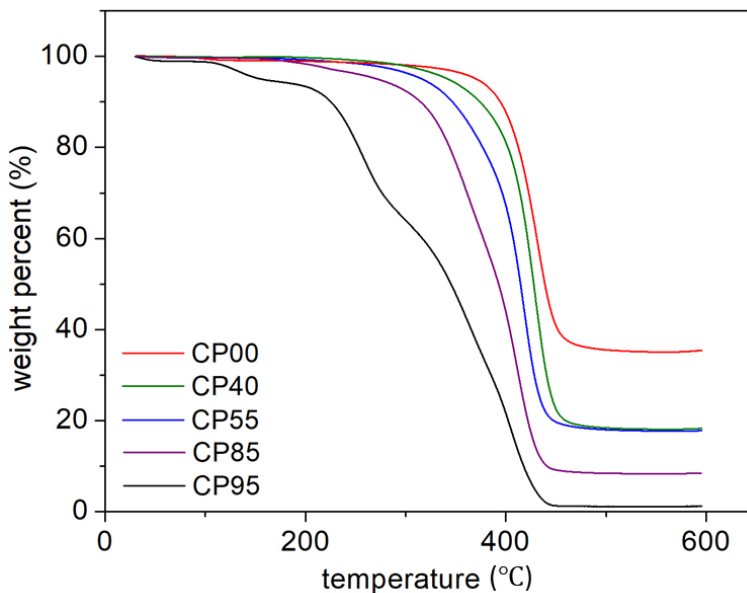
Figure 4.2 TGA traces of the copolymer series. All experiments were conducted under N_2 purge between 30 and 600 °C.

To demonstrate the 3D conformal coating capability, we show SEM images of the copolymer films on a variety of 3D geometries in Figure 4.3. For demonstration purposes, only copolymers with composition at the two ends of the composition range (CP10 and CP95) were used. The surface texture changed distinctly from the relatively rough metal oxide surface to a much smoother polymer surface. The root-mean-square roughness (R_{rms}) for as-deposited copolymer films on a silicon wafer is 0.63 nm, confirmed by AFM analysis. We achieved conformal, nanoscale coating onto a broad spectrum of geometries with

different dimensions and aspect ratios, including nanopillars, nanopores, nanolines and microline arrays. Precise thickness control from 30 to 300 nm can be achieved, with minimal thickness variation across the substrate. Energy-dispersive X-ray spectroscopy (EDX) mapping of carbon and titanium further confirms the conformal deposition of the copolymer on 3D microstructures (Figure 4.4). These results suggest the materials are promising polymer separators for 3D microbattery architectures.
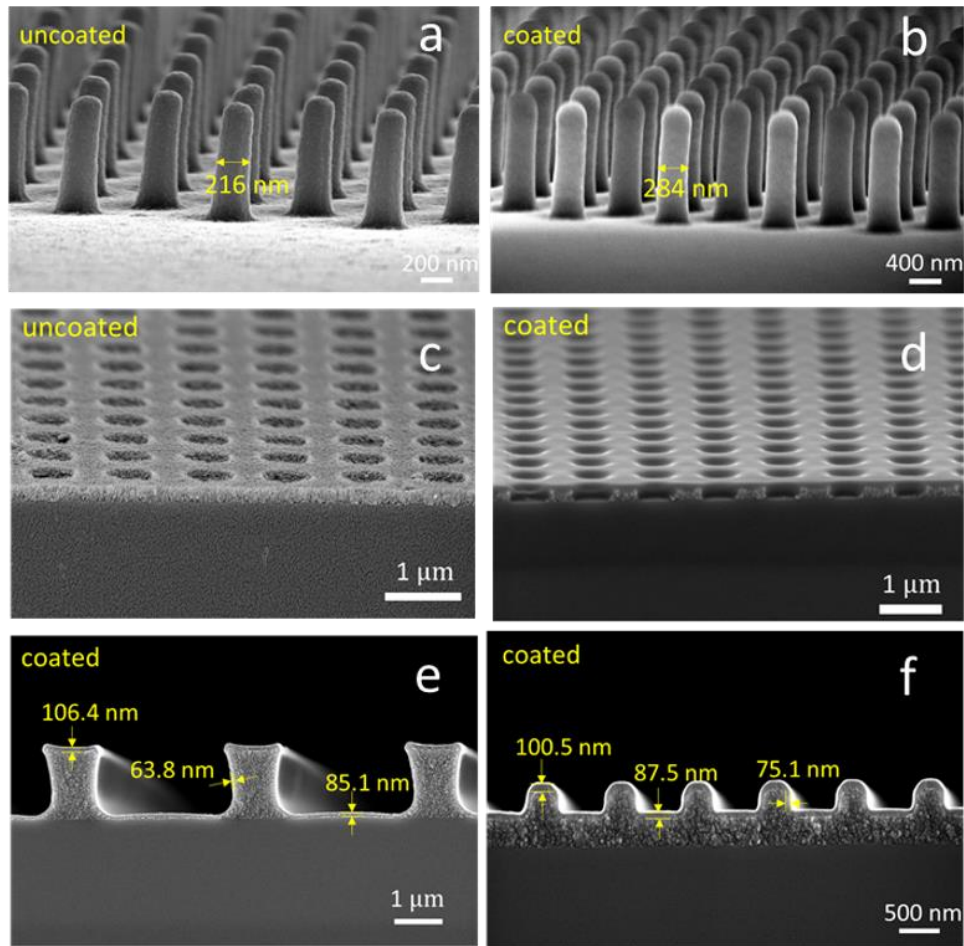
Figure 4.3 SEM images of TiO_2 nanopillars (a) before and (b) after CSE95 deposition, TiO_2 nanopores (c) before and (d) after CSE10 deposition and CSE10 coated (e) microline and (f) nanoline arrays.

Without lithium salt doping, all of the pristine copolymer films showed typical dielectric behavior as indicated by a vertical line in the Nyquist plot (Figure 4.5a). A phase

angle of 89° persisted over a wide frequency range between 1×10^5 to 1×10^2 Hz as shown in the Bode plot (Figure 4.5a, inset). This indicates that there are no mobile charges within the films before ion doping. The electronic conductivity (σ_e) of CP00 and CP95 were measured by applying a small voltage bias between -100 mV to +100 mV. In both cases, reversible and ohmic responses were observed. The σ_e (CP00) and σ_e (CP95) were calculated to be 7.8×10^{-13} S cm^{-1} and 8.9×10^{-11} Scm$^{-1.}$
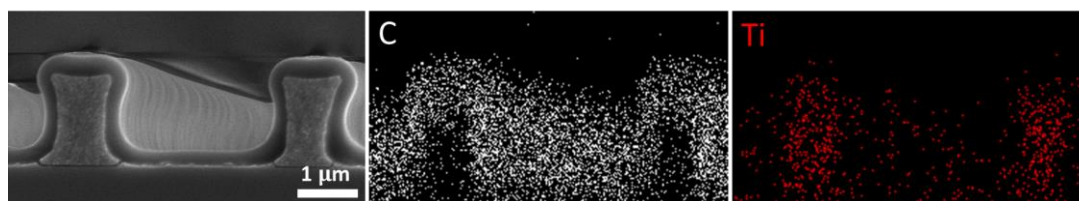
Figure 4.4 EDX mapping of carbon and titanium of a 400 nm CP95 coated TiO$_2$ micro-line array, confirming the conformal coating of copolymer on 3D surfaces.

Such small values indicate the electrically insulating feature of our deposited films at all compositions, which is a prerequisite for nanoscale electrolytes to prevent shorts. We noticed that CP95 possesses a larger σ_e than homopolymer poly(EGDA) (CP00), which may be due to the presence of polarizable -OH groups in HEMA. In addition to high electronic resistance, the thin copolymer films must be able to withstand the significant electrical field between the electrodes to prevent electrical breakdown.[172] The dielectric strength of poly(EGDA) is measured to be 3.9×10^5 V cm^{-1} (Figure 4.6a), indicating that a minimum film thickness of 102.6 nm is needed to prevent electrical breakdown in a 4 V-operated battery. In the following ionic conductivity measurements, deposited copolymer films of all compositions are approximately 300 nm, which far exceeds the threshold thickness.
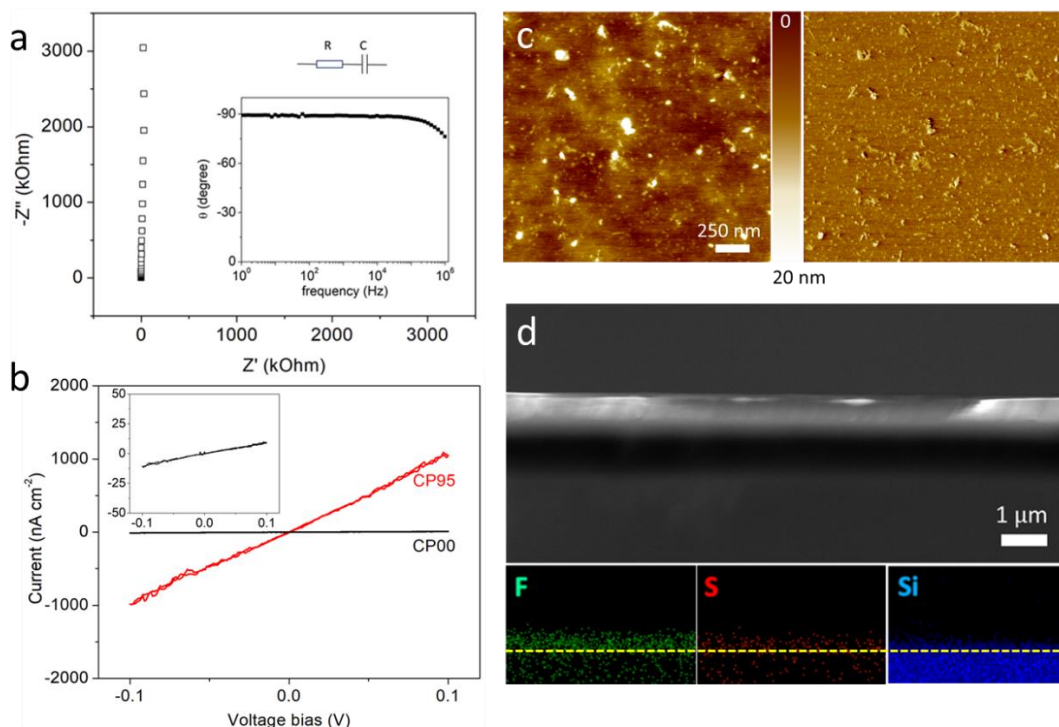
Figure 4.5 (a) Impedance spectroscopy of the CP95 copolymer. Bode plot and the model circuit are shown in the inset. (b) dc current-voltage curves of CP00 and CP95. Data were taken at 2 mV s^{-1}. (c) AFM height (left) and phase (right) images of a CSE95 film on silicon wafer prepared using 0.3 M LiTFSI solution. (d) Cross-sectional SEM and EDX elemental mapping of a CSE95 film.

Lithium ions are introduced into the film by overnight soaking in LiTFSI solution. Here, we denote the lithiated copolymer solid-state electrolytes as CSE10 to CSE95. A layer of salt remains on the surface of the films after doping in 1 M LiTFSI solution if not subsequently rinsed.[164] As the poly(HEMA-*co*-EGDA) network swells easily in polar solvents, excessive rinsing may cause extraction of lithium salt from the film and increase sample variation; therefore, we decreased the concentration of doping solution from 1 to 0.3 M in order to obtain solid electrolyte films without rinsing (Figure 4.5c). After doping, the CSE95 film thickness increased by 40.2% relative to the original CP95 film, consistent with the incorporation of lithium salt into the film. To better visualize the salt distribution throughout the film thickness, we converted an extra thick (650 nm) CP95 film into CSE95,

which exhibited a similar 44.5% thickness expansion, approaching 1 μm. Cross-sectional EDX clearly shows that fluorine and sulfur, characteristic of the TFSI anions, are distributed uniformly throughout the film (Figure 4.5d). While densely cross-linked polymers have previously shown that salt primarily resides in the top layer of depositions,[152] we have achieved a more uniform salt distribution in lithiated poly(HEMA-*co*-EGDA) films. FT-IR analysis confirms the removal of solvent from thin films (Figure 4.6b and 4.6c).
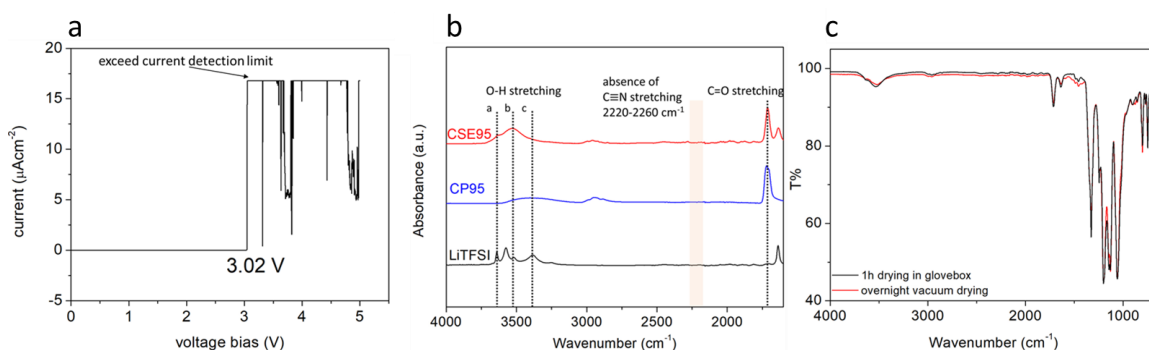
Figure 4.6 (a) Breakdown voltage measurement of a poly(EGDA) film. (b) The absence of absorption peaks between 2220 cm-1 to 2260 cm-1, corresponding to C≡N stretching, confirms that solvent residue concentration is below the FTIR detection limit. (c) Additional drying does not change the IR profile.

The impedance behaviors of the CSE series were characterized by electrochemical impedance spectroscopy (EIS), and the results are shown in Figure 4.7a. For sample CSE10, with the lowest HEMA concentration and the highest cross-linking density, both the Nyquist and Bode profiles are identical to its pristine counterpart, representing negligible conductivity. The poor performance is likely a result of not incorporating enough salt into this densely cross-linked system, as evidenced by a much smaller thickness change of 2.9% after doping. With increasing concentration of HEMA, the impedance profiles clearly show conducting behavior in CSE55 and CSE95. In both cases, a suppressed semicircle at high frequencies is observed, followed by a sharp increase in the imaginary part of impedance

at lower frequencies, coupled with double-layer formation on the ITO and gold blocking electrodes. An equivalent circuit model was fit to the data (Figure 4.7a inset). The circuit contains three sets of RC parallel circuits in series to account for the flattened semicircular shape at high frequencies and a constant phase element to model the Warburg-like blocking behavior at lower frequencies. The additional RC components takes into consideration of any resistive layer at the ITO|CSE and CSE|Au interfaces induced by surface heterogeneities or metal evaporation.[173] The ionic resistance (R_i) is the sum of the fitted values for R_2, R_3, and R_4 and the ionic conductivity is calculated on the basis of Equation 4.2:

$$\sigma = \frac{L}{R_i \cdot A} \tag{4.2}$$

where L is the film thickness after doping and A is the tested film area (6 mm^2). Increasing the HEMA content from 55% to 95% resulted in a shrinkage of the high-frequency semicircle that is consistent with the Bode plot where the peak frequency (f) shifts from 2.53×10^3 Hz to 3.16×10^4 Hz. This indicates a decrease in the conductivity relaxation time (τ_σ), defined as 1/f. The ionic conductivity at room temperature for CSE55 and CSE95 is $(3.2 \pm 0.9) \times 10^{-8}$ S cm^{-1} and $(6.1 \pm 2.7) \times 10^{-6}$ S cm^{-1}, respectively. Impedance profiles of individual samples are provided in Figure 4.8 and fitting results are summarized in Table 4.2 and Table 4.3. The ionic conductivities are more than 4 orders of magnitude larger than their respective electronic conductivities, confirming that conduction is primarily due to the doped ions. Although our CSEs still possess lower ionic conductivities compared to the best performing macroscopic SPEs, the capability of conformal deposition at the nanoscale makes them promising for miniature power source fabrication.
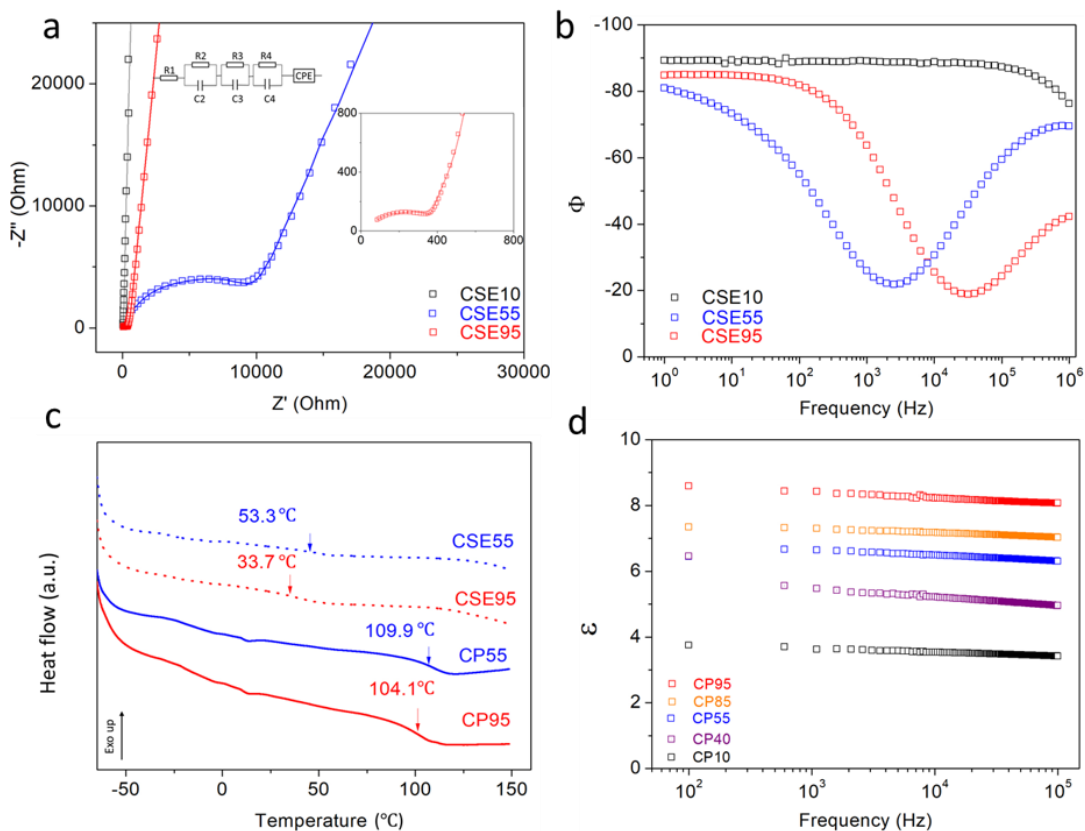
Figure 4.7 (a) Impedance spectroscopy of the doped CSE10, CSE55 and CSE95 films using ITO and gold as blocking electrodes. Magnified view of CSE95 Nyquist plot and the equivalent circuit model are shown in the inset. (b) Bode plots of CSE10, CSE55 and CSE95. (c) DSC traces (heating scan at 10 ℃ min^{-1}) of CP55, CP95 polymer networks and CSE55, CSE95 electrolytes. (d) Dielectric constants measurement of the copolymer series between 1×10^2 to 1×10^5 Hz at room temperature.

To better understand the ionic conduction in the CSEs, we measured the glass transition temperature (T_g) of the CP55 and CP95 matrices as well as their respective doped counterparts (Figure 4.7c) to confirm if the polymer structural relaxation is involved in ionic conduction. The T_g of CP95 network (104.1 ℃) falls into the general T_g range for poly(HEMA) between 40 and 110 ℃. Because of the topological constraints of cross-links, the T_g of CP55 (109.9 ℃) is higher than CP95. Interestingly, salt doping lowers T_g in both systems, as opposed to conventional polyether-based electrolytes, where T_g increases because of the formation of ionic cross-links from polymer-salt coordination. The observed

72

behavior of the poly(HEMA-*co*-EGDA) CSEs is consistent with "polymer-in-salt" systems,[174] in which high salt loading screens strong dipole-dipole interactions in polar polymer matrices with Li^+ coordinated interactions, resulting in an increase of free volume in the system. The T_g values of CSE55 (53.3 °C) and CSE95 (33.7 °C) are still above room temperature, indicating that both samples are at a glassy state when ionic conductivities are measured. As the segmental motion of polymer chains is not significant in this condition, we surmise that the conducting mechanism is dominated by ion hopping through the percolated ionic clusters as in "polymer-in-salt" electrolytes. Additional TGA analysis (Figure 4.9) confirms that salt loading in doped copolymers exceeds 60 wt%, which is much higher than conventional PEO-based SPEs. As the ionic conduction relies on ionic aggregates rather than long range segmental motion of polymer chains, these electrolytes, or else denoted as conducting polymer glasses,[175] display ionic conduction at temperatures near and even below their respective T_g values due to the decoupling of ion transport and matrix structural relaxation. Here we calculated the approximated decoupling index (R_τ), defined as the ratio of structural relaxation time τ_s to τ_σ, using Equation 4.3:[176]

$$logR_\tau \approx 14.3 + log\sigma(T_g) \tag{4.3}$$

For CSE55 and CSE95, log R_τ are 6.8 and 9.1 using room-temperature conductivities; the values will increase if ionic conductivities at T_g are applied. The high R_τ value indicates that the conductivity is highly decoupled from the segmental motion of polymer chains. This estimation compares well with previously reported strongly-coupled systems, such as PEO/LiTFSI (log R_τ =0.3) and strongly-decoupled system as in PMMA/EMITFSI (log R_τ =7.3).[177] In fact, MacFarlane *et. al.* observed a similar decoupling behavior in bulk poly(HEMA)/LiCF$_3$SO$_3$ solid electrolyte, as confirmed by

strong ionic conduction at sub-T_g temperature and the Arrhenius-like correlation of ionic

conductivity to temperature.[175]
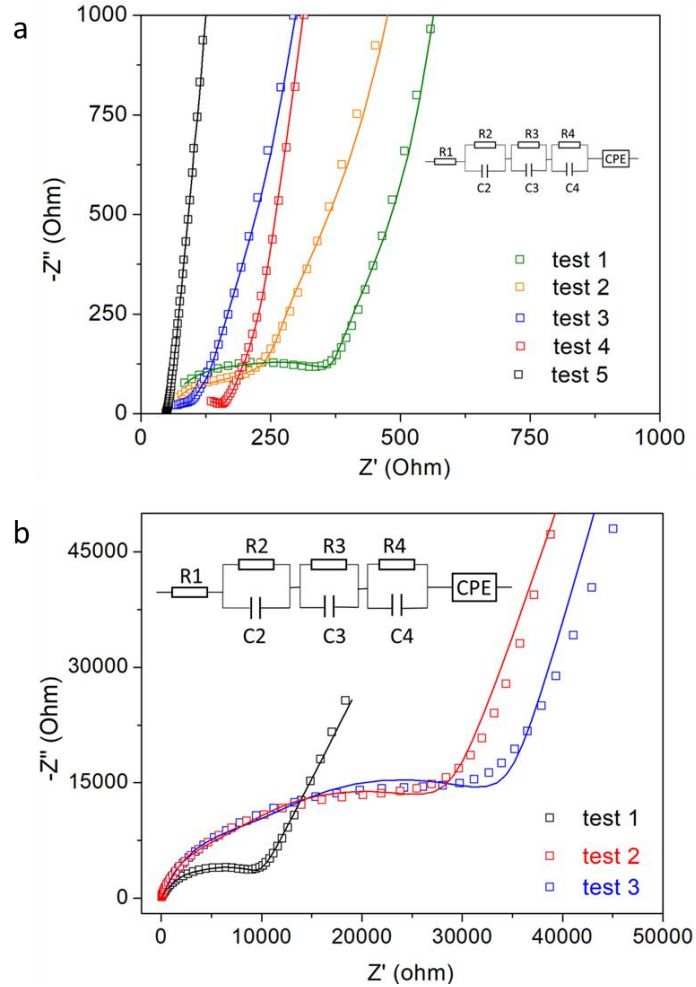
Figure 4.8 Nyquist plots of individual tests for different samples of (a) CSE95 and (b) CSE55. Sample variation may be induced during the solution doping process. All impedance profiles can be fitted into the same equivalent circuit model as shown in the inset. We found it necessary to modify the EC with additional components in order to get good fits. In thin film systems, impacts from interfaces become much more important. We hypothesize that the complication is very likely due to the presence of additional resistive layers at the ITO|CSE and CSE|Au interfaces. This could be induced by salt precipitation upon solvent evaporation (interface heterogeneities). Gold evaporation to polymer surfaces may also cause surface property change.

Table 4.1 Fitting results of impedance values for CSE95.

sample	$R_1(\Omega)$	$R_2(\Omega)$	$R_3(\Omega)$	$R_4(\Omega)$	$R_i=R_1+R_2+R_3$
1	55.35	123.7	158.8	152.0	434.50
2	60.54	91.36	151.8	88.10	331.26
3	102.8	53.60	18.08	38.76	110.44
4	59.92	32.36	77.85	37.29	147.70
5	49.87	11.35	3.032	4.425	18.807

Table 4.2 Fitting results of impedance values for CSE55.

sample	$R_1(\Omega)$	$R_2(\Omega)$	$R_3(\Omega)$	$R_4(\Omega)$	$R_i=R_1+R_2+R_3$
1	87.24	672.3	3745	4558	8975.1
2	43.75	453.4	6548	19550	26551.4
3	69.29	734.6	9482	22440	32656.6

It is interesting to note that CSE95 has a much higher conductivity relative to CSE55, although both systems have a comparable thickness change after salt doping. This indicates that the lithium salt uptake is not the only parameter that impacts ionic conductivity in our CSEs. Similar behaviors were observed in poly(phenylene oxide),[164] where moderate conductivity on the order of 10^{-10} S cm^{-1} was obtained even though the film thickness doubled after doping. As shown in recent studies, the polarity of the polymer matrix contributes to the dissociation of salt, which improves ionic conductivities.[178] For conducting polymer glasses, salt dissociation is crucial to enable the Li$^+$ to screen the interactions between polymer chains. Increasing the HEMA concentration from 10 to 95 mol% increased the dielectric constant from $\varepsilon =3.6$ to $\varepsilon =8.4$ (at 1 kHz) representing an increase in the polarity of the network due to the stronger presence of polar hydroxyl groups. It is important to note that the general range for dielectric constants of polymers are from 2 to 4, *e.g.* ε(PEO)=2.8 at room temperature. The dielectric constant of the CP95 matrix (ε =8.4) is even higher than polar polymer like PAN (ε=4.1) and molten PEO (ε=7.7),[179] which we believe allows the high solubility of salt and facilitates ion dissociation and

transport in the CSEs. This may also contribute to the conductivity difference between CSE55 and CSE95.
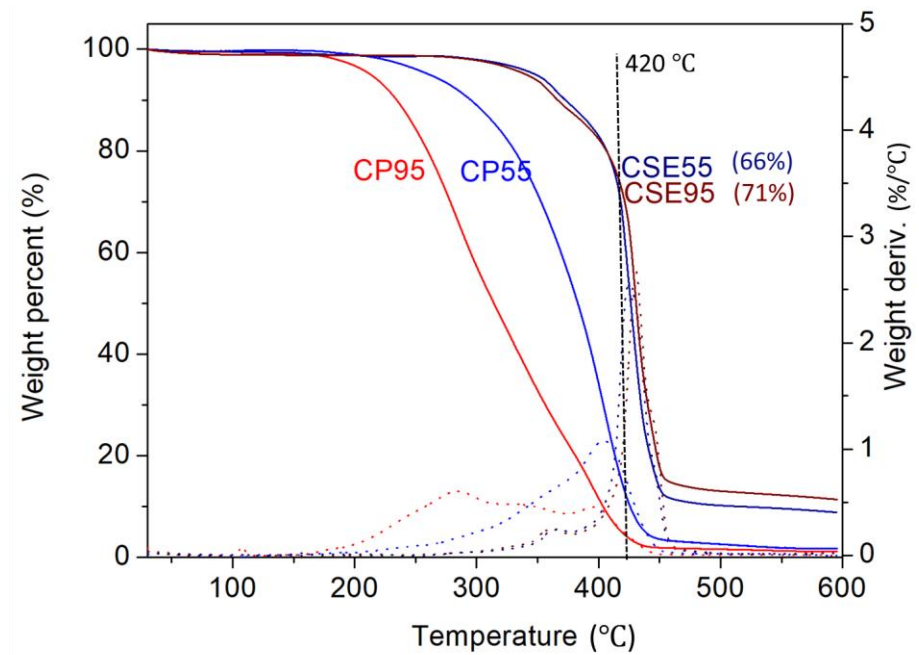
Figure 4.9 TGA analysis of CP55/CSE55 and CP95/CSE55. Since the decomposition temperatures of the copolymer and the salt slightly overlap, we use 420 ℃ as the threshold temperature at which most polymer has decomposed while the salt is still at the beginning of decomposition. With this approximation, salt loading in CSE55 and CSE95 are 66% and 71%, respectively.

4.4 Conclusions and Future Work

In summary, we demonstrated a novel design strategy to fabricate conformal, nanoscale SPEs for 3D battery architectures. By using iCVD as a synthesis platform, we systematically varied the compositions and polarity of the copolymer network to enable high salt loading and fast ionic transport in the electrolytes. These results offer significant advantages for use in 3D miniature power source fabrication. As iCVD is compatible with a variety of vinyl and acrylate monomers, CSEs with enhanced properties, *e.g.* higher breakdown strength and lower electronic conductivity, can be expected. In particular,

fluorinated monomer may generate interesting result due to their unique dielectric properties.

CHAPTER 5

ORDERED NANOPOROUS CARBON ELECTRODES FROM

BOTTLEBRUSH BLOCK COPOLYMER TEMPLATED SYNTHESIS

5.1 Introduction

Ordered porous materials demonstrate great potential for applications including in separation,[180-181] catalysis,[29, 182] energy storage[183-186] and photonics,[187-191]. Preparation of these materials using organic templates, either surfactants or polymers that guide the assembly of precursor films[192] or assembles of crosslinked polymer spheres that serves as mechanical frameworks for precursor infiltration,[193-195] is especially attractive as it avoids the necessity of etching in synthetic routes that employ inorganic templates, such as silica beads.[196] The use of soft templates represents a green and highly tunable "bottom up" method.[197] Access to the full spectrum of pore sizes, from micro- (1-2 nm), meso- (2-50 nm) to macropores (50 nm and above), is of urgent demand to enable the versatility of ordered porous materials. Soft templating via the assembly of small molecule surfactants and linear block copolymers (BCPs) has been successfully employed to prepare mesoporous carbons with pore sixes between approximately 2 nm and 35 nm.[41, 193, 198-199] Access to larger pore sizes by using linear block copolymers is typically limited by kinetic challenges to forming ordered precursor films with high molecular weight templates, which can be partially mitigated by the addition of pore swelling agents. On the other hand, very large pores can be accessed by infiltrating assemblies of polystyrene (PS) beads with carbon precursors followed by removal of the beads during carbonization. This physical templating approach leads to porous carbons with pore sizes of hundreds-of-nanometers. [195, 200-202] While both techniques are useful and widely applied, there remains an apparent

and wide gap in accessible pore sizes in a critical regime between about 35 and 150 nanometers. In this work, we demonstrate that a series of amphiphilic bottlebrush block copolymers with precisely controlled molecular weights used as soft templates can generate porous carbons with spherical domain sizes ranging from 18 nm to 150 nm, effectively bridging meso- and macropores using a single class of template (see Figure 5.1a and 5.1b)

Bottlebrush block copolymers (BBCPs) are comb-like macromolecules with densely grafted side chains of distinct chemical functionalities.[49-51, 203-204] One major advantage of BBCPs are their significantly reduced chain entanglements by comparison with the linear analogs, leading to lower energy barriers for structural reorganization and rapid assembly, as shown by Grubbs[205] and others[56, 206]. Previously, the lamellae morphologies have been extensively studied, with respect to the bottlebrush molecular structures, lamellae dimensions and assembly kinetics.[30, 51, 203, 205, 207-208] These results offered significant advantages for the rapid fabrication of photonic crystals, by using BBCPs directly or using BBCPs as soft templates to accurately align functional nanoparticles into layered hybrid nanostructures;[30, 207, 209] BBCPs composites with ZrO$_2$,[206] Au[56] and CdSe[55] nanoparticles have been successfully demonstrated to obtain Bragg mirrors and nonlinear photonic devices. Further exploration of diverse morphologies of BBCPs, for example, cylindrical and spherical morphologies, would be highly beneficial toward the rapid fabrication of nanoporous materials. By introducing strong asymmetry into polystyrene-*block*-polylactide (PS-*b*-PLA) BBCPs side chains and inducing interfacial curvature, Rzayev and coworkers achieved cylindrical morphologies;[210] additional removal of PLA phase resulted in nanoporous PS monoliths. However, reports on

79

systematic research for realization of spherical morphologies of BBCPs are still rare. The extended poly(norbornene) backbone and the densely grafted, stiff side chains present energy barriers to the formation of high-curvature spherical morphologies. Although BBCP spherical micelles in dilute aqueous environment have been achieved,[211] the rapid formation of such morphologies in the bulk is of demand for one-step templated synthesis of functional materials.

We have recently shown that BBCPs with soft poly(dimethylsiloxane) (PDMS) side chains possess additional flexibility relative to their counterparts with stiff side chains.[204] This reduces energy penalties to the formation of high-curvature morphologies. By incorporating a hydrophilic poly(ethylene oxide) (PEO) block that exhibits selective interaction to hydrogen bond donors, we report here the additive-driven assembly of BBCPs composites with well-ordered spherical morphologies. Specifically, blends comprised of PDMS-*b*-PEO BBCP templates and phenol-formaldehyde resin (resol) were prepared. We then converted the precursor blend into nanoporous carbon with interconnected hierarchical pores by carbonization and pyrolysis (Figure 5.1a). The nanoporous carbon films are shown to possess superior charge storage capability for supercapacitor applications, as a combined result of high surface area and ordered, connected pathways for rapid electrolyte diffusion.

One step further, we harness the facile fabrication strategy and add a third component to the hybrid precursor to enhance the charge storage capacity of the porous electrodes. Here we chose Fe_2O_3 nanoparticle, an anode material in lithium-ion batteries known for high specific capacity above 900 mAhg^{-1}.[212] It is worth mentioning that Fe_2O_3 is photothermally active, which enables rapid carbonization via intense flash lamp

radiation, instead of prolonged tube furnace pyrolysis. This offers significant advantages to large-scale, low-cost fabrication of composite electrodes.

5.2 Experimental Section

5.2.1 Materials

Hydroxyl-terminated polydimethylsiloxane (PDMS-OH, M_w = 4.7 kg mol^{-1}), and poly(ethylene glycol) methyl ether (PEO-OH, M_w = 5.0 kg mol^{-1}) were purchased from Sigma-Aldrich. They were heated at 120 °C for 4 h under nitrogen flow to remove moisture before usage. Grubbs 3rd generation catalyst, exo-5-norbornenecarboxylic acid, N,N'-dicyclohexylcarbodiimide (DCC, >99.0%), and 4-dimethylaminopyridine (DMAP, >99%) were purchased from Sigma-Aldrich, and used without further purification. Anhydrous dichloromethane (DCM), and anhydrous tetrahydrofuran (THF, 99.9%) were purchased from Acros Organics. The phenolic resin was synthesized in the lab following previous literature.[193]
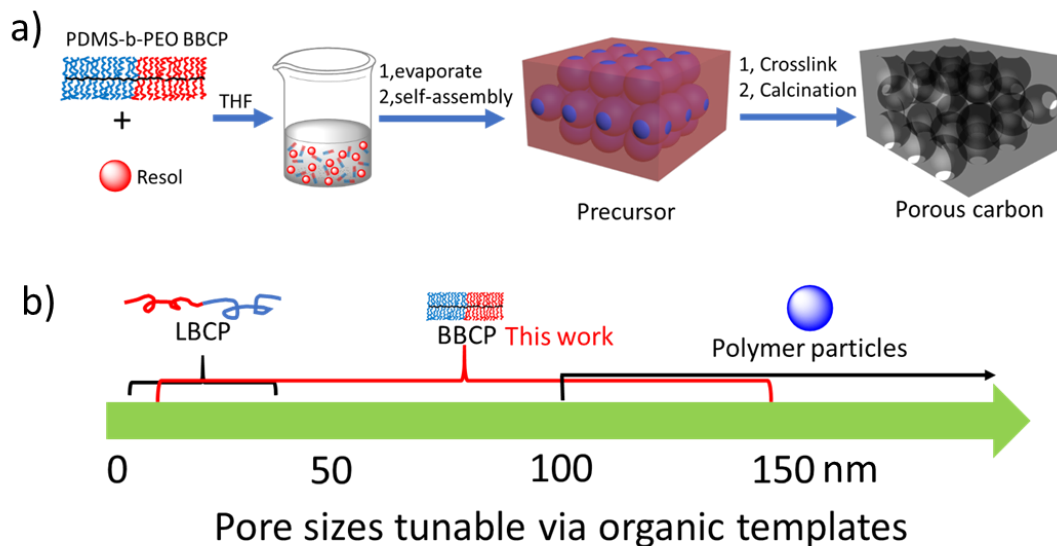
Figure 5.1 (a) Schematic illustration of additive-driven BBCP assembly and subsequent pyrolysis leading to nanoporous carbon. (b) Pore sizes tunable breadth with different organic templates.

5.2.2 Synthesis of PDMS-b-PEO brush block copolymers (BBCPs)

The macromonomers PDMS capped with norbornene (PDMS-NB, M_w = 4.8 kg mol^{-1}) and PEO-NB (M_w = 5.0 kg mol^{-1}) were synthesized according to the reported method.[203, 213] The PDMS-*b*-PEO BBCPs were synthesized through sequential ring opening metathesis polymerization (ROMP). In a typical synthesis, 200 mg of each macromonomer was added to separate reaction flasks in a N$_2$ filled glove box, followed by the desired amount of anhydrous DCM. The concentration of the macromonomer was varied between 0.05 M and 0.1 M. At room temperature, the polymerization of PEO-NB was initiated by adding desired amount of 3rd generation Grubbs catalyst solution in DCM. After the first macromonomer (PEO-NB) polymerized (approximately 15 min), the solution of the second macromonomer (PDMS-NB) was added to the reaction mixture. The obtained solution was stirred for an additional 2-3 hours to ensure complete polymerization and then the reaction was terminated with ethyl vinyl ether. The obtained PDMS-*b*-PEO

BBCP was characterized by ^{1}H NMR spectrum. The molecular weight of PDMS-*b*-PEO BBCP was controlled by tuning the molar ratio of macromonomers to catalyst. GPC MALLS trace of all the prepared samples displayed monomodal peak with narrow molecular weight distribution. The obtained BBCPs with different M_w are denoted as BBCP-210k, BBCP-250k, BBCP-394k, BBCP-640k and BBCP-1800k.

5.2.3 Preparation of precursor and porous carbon

The PDMS-*b*-PEO BBCPs and resol were dissolved separately into THF with a concentration of 20 mg mL^{-1}. 1.0 mL PDMS-*b*-PEO solution was mixed with 1.5 mL phenolic resin solution; excess solvent was evaporated by blowing nitrogen until the concentration reached approximately 100 mg mL^{-1} was obtained. Then 50 µL mixture solution was drop casted on silicon wafers or stainless steel sheets. After solvent evaporation at room temperature, the precursor was subsequently crosslinked by heating up in an oven at 150 ℃ for 2 hours. To prepare the nanoporous carbon, the crosslinked precursor was further pyrolyzed in a tube furnace at 700 ºC for 30 min under a nitrogen flow (120 mL min^{-1}) with a heating rate of 10 ℃ min^{-1}. The average thickness of nanoporous film is ~15 µm, and the mass loading is ~1.0 mg cm^{-2}.

Following a similar procedure, the precursor films containing iron/iron oxide nanoparticles can be prepared using a mixture of PS-b-PEO brush BCP (50 mg), iron oxide NPs (100 mg) and phenol resol (80 mg) in dimethylformamide (1.4 mL). PS-b-PEO was synthesized based on the group's previous report.[56] A rod with a gap size of 35 micrometers was used for the preparation of the coating films, resulting in dried films on nickel foils with average thicknesses of approximately 2.0 µm. The iron/iron oxide NPs

were synthesized according to our reported procedure, and ligand exchange was carried out to graft 4-hydroxybenzoic acid onto the NP surface.[214]

The photothermal processing was carried out on a Novacentrix Pulseforge 1300 photonic curing system. The light intensity was tunable via changing applied voltage and/or pulse duration time. For the preparation of carbon/iron oxide membranes on aluminumthe pulse duration time was fixed at 0.6 milliseconds and the voltage at 610 V was applied affording an optimal light energy at 6572 mJ/cm^2. Different light exposures (4, 8, and 12) were performed with a time interval of one second.

5.2.4 Characterization and measurements

Gel permeation chromatography (GPC) of the BBCPs was carried out in THF with 1.0 vol% triethylamine (TEA) on two PLgel 10 µm mixed-B LS columns (Polymer Laboratories) connected in series with a Wyatt Technologies DAWN EOS multi-angle laser light scattering (MALLS) detector and RI detector at a flow rate of 1.0 mL min^{-1}. No calibration standards were used for the BBCPs as direct dn/dc values were obtained for each injection by assuming 100% mass elution from the columns. Fourier-transform infrared spectroscopy (FTIR) measurements were carried out on a PerkinElmer FTIR spectrometer equipped with a universal ATR sampling accessory. Small-angle X-ray scattering (SAXS) measurements were performed on a Ganesha SAXS-LAB using 0.154 nm (Cu-Kα radiation), and X-ray beam area of approximately 0.04 mm^2 and a Linkam HFS600E-P temperature stage. Transmission electron microscopy (TEM) measurements were conducted with a JEOL 2000FX TEM operated at an accelerating voltage of 200 kV. Thin sections of approximately 30 nm in thickness were prepared using a Leica Ultracut UCT microtome equipped with a Leica EM FCS cryogenic sample S2 chamber operated

at T = −160 °C. Tomography was carried out using a JEOL JEM-2200FS at 200 kV acceleration voltage and a probe size of 1.5 nm. Scanning transmission electron microscopy in high angle annular dark field imaging mode (STEM-HAADF) was used. Image series of 121 images for tomography reconstruction were recorded at 1° steps from −60° to + 60° tilt angles. Three-dimensional reconstructions were generated using the filtered back projection algorithm in Etomo (part of the IMOD software package, UC Boulder). Volume and iso surface rendering were performed using Chimera (UCSF) software. Field emission scanning electron microscopy (FESEM) measurements were carried out on a FEI Magellan 400 FESEM. Raman spectrum were collected on Reinshaw RAMAN spectrometer with 632.8 nm excitation wavelength. Nitrogen adsorption/desorption measurements were conducted on an Autosorb-1 system at liquid nitrogen temperature (77K). The specific surface area was calculated by using the Brunauer-Emmett-Teller (BET) method. Electrochemical measurements, includeing cyclic voltammetry (CV), galvanostatic charge−discharge (GCD) and cycling test were carried out in a three-electrode cell with a Pt wire counter electrode and Ag/AgCl reference electrode with a CHI660E electrochemical workstation (CH Instruments Inc.). Electrochemical tests were conducted in 6 M KOH at ambient temperature with aqueous potentials referenced against Ag/AgCl. The CV curves were obtained at various scan rates from 10 to 1000 mV s^{-1} in the range of −1.0 to −0.2 V. GCD curves were obtained at various current densities from 2 to 100 A g^{-1} in the range of −1.0 to − 0.2 V. All LIB tests were performed on Maccor 4304 electrochemical station, in the half-cell configuration, where a piece of lithium metal served as both the counter and reference electrode. 1M LiClO$_4$ dissolved in a 1:1 ratio of ethylene carbonate and dimethyl carbonate by volume served as

the electrolyte. The galvanostatic cycling was performed within a voltage window of 0.01V-3.0V. Specific capacity calculation was based on the total mass of the hybrid material measured by the microbalance (Cahn C-31). All tests were conducted in an argon atmosphere.

5.3 Results and Discussion

In this study, we synthesized PDMS-*b*-PEO BBCPs with constant PDMS and PEO side chain lengths (PDMS 4.8 kg mol^{-1}, PEO 5.0 kg mol^{-1}) and mass fraction f(PDMS) = 50%, but varied backbone repeating units, as shown in Figure 5.2. We denote the polymers as BBCP-M_w, where M_w is the total molecular weight of the macromolecules sampling 210, 250, 394, 640 and 1800 kg mol^{-1}.
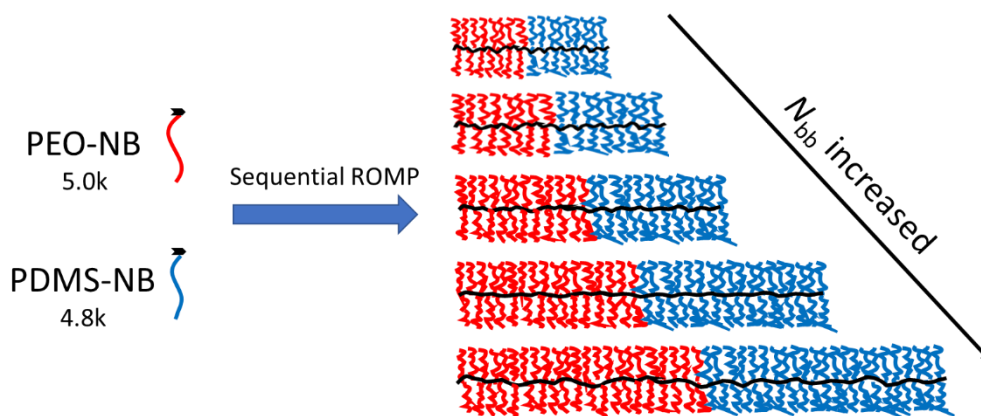
Figure 5.2 Schematic illustration of PDMS-*b*-PEO BBCP synthesized in this work.

To understand the morphology transition of PDMS-*b*-PEO BBCPs, BBCP-210k is discussed here in detail. Small angle X-ray scattering (SAXS) profile of neat BBCP-210k (Figure 5.3a) after annealing at 80°C for 6 hours shows little evidence of microphase separation. It indicates that PDMS and PEO exhibit a low χ that is insufficient to drive

86

phase separation at room temperature. However, strong indication of microphase separation appeared with the addition of small amount (5-25 wt%) of additives that can hydrogen bond to the PEO block. The concept of additive driven assembly resulting from the addition of components that can hydrogen bond selectively to one block of a BCP was demonstrated using PEO containing polymers with small and large molecular weight additives by Tirumala[215-216] and Daga[217-218]. We utilized 4-hydroxybenzoic acid (HBA), an extensively studied hydrogen bond donor for additive-driven assembly. It can be surmised that the selective hydrogen bonding of HBA to PEO side chains leads to an increase of χ between PDMS and PEO/HBA hybrid, enabling the formation of well-ordered morphologies.[219] The q* position ratio of 1:3:5 indicates that PDMS-*b*-PEO BBCP mixture with 5 wt% HBA exhibits symmetric lamellae morphology with d spacing ($2\pi/q*$) of 36.3 nm. This value increased to 39.2 nm as the amount of HBA increased to 15 wt%, which is likely due to the increasing volume fraction of PEO/HBA domain. When the additive amount exceeded 25 wt%, we observed an interesting order-to-order transition from lamellae to body center cubic (BCC) packing spherical morphology, as evidenced by the q* position ratio of 1:$\sqrt{3}$.[220] The formation of uniform spherical morphology was further confirmed by transmission electron microscopy (TEM) (Figure 5.3b), where the light and dark domains correspond to PEO/HBA and PDMS respectively due to the difference of C and Si nuclear masses. The phase transition from lamellae to spheres could be ascribed to the additive induced volume fraction asymmetry in PDMS and PEO/HBA. The result is promising in that PDMS-*b*-PEO BBCPs can be used as soft templates for hydrophilic precursors that demonstrate strong hydrogen bonding with PEO side chains to form porous functional materials.
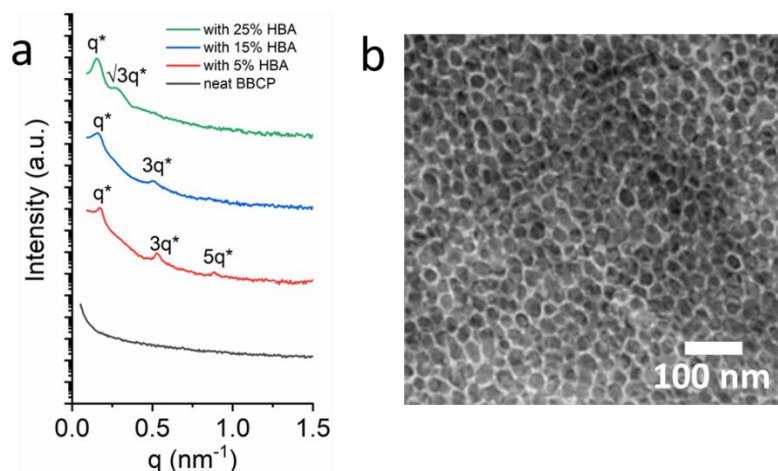
Figure 5.3 (a) SAXS profiles of BBCP-210 K mixture with different amount of small molecule 4-hydroxybenzoic acid (HBA). (b) Bright field TEM image of BBCP-210 K with 25 wt% HBA.

To extend the strategy to other additives, phenol-formaldehyde resin, or "resol"(thermally curable prepolymer with M_w ~ 500 g mol^{-1}) was selected as a hydrogen bond donor and a carbon precursor.[193] As expected, strong microphase separation appeared after blending in resol (Figure 3a). In all hybrid samples, resol to BBCP weight ratio maintained at 1.5:1 to ensure spherical morphology formation. In fact, lamellae morphologies appear when the ratio was between 0.25:1 and 0.5:1 (Figure 5.5). After thermal curing, the morphologies of the organic hybrids were imaged by TEM and are shown in Figure 5.4b to 5.4f. Uniform, well-ordered spherical morphologies are evident in all samples templated by BBCPs with increasing M_w. The diameter of PDMS spheres significantly increase from 18 nm to 150 nm as the M_w of BBCP increases from 210k to 1800k (Table 5.1). SAXS profiles (Figure 5.4a) provide additional evidence to conclude the formation of spherical morphologies, indicated by the scattering peak position ratios of 1: √3: √7. For BBCP-1800k, the scattering peak intensity is weak because q* was too small and the position too close to the beam stop. The d-spacings (2π/q*) increased accordingly as the M_w of BBCPs increased, as listed in Table 5.1.
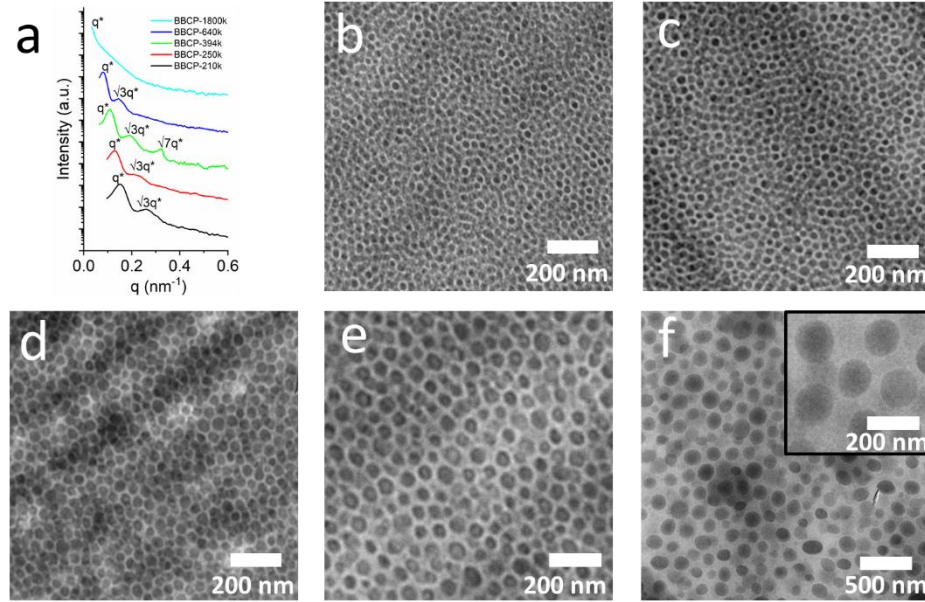
Figure 5.4 (a) SAXS profiles of neat PDMS-*b*-PEO BBCPs and the BBCPs blend with resol. TEM images of organic hybrids 1~5 (b,c,d,e,f) showing well-ordered spherical morphologies.

Table 5.1 PDMS sphere diameters in BBCPs with different molecular weight.

Samples	M_w (kg mol^{-1})	Đ	Sphere diameters (nm)
BBCP-210k	210	1.15	18.6 ± 3.2
BBCP-250k	250	1.16	23.8 ± 3.0
BBCP-394k	394	1.20	34.5 ± 4.1
BBCP-640k	640	1.23	57.3 ± 5.8
BBCP-1800k	1800	1.28	149.7 ± 18.1

A simplified mathematical relationship between PDMS sphere diameter (D) and M_w of BBCPs is present in Equation (5.2), based on an assumption that the PDMS sphere surface area equals to the sum of individual PDMS-*b*-PEO brush interfacial area (A), as illustrated in Figure 5.6a.

$$D = \frac{6f_{PDMS}}{A\rho_{PDMS}N_A} M_w \qquad (5.2)$$

Here f_{PDMS} and N_A are mass fraction of PDMS block and Avogadro constant. From Equation (5.2), D follows a linear relationship with M_w, which is consistent with our

experimental observations (Figure 5.6b). It is worth noting that from the slope in Figure 5.6b, the interfacial area of individual BBCP molecule is calculated to be A = 61.7 nm^2, and a resultant radius of R = 4.4 nm. This value is very comparable to the end-to-end distance of PDMS side chains (R= 4.7 nm) that was calculated from previous literature.[213, 221-222]. The consistency provides confidence for our proposed model of spherical morphology formation.
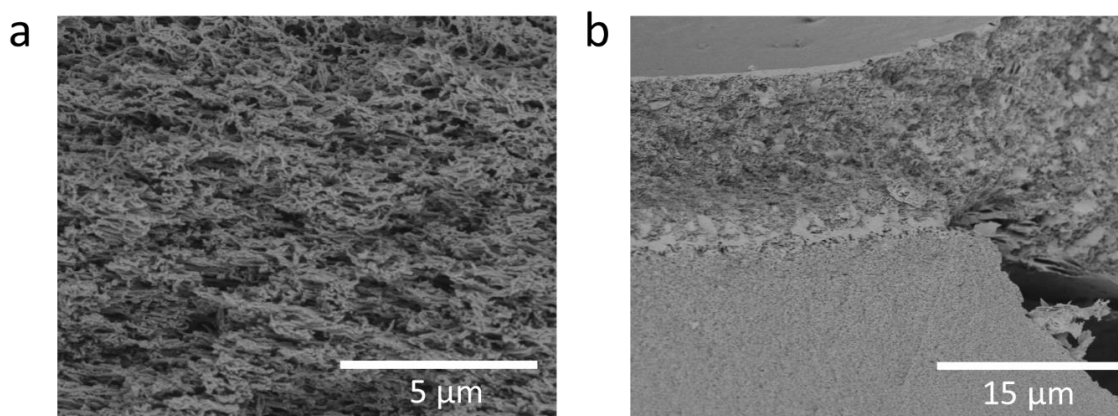
Figure 5.5 Cross-sectional FESEM image of carbon from the precursors with less resol, a) resol : BBCP = 0.25:1 by weight, exhibiting lamellar morphology and b) 0.5:1 exhibits coexistence of lamellar (top) and spherical (bottom) morphologies.

Table 5.2 The dn/dc values of GPC MALLS test and d-spacing ($2\pi/q^*$) from SAXS

Samples	dn/dc	d-spacing (nm)
BBCP-210k	0.034	41
BBCP-250k	0.037	50
BBCP-394k	0.035	60
BBCP-640k	0.036	79
BBCP-1800k	0.035	-

The conversion of as-prepared organic hybrids into nanoporous carbon was conducted by tube furnace pyrolysis in an inert atmosphere (Figure 5.7a). PDMS is reported to go through multistep degradations into a series of volatile, oligomeric cyclic

siloxanes around 420 °C [223-224](Figure 5.7b). As different cyclic siloxanes possess different boiling points, the degradation is relatively mild, preventing the structure from being cracked by rapid gas evolution during template degradation. After carbonization, only 2.7% silicon remained, indicating that the PDMS domain completely decomposed with minimal doping, confirmed by FTIR (Figure 5.8a) and XPS (Figure 5.8a). A representative porous carbon film templated from BBCP-1800k is shown in Figure 5.7c. Uniformly large pores of approximately 100 nm demonstrated hexagonally packing after pyrolysis. Moreover, the high magnification SEM image (Figure 5.7c inset) clearly shows the smaller meso- and micropores on the carbon walls due to template degradation, resulting in a hierarchical porous structure.
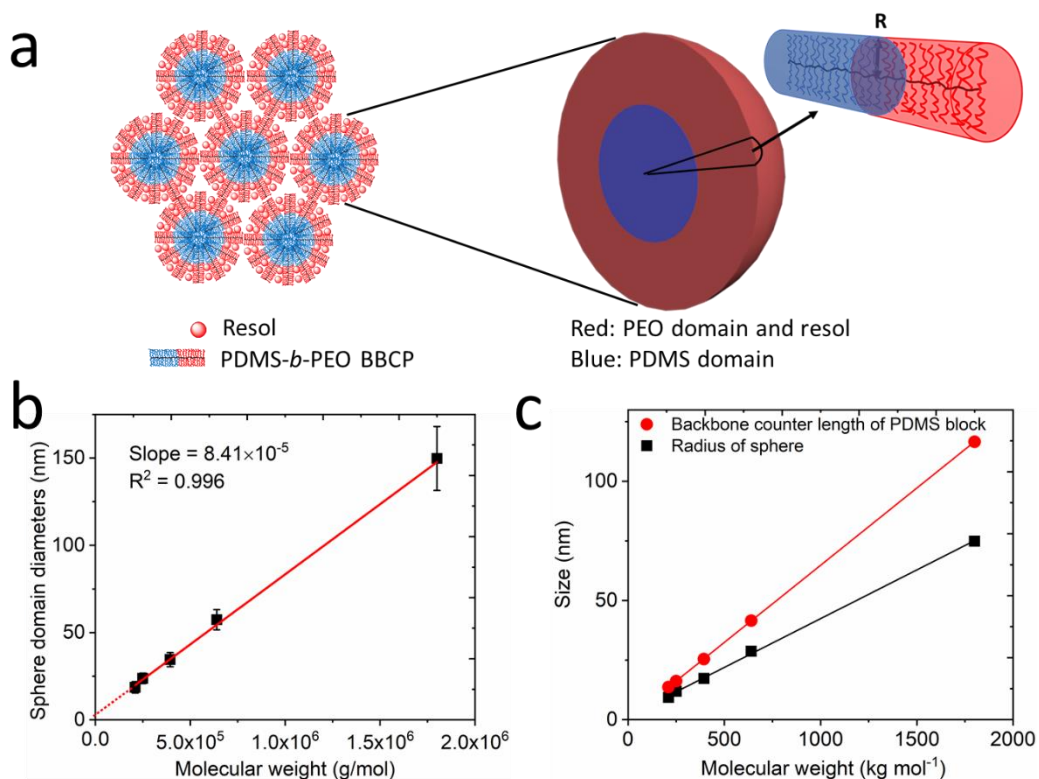
Figure 5.6 (a) The illustration of PDMS-*b*-PEO BBCP self-assembly into spherical morphologies. (b) the linear relationship between the BBCP molecular weight and

spherical diameter. (c) sizes of the calculated counter length (red) and measured radius of spheres.
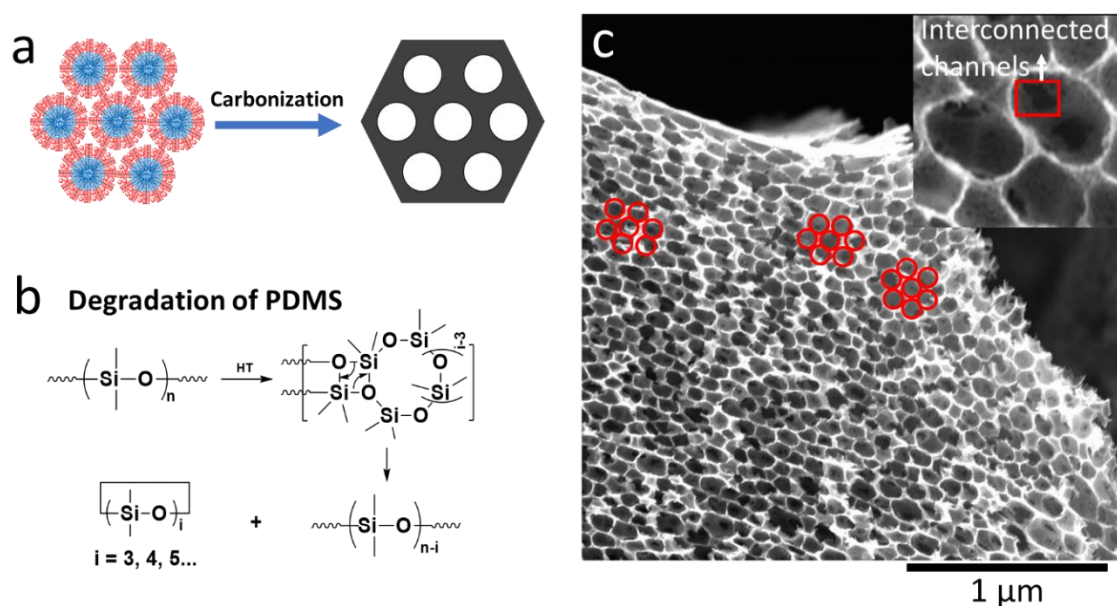
Figure 5.7 (a) Scheme of preparing of well-ordered interconnected porous carbon. (b) the degradation of PDMS at high temperature. (c) FESEM image of typically porous carbon (PC-5) after carbonization, the insert image size is 250×250 nm.

As shown in Figure 5.9a to 5.9e, the pore size gradually increased from 15.7, 22.1, 32.7, 49.0 to 107.7 nm as the M_w of BBCP templates increased from 210 to 1800 kg mol^{-1}. We denote these carbonized samples as PC-1 to PC-5. The broader tunability window of pore sizes from mesopore to macropores by BBCPs is impressive compared to that of using linear block copolymers.[45, 47, 181, 192, 225] It is worth noting that in addition to pore size control, interconnected porous structures are clearly observed by TEM shown in Figure 5.9f to 5.9k.
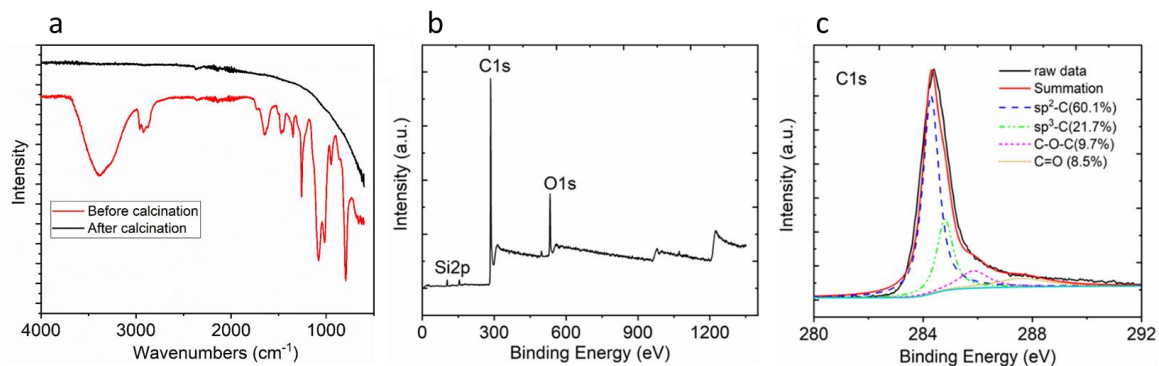
Figure 5.8 (a) FT-IR spectrum of hybrid precursor and nanoporous carbon. (b) XPS analysis of   obtained nanoporous carbon. (c) C1s XPS spectrum. The black line is experimental data that can be deconvoluted into several synthetic peaks (dashed curves). The red solid curve is the summation of all the synthetic peaks. Percentages of different carbon species are evaluated based on area of synthetic peaks.
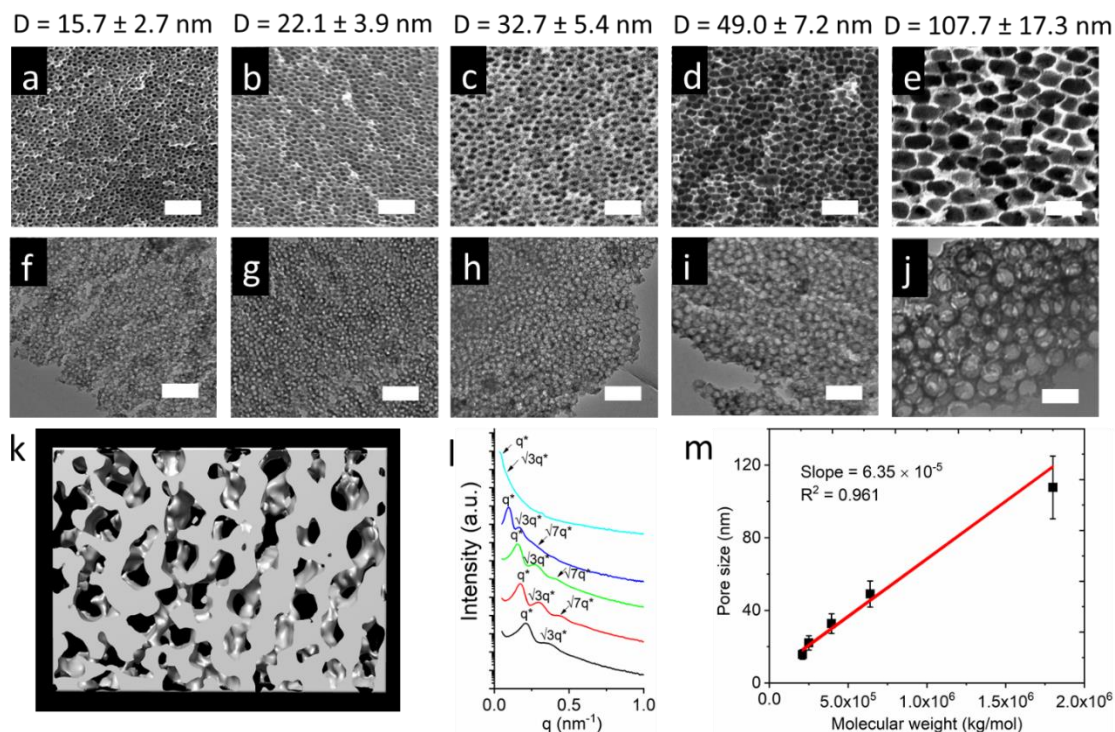
Figure 5.9 The pore sizes are well controlled by molecular weight of BBCPs. (a-e) FESEM images of nanoporous carbon with different pore size. (f-j) Bright filed TEM images of nanoporous carbon with different pore sizes. The scale bar is 200 nm. (k)The tomography of selected nanoporous sample (l) SAXS profiles of all the porous carbon, from bottom to top the pore sizes are increased. (m) the linear relationship between pore size and molecular weight of BBCPs.

SAXS profiles (Figure 5.9l) of PC-1 to PC-4 all maintained strong high order peaks, with peak position ratio q* equals to 1: $\sqrt{3}$ or 1: $\sqrt{3}$: $\sqrt{7}$. The linear relationship ($R^2 = 0.961$) between the pore size and molecular weight of BBCPs (Figure 5.9m) indicates that the ordered spherical morphologies were well maintained after pyrolysis. The slope of 6.35×10^{-5} is slightly smaller than that of the organic hybrid (slope = 8.41×10^{-5}), as a result of the volume shrinkage during pyrolysis.

Several features make the nanoporous carbon promising candidates for supercapacitor applications. Raman spectroscopy (Figure 5.10) shows G band at 1580 cm^{-1} and higher order 2G band at 2700 cm^{-1}, with an intensity ratio $I_{(G)}/I_{(D)}$) of 1.17, indicating a considerable degree of graphitization. The electrical conductivity is approximately 150 S m^{-1}, which is significantly higher than that of commercial activated carbon ($\sim$ 50 S m^{-1}).[183] In addition, the nanoporous carbon surface was found to have oxygen-containing functionalities, as confirmed by the strong oxygen signal in X-ray photoelectron spectroscopy (XPS) (Figure 5.8c). It has been reported that oxygen functionalities can increase the wettability of carbon materials and ease the electrolyte permeation into the porous structure.[226] The interconnected, ordered nanopores provide lower tortuosity for electrolyte diffusion relative to that in randomly distributed pores, as in commercial activated carbon.[186, 197] The nanoporous carbon films on stainless steel were tested as electrodes without any post-modification, *e.g.* KOH activation.[227-228] For demonstration purposes, PC-2 (average pore size 22 nm) and PC-5 (average pore size 107 nm) were selected for further physical and electrochemical characterizations.

Figure 5.11a shows the nitrogen absorption-desorption isotherms of PC-2 and PC-5. The steep increase in the amount of nitrogen absorbed at low relative pressure ($p/p_0 <$

0.1) indicates the existence of micropores and capillary condensation.[229] The hysteresis loop located at $0.4<p/p_0<1.0$ suggests the presence of small mesopores. The formation of micropores and smaller mesopores is likely due to gas evolution during the pyrolysis, consistent with our prior discussion. In fact, these hierarchical pores generated from gas evolution improve the interconnectivity of the structure and increase the total surface area of the nanoporous carbon (Figure 5.11b). PC-2 and PC-5 showed considerably high surface areas of 573 and 508 $m^2\,g^{-1}$ respectively (Table 5.3).

The electrochemical performances of PC-2 and PC-5 films were investigated in a three-electrode electrolytic cell filled with 6 M aqueous KOH electrolyte. The cyclic voltammetry (CV) scans for PC-5 at varied scan rates are shown in Figure 5.11c. Quasi-rectangular shape of the CV curves are well-maintained for scan rates up to 1000 mV/s. Galvanostatic charge/discharge (GCD) profiles in a potential range between −1.0 and −0.2 V under different current densities for PC-5 were shown in Figure 5.11d. The isosceles triangular shaped GCD profiles collected at large current densities indicate that PC-5 has nearly ideal capacitive performance and efficient ion transfer.[183, 186] The specific capacitance (C_g) of PC-5 was found to be 211 $F\,g^{-1}$ at a current density of 2 A g^{-1}. Moreover, the electrode possesses strong capacity retention, remaining 59.2% of the capacitance (125 $F\,g^{-1}$) at a high current density of 100 A g^{-1} (Figure 5.11e). This result compares favorably among electrostatic double layer capacitors (EDLCs).[183, 186] PC-2 exhibits comparable but slightly higher specific capacitance (254 F g^{-1} at a current density of 2 A g^{-1}) than PC-5 (Figure 5.11e).
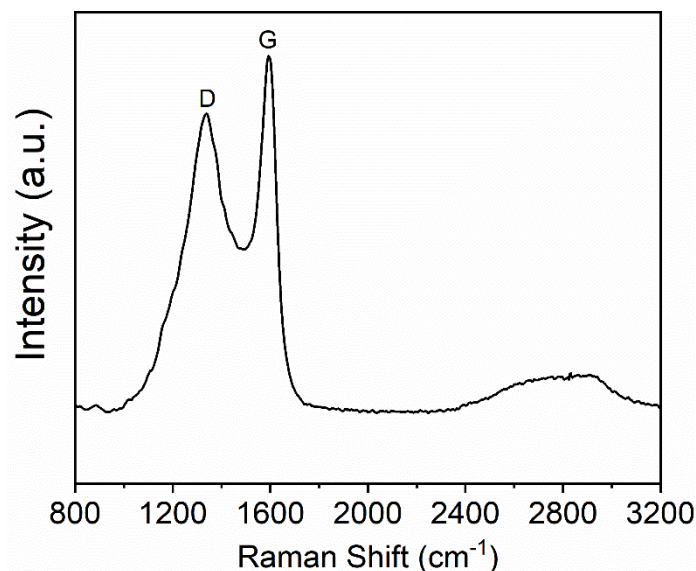
Figure 5.10 Raman spectrum of PC-5 nanoporous carbon.

Electrochemical impedance spectroscopy (EIS) (Figure 5.12a) revealed that PC-5 possessed combined series resistance (R_s) as small as 0.21Ω, and a negligibly small charge transfer resistance ($R_{ct} < 0.5$ Ω). Further analysis of the Bode plot (Figure 5.12b) discloses that the characteristic time constant (τ_0) equals to 0.16 s, which is smaller than most carbon based materials.[183] The small τ_0 of PC-5 is in agreement with the good rate capability. In addition, PC-5 demonstrated stable electrochemical cycling with 97% retention after 10000 cycles (Figure 5.11f). These results confirm that the BBCP templated nanoporous carbon generates exceptional EDLC supercapacitor performance.

Table 5.3 BET results of PC-2 and PC-5

Samples	BET surface area (m²/g)	Micro pore surface area (m²/g)	Total pore volume (cm³/g)[a]	Micro pore volume (cm³/g)[b]
PC-2	573	314	1.001	0.150
PC-5	508	284	0.585	0.136

[a] DFT absorption cumulative volume. [b] t-plot micropore volume.
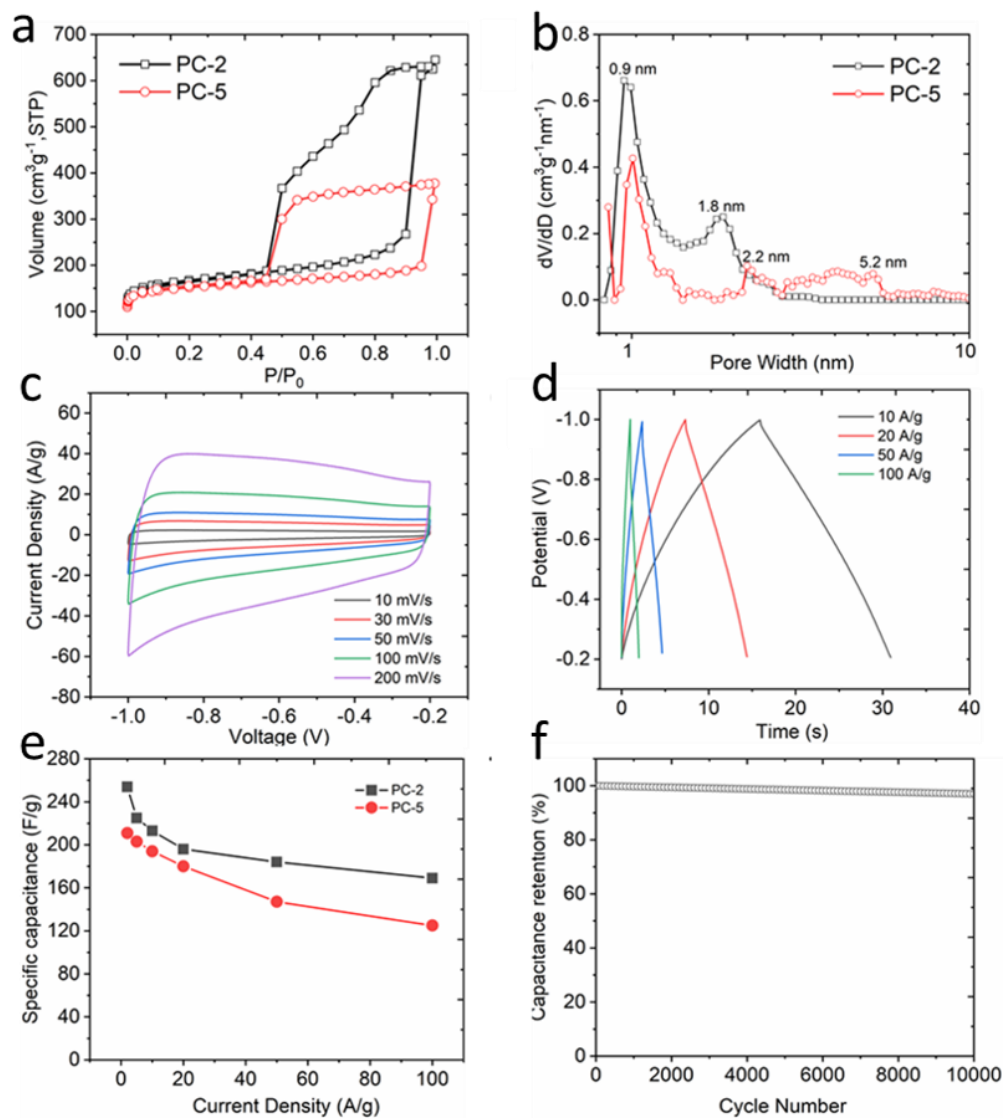
Figure 5.11 (a) Nitrogen absorption-desorption isotherms of PC-2 and PC-5 collected at liquid nitrogen temperature (77k). (b) The micro and meso pore size distribution of PC-5 calculated from absorption-desorption isotherms using DFT method. (c) Cyclic voltammograms collected at various scan rates of PC-5. (d) GCD profiles collected at various current densities of PC-5. e) Gravimetric capacitance measured at different current densities. (e) The capacitance stability of PC-5 after 10000 cycle.
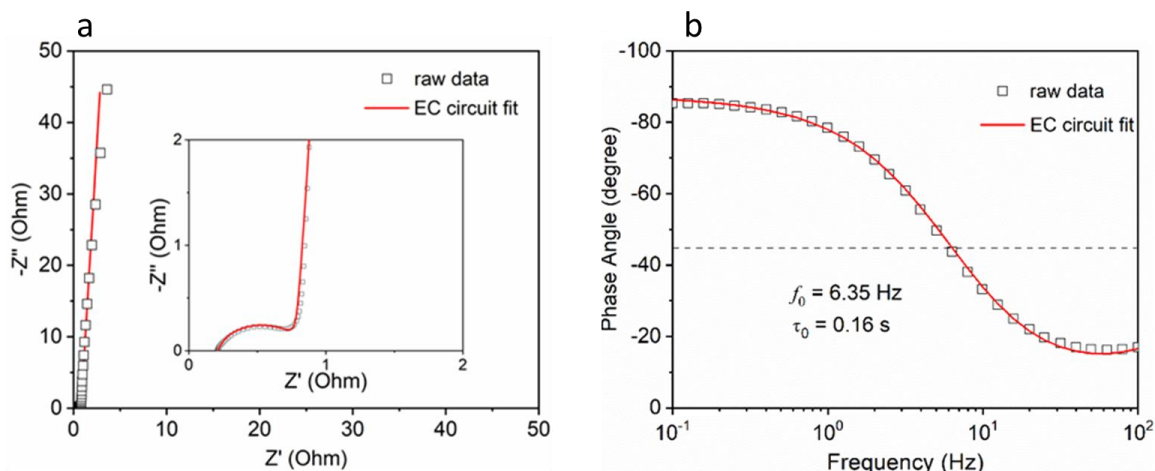
Figure 5.12 The electrochemical test of PC-5. (a) Nyquist plot collected at open circuit potential from 0.1 to 10^5 Hz with a perturbation of 5 mV. Inset shows the high frequency region. (b) Bode phase plot. Dashed line highlights the characteristic frequency f_0 ($1/\tau_0$) at the phase angle of -45°.

The fabrication approach described here is compatible with a variety of precursors toward functional porous solids. Adding electrochemically active nanoparticles into the hybrid precursor leads to composite electrodes with nanoparticles embedded in porous carbon matrices. In order to improve the electrode capacity, we chose iron oxide, an anode material in LIBs known for its high specific capacity (> 900 mAhg^{-1}). Recent studies have shown that the capacity of carbon-based anodes can be improved dramatically by the inclusion of Si, Sn or metal oxides including iron oxide.[230-233] Preparation of hybrid precursor films comprising BBCP template, resol and iron oxide nanoparticles followed a similar procedure as specified in sector 5.2.3. It is worth mentioning that iron oxide is photothermally active to convert light irradiation into heat. Previously, our group reported using gold nanoparticles to photothermally convert polyhedral oligomeric silsesquioxane into porous silica.[53] Photothermal processing of the composite under ambient conditions was conducted using a xenon flash lamp with light emission over a large range of wavelengths from approximately 200 nm to 1000 nm. Typical pulse durations were 0.3

98

millisecond and a typical process sequence employed 6-10 pulses. The light energy density is tunable through the variation of voltage and/or pulse duration time. The iron oxide nanoparticles absorb strongly in the emission band of the flash lamp; the local heating converts resol to amorphous carbon and pyrolyzes the BBCP template, removing it from the film. This resulted in nanoporous carbon films decorated with iron oxide nanoparticles. The carbon matrix serves as a conductive network to support the Fe_2O_3 conversion in LIB cycling tests.

The performance of the carbon/Fe_2O_3 composite anode is shown in Figure 5.13. The distinct lithiation plateau at 0.8 V (vs Li/Li^+) indicates the good reactivity of iron oxide. Under the current of 200 mAg^{-1}, the composite electrode exhibited specific capacity as high as 1550 $mAhg^{-1}$ for the 1st discharge. This high capacity, together with the relatively low Columbic efficiency (Figure 5.12b), indicate the high surface area of the porous composite and the resultant parasitic irreversible reactions at the interfaces. These reactions include the solid electrolyte interface (SEI) formation, and possibly the corrosion-like reactions of the carbon matrix [234-235]. The capacity of composite electrode gradually stabilized after several lithiation/delithiation cycles and generated a specific capacity approximately 900 $mAhg^{-1}$, which is comparable to some of the best performing ferrite containing electrodes.[212] As current density increased to 300 mAg^{-1} and 400 mAg^{-1}, the electrode demonstrated capacities of 600 $mAhg^{-1}$ and 450 $mAhg^{-1}$.
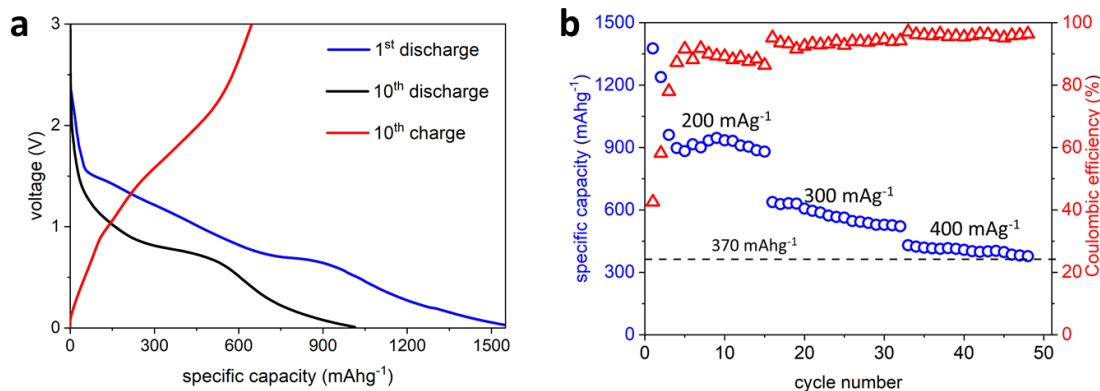
Figure 5.13 Galvanostatic charge/discharge performance of the mesoporous carbon/iron/iron oxide electrode within a potential window from 0.01V to 3V. (a)Profiles of the 1st, 10th discharge and the 10th charge under the current density of 200 mAg^{-1}.(b)Rate performance and Coulombic efficiency for the first 50 cycles of charge/discharge under varied cycling currents. The sample tested was made by 8 light pulses.

5.4 Conclusions and Future Work

In summary, we explored the additive-driven assembly of PDMS-*b*-PEO BBCPs into spherical morphologies. Using resol as hydrogen bond donor, we achieved precise control of the spherical domain sizes over a large range (18-150 nm) by varying the M_w of BBCPs templates. Upon pyrolysis, nanoporous carbon films with pore sizes from 16 to 107 nanometers were readily obtained, serving as promising electrode materials for high-rate EDLCs. This strategy enables the completion of full access to the size spectrum of nanopores by using organic templates. We believe that the strategy can be extended to other systems, such as well-ordered porous silica and metal oxides.

The addition of photothermally active Fe_2O_3 not only improves charge storage capacities, but also allows the rapid photothermal pyrolysis to obtain the composite electrodes. Compared to other electrode materials that can be produced in large scale, the capacity of carbon/iron oxide composite prepared via photothermal processing is compelling and the method reported here provides an effective route to industrial scale

100

production of high-performance, binder-free anode for lithium ion batteries and beyond. Future studies will include texturing the anode via direct imprinting to increase anode surface area to provide pathways to increased charge-rate performance.

APPENDIX: ORGANIC CATHODE WORK

In this appendix, we document our progress in the development of a class of organic cathode materials. We have demonstrated a proof-of-concept that stepwise crosslinked hydroquinone-formaldehyde polymers can be used as cathodes in LIBs, and hybrid inks comprising the hydroquinone-formaldehyde oligomer and carbon nanotubes/graphene nanoflakes can be readily imprinted into 3D microelectrodes. This part, although may still require some future work, represent a critical aspect of our effort in developing novel electrode materials to enable high-performance power sources.

6.1 Introduction

Organic electrodes based on quinone-containing polymers for secondary batteries received increasing attention in recent years due to their high theoretical capacities (300-600 mAhg^{-1} for lithium-ion batteries),[236] versatile chemical structures from earth-abundant elements,[237] and greener synthesis relative to ceramic electrode materials. Despite these advantages, one common issue for quinones are their high solubility in organic electrolytes, leading to unstable electrochemical cycling performances. Methods to mitigate the solubility issue include forming quinone salts, polymerization of high-molecular weight macromolecules,[238] and applying solid-state or gel electrolytes.[239] Alternatively, inspired by the completely insoluble polymeric networks like elastomers and thermosets, crosslinking quinone-containing monomers and oligomers are promising routes to stabilize the electrode structures. Previously, hyper-crosslinked poly-pillar[5]quinone was reported to combine cycling stability and electrochemical reactivity.[240] Although the monomers possess high theoretical capacity (above 400 mAhg^{-1}) and the oligomeric (4 and 5 monomer units) counterparts have been demonstrated as

high-performance cathodes,[241] the material utilization efficiency of the crosslinked form was lower than expected. This is because on one hand, the micron-size crosslinked quinone particles lack the electronic conductivity to make full use of the materials buried inside (electronic pathways); on the other hand, the dense crosslinks prevent access of electrolyte to all active materials (ionic pathways). To address these challenges, in this work, we explore using quinone precursors that go through stepwise crosslinking- the oligomer forms are still soluble to allow the formation of hybrids; the second-step thermal crosslinking prevent the dissolution of active materials in the battery tests. Methods to further improve the electrolyte access, *e.g.* blending in plasticizers, were also explored.

Hybridizing with high-surface area carbon additives, *e.g.* graphene and carbon nanotubes (CNTs) in the solution phase is effective to improve the electronic conductivity of the hybrid electrode materials. For example, self-polymerization of dopamine with the presence of CNTs in water resulted in hybrid electrodes with robust, conformal coating of polydopamine on the surfaces of CNTs.[242] The assembly of the dissolved quinone precursors-either monomers or oligomers, with carbon additives in the solution phase, allows better contact of the precursor to the conductive carbon networks, relative to their fully cured particle forms.

Base-catalyzed phenol-formaldehyde oligomer ($M_w \sim$ 500-2000 g mol^{-1}), or else termed as "resol", is a widely used prepolymer to create phenolic thermosets. Similarly, hydroquinone is expected to go through polycondensation with formaldehyde to form network structures. In fact, Pirnat *et al* reported hydrochloric acid catalyzed, one-step crosslinking of nanoporous quinone-formaldehyde particles that demonstrated electrochemical reactivity in lithium-ion batteries (LIBs).[243] Here we report the

preparation of quinone-formaldehyde oligomers (M_w< 2000 g mol^{-1}) in basic environment. These oligomers demonstrate solubility in a variety of organic solvents including ethanol, dimethylformamide (DMF) and N-methyl pyrrolidone (NMP), enabling molecularly mixing with graphene nanosheets in solvent. Further thermal treatment induces complete crosslinking of quinone-formaldehyde resin on the surfaces of graphene sheets. This report presents simple, solution-processable quinone electrode preparation based on common monomers, which holds potential for large-scale fabrication.

6.2 Experimental Section

6.2.1 Synthesis of Quinone-Formaldehyde Oligomers

The synthesis followed a modified preparation procedure for phenol-formaldehyde prepolymers. In a typical synthesis, 6.6 g phenol, 0.5 g sodium hydroxide were dissolved in a mixture solvent (25 ml) comprising ethanol and water (1:4) and was stirred at 60℃ oil bath till the mixture turned a homogeneous dark solution. 9.0 g formalin (30 wt% of formaldehyde in water) was added dropwise within 10 min and the mixture was kept at 78℃ for approximately 30 min. Subsequently, 50 ml of N-methyl pyrrolidone (NMP) was added and the mixture was neutralized with 2 M HCl. The residual water and ethanol were removed under a nitrogen flow; NaCl precipitated due to poor solubility in NMP and was removed by subsequent filtration.

6.2.2 Synthesis of Copolymer Plasticizer

Dopamine acrylamide (DMA) and poly(dopamine acrylamide)-co-poly(ethylene glycol) methyl ether methacrylate (PDMA-co-PEG950) were synthesized and purified by following reported methods. In a typical synthesis, poly(ethylene glycol) methyl ether methacrylate (PEG950, Mw=950 gmol^{-1}, Sigma-Aldrich) was purified using basic Al$_2$O$_3$

column to remove the inhibitor. DMA (1.1 g), PEG950 (5.0 g) and azobisisobutyronitrile (AIBN, 0.11 g) were dissolved in 15 ml DMF in a 50 ml Schlenk flask. The system was degassed through three freeze-pump-thaw cycles and stirred overnight at 60 ℃. The polymer was precipitated in ethyl ether three times before dried in oven.

6.2.3 Preparation of Hybrid Electrodes

Composition of the electrodes are specified in Table X. In a typical preparation, appropriate amount of copolymer plasticizer, quinone prepolymer and graphene nanoflakes were dispersed in NMP and assisted with a speed mixer (2500 rpm, 10 min). The resultant dispersion was poured into an aluminum pan and dried at room temperature under nitrogen flow with subsequent curing at 120℃ for 2 hours.

Table 6.1 Quinone-formaldehyde composite electrode sample composition

sample	copolymer plasticizer (mg)	quinone prepolymer (mg)	graphene nanoflakes (mg)	polymer weight percent (%)
A1	10	50	140	30
A2	20	40	140	30
A3	40	20	140	30
B1	10	50	60	50
B2	20	40	60	50
B3	40	20	60	50

6.2.4 Physical and Electrochemical Characterizations of Hybrid Electrodes

FTIR measurements were carried out using a PerkinElmer spectrometer with universal ATR sampling accessory. Surface morphology of polymer blends were characterized by Dimension 3100 AFM. Field effect scanning electron microscopy (FESEM) were conducted on Magellan 400. Electrochemical measurements were

conducted in Swagelok cells assembled in an argon filled glove box. LiTFSI (1M, in 1,3-dioxolane/dimethoxyethane=1/1 by volume) was used as the liquid electrolyte. A piece of lithium metal served as both the counter and reference electrode. Galvanostatic charge and discharge were measured on a Maccor 4304 electrochemical workstation. Cyclic voltammetry was conducted on CHI660 workstation. Impedance spectroscopy was conducted using a Gamry600 potentiostat.

6.2.5 Imprinting of Hybrid Electrodes

Silicon master mold with a grid pattern of 2 μm (width)-5 μm (height)-10 μm (pitch) was used to transfer pattern to PDMS stamps based on Sylgard 184 (Dow Corning). Hybrid ink comprising appropriate amount of quinone prepolymer and carbon nanofiber was drop cast onto the substrate at 600 rpm for 10 s, followed with PDMS stamp embossing. After that, samples were soft baked at 70 ℃ for approximately 30 min and heated at 120 ℃ for 10 min in an oven before demolding. Finally, the imprints were further cured at 120 ℃ for 2 hours.

6.3 Results and Discussion

6.3.1 Synthesis of Quinone-Formaldehyde Oligomers

The synthesis of quinone-formaldehyde prepolymer is illustrated in Figure 6.1a. The molecular weight of the prepolymer is approximately 1500 $gmol^{-1}$, as confirmed by gel permeation chromatography (GPC). Further crosslinking at elevated temperature oxidized hydroquinone to quinone, supported by the appearance of distinct carbonyl IR absorption at 1660 cm^{-1} and the decreased -OH stretching absorption in the fully cured quinone-formaldehyde polymer (Figure 6.1b). The oligomer has good solubility in organic solvent like NMP while after crosslinking, the network structure has minimal solubility in

a variety of solvents including dimethylformamide (DMF), propylene carbonate (PC) and dimethyl carbonate (DMC), as shown in Figure 6.1c. The solubility change offers significant advantages for solution processing of oligomers and the stable electrochemical cycling after curing.
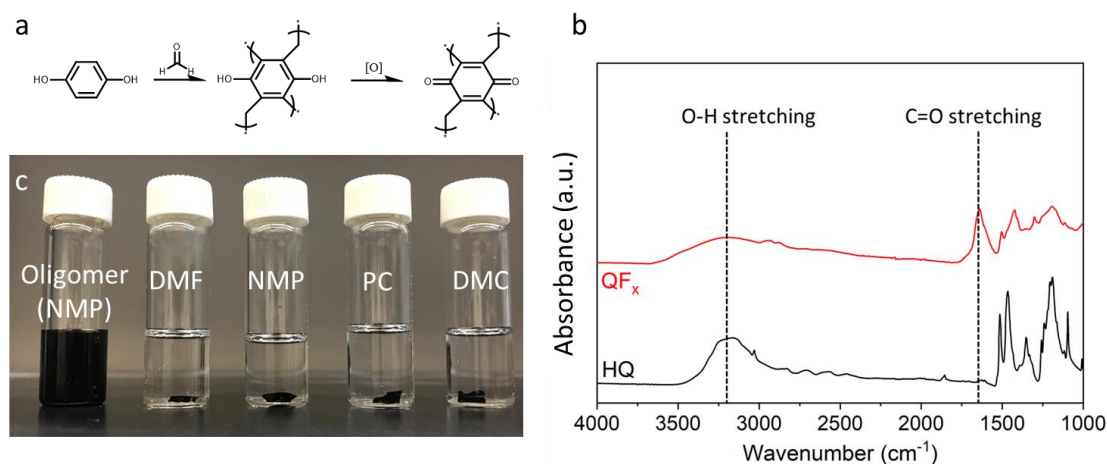
Figure 6.1 (a) Synthesis procedure of quinone-formaldehyde polymers. (b) FTIR traces of oligomeric and fully crosslinked quinone-formaldehydes. (c) photographs showing solubility difference of the polymer before and after crosslinking in various solvents.

6.3.2 Hybrid Electrodes and Electrochemical Performance

We first characterized the electrochemical reactivity of quinone-formaldehyde oligomer using galvanostatic charge and discharge measurement (Figure 6.2a). The oligomer showed reversible capacity of 291.8 mAhg^{-1} with Coulombic efficiency over 98%. The high capacity is consistent with our expectation as the oligomer contains high portion of the active quinone functionalities. Without full crosslinking, the composite electrode suffered from gradual capacity loss as quinone-formaldehyde oligomer has high solubility in the organic electrolyte. Using the same preparation method, heating the electrode at elevated temperature before electrochemical tests enabled further crosslinking of the

molecules. However, as shown in Figure 6.2b, we observed distinct capacity decrease from the oligomer state to the cured network state. We surmise that high crosslinking density and the resultant low free volume prevents electrolyte to have access to the bulk quinone-formaldehyde. The appearance of high overpotential during charging supports our hypothesis; the densely crosslinked network caused the sluggish electrolyte diffusion and the premature ending of delithiation.
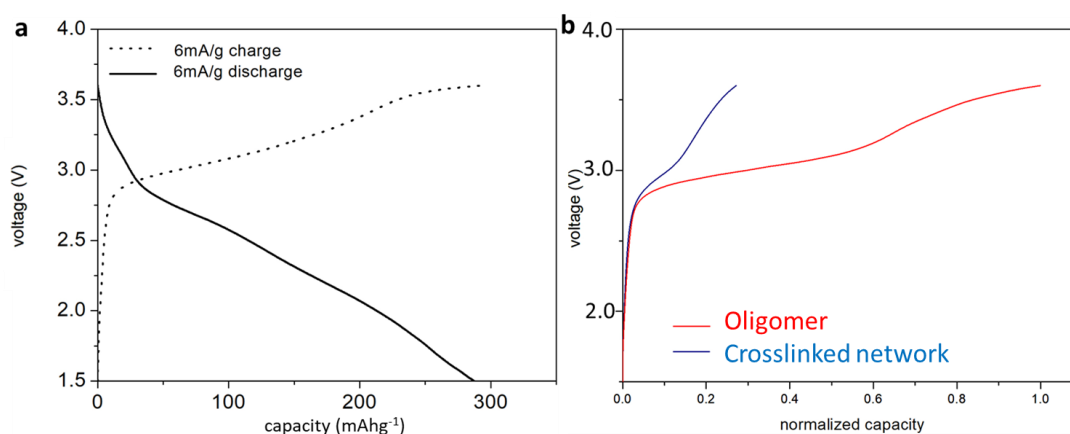
Figure 6.2 (a) Charge and discharge profiles oligomeric quinone-formaldehyde between 1.5V and 3.5 V vs. Li/Li$^+$ at a current density of 6mAg^{-1}. (b) Charge profiles of quinone-formaldehyde before and after crosslinking without adding copolymer plasticizers.

To mitigate the effect from free volume loss, we synthesized a random copolymer PDMA-co-PEG950 as a plasticizer. The dopamine containing monomer help with the mixing with quinone-formaldehyde due to chemical similarity. The short-chain PEO containing monomer will have favorable interaction with the LiTFSI electrolyte, serving as an embedded gel electrolyte (after complexing with LiTFSI liquid electrolyte) in the hybrid electrode. Phase graphs from atomic force microscopy measurement (Figure 6.3) show that mixing copolymer plasticizer with quinone-formaldehyde by various ratios (1:5, 1:2 and 2:1 plasticizer/quinone by weight) all leads to mixtures with small domain size of

a few tens of nanometers. Cyclic voltammetry of electrode after blending in 33% plasticizer (sample A2) is shown in Figure 6.3a. Distinct anodic peak at 2.8 V and cathodic peak at 2.7 V are consistent with previous literature on quinone based cathode materials. The broadening of the peaks indicates the existence of different chemical environment of carbonyl groups. The scan rate dependence of anodic and cathodic peak intensities shows scaling factors of 0.7 and 0.69 respectively (Figure 6.4b), suggesting that the electrochemical process is a mixture of diffusion- and surface-controlled processes. We surmise that the graphene nanoflakes also contribute to the capacity via capacitive charge storage.
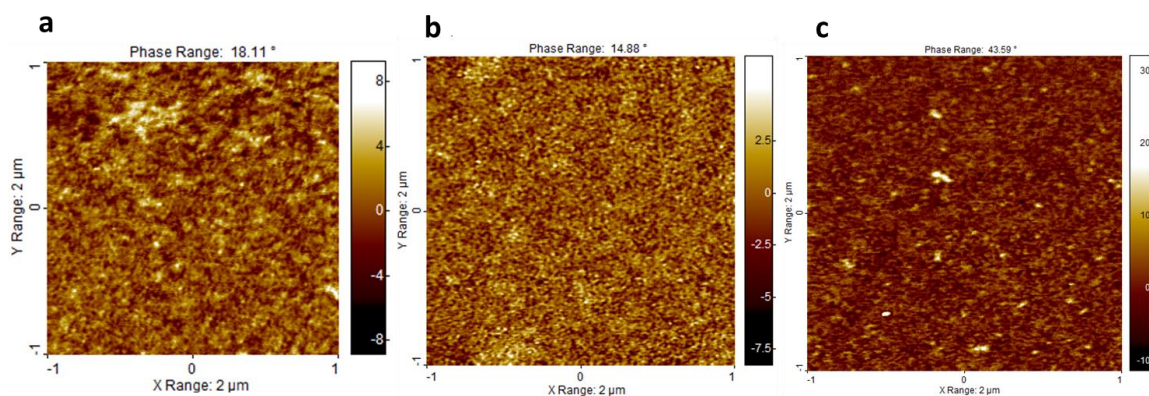
Figure 6.3 AFM imaging of quinone-formaldehyde blending with PDMA-co-PEG950 plasticizer with a ratio of 1:5, 1:2 and 2:1 by weight.
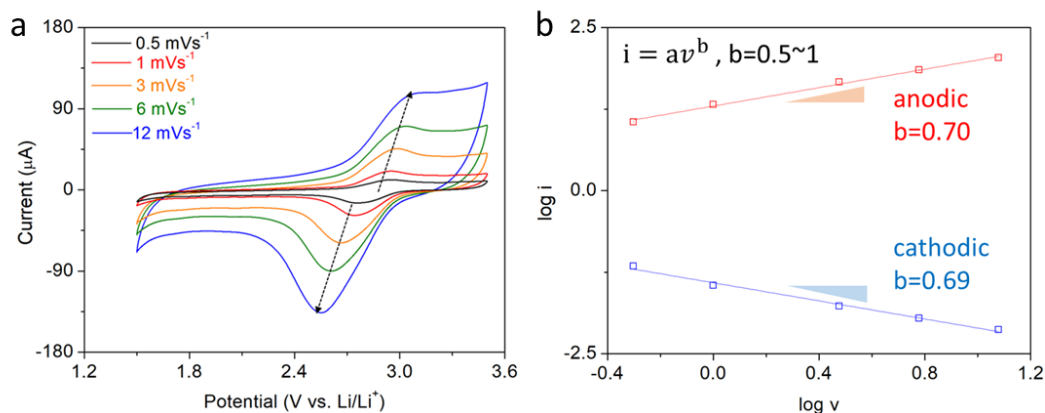
Figure 6.4 (a) Cyclic voltammetry of sample A2 at scan rates of 0.5, 1, 3, 6 and 12 mVs^{-1}. (b) scaling factors for anodic and cathodic processes.

EIS measurement of the composite electrode is shown in Figure 6.5a. In comparison with the Randles equivalent circuit model, we modified the capacitor components to be constant phase elements (CPEs) to account for the distributed activation energies in the electrochemical system. The fitted charge transfer resistance is approximately 850 Ω; the relatively large value is a result of the crosslinking and is consistent with our prior discussion. From the Warburg resistance (Figure 6.5b), corresponding to the impedance response in the middle frequencies, we can calculate the Warburg coefficient (890.2 Ωs$^{-1/2}$) corresponding to the diffusion of electrolyte in the bulk electrode. Future work in this end includes the full EIS measurement of all the six samples and compare the Warburg coefficient values. It is reasonable to expect that increasing plasticizer loading decreases the coefficient.
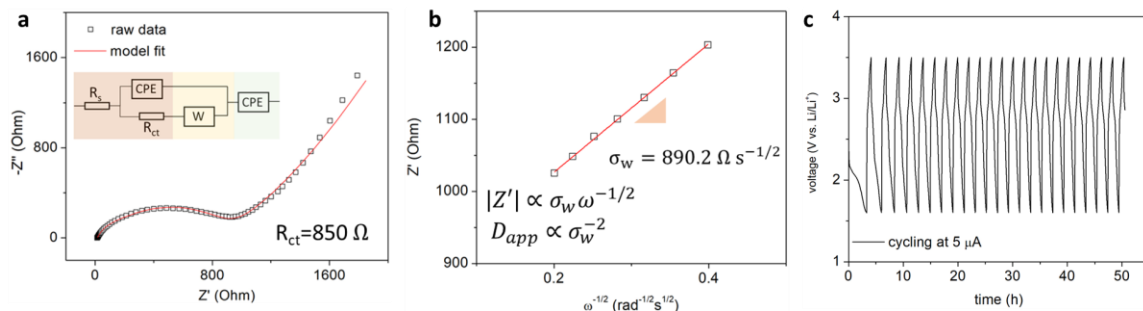
Figure 6.5 (a) EIS Nyquist plot of sample A2 and the equivalent circuit model (inset). (b) Relationship and linear fit of Z' and $\omega^{-1/2}$. The slope corresponds to the Warburg coefficient. (c) Cycling profile of sample A2 at 5 µA.

The charge and discharge profiles of sample A2 are shown in Figure 6.5c. Distinct plateaus at 2.8 V can be seen with small overpotential, which is consistent with the cyclic voltammetry measurement. The calculated specific capacity (normalized to the mass of quinone-formaldehyde polymer only) is approximately 118 mAhg^{-1}, and the overall capacity of composite electrode is 35.4 mAhg^{-1}. Future work in this end includes the full galvanostatic measurement of all the 6 samples to find the best performing specific capacity for active materials only and for the composite electrode. In fact, the relatively small loading of active materials is a common challenge in the field of study. As quinone based polymer cathodes have much lower electronic conductivities than their inorganic counterpart, they rely heavily on carbon based additives; the method of sample preparation, and the quality of contact between polymer and conductive additives are critical to the battery performance.

6.3.3 Compatibility with Micropatterning

We have previously shown that imprinting electrode precursors into microelectrodes with high surface-to-volume ratio improves the materials utilization

efficiency, leading to higher specific capacity. For demonstration purposes, we created microline array of quinone-formaldehyde polymer using imprint lithography as shown in Figure 6.3. The imprints possess good structure integrity with approximately 1 μm in width, 3.8 μm in height and 10 μm in pitch, reaching an aspect ratio of 3.8. It is reasonable to believe that the precursor is also compatible with the larger scale coating and patterning techniques, including the roll-to-roll coating and screen printing. If targeting at smaller feature sizes, the resolution limit is dependent on the dimensions of the carbon additives. In this demonstration, we found challenges of reaching nanoscale pattern or patterning hybrid precursors with a high loading of carbon nanofibers. However, by using better dispersed additives, *e.g.*, graphene nanosheets, carbon nanoparticles and carbon nanotubes, smaller feature patterning is possible.
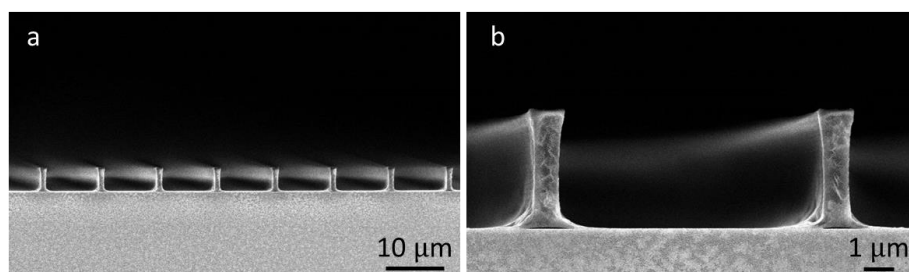
Figure 6.6 SEM imaging of imprinted quinone-formaldehyde electrodes.

6.4 Conclusions and Future Work

In summary, we utilized simple chemicals, *i.e.*, hydroquinone and formaldehyde, to obtain quinone-formaldehyde oligomers. By hybridizing the oligomer with graphene nanoflakes, the composite electrode demonstrated high specific capacity of approximately 300 mAhg^{-1}. Crosslinking induced capacity decay due to loss of free volume can be

mitigated by using a copolymer plasticizer, leading to specific capacity above 100 mAhg^{-1}, which is comparable with benchmark cathode materials, e.g., $LiMn_2O_4$ (110 mAhg^{-1}), $LiCoO_2$ (140 mAhg^{-1}) and $LiFePO_4$ (170 mAhg^{-1}). The precursor can be readily patterned into microscale features, demonstrating potentials for applications in light-weight power sources with small form factors. Future works include more detailed electrochemical characterizations of composite electrode samples with different active materials loading.

BIBLIOGRAPHY

[1]   S. M. Spearing, *Acta Mater.* **2000**, *48*, 179-196.

[2]   H. G. Craighead, *Science* **2000**, *290*, 1532-1535.

[3]   W. F. Brinkman, M. R. Pinto, *Bell Labs Technical Journal* **1997**, *2*, 57-75.

[4]   S. Ferrari, M. Loveridge, S. D. Beattie, M. Jahn, R. J. Dashwood, R. Bhagat, *J. Power Sources* **2015**, *286*, 25-46.

[5]   R. W. Hart, H. S. White, B. Dunn, D. R. Rolison, *Electrochemistry Communications* **2003**, *5*, 120-123.

[6]   E. Menard, M. A. Meitl, Y. G. Sun, J. U. Park, D. J. L. Shir, Y. S. Nam, S. Jeon, J. A. Rogers, *Chemical Reviews* **2007**, *107*, 1117-1160.

[7]   D. A. LaVan, T. McGuire, R. Langer, *Nature Biotechnology* **2003**, *21*, 1184-1191.

[8]   Y. N. Xia, G. M. Whitesides, *Angew. Chem.-Int. Edit.* **1998**, *37*, 550-575.

[9]   D. Qin, Y. N. Xia, G. M. Whitesides, *Nature Protocols* **2010**, *5*, 491-502.

[10]   K. M. Vaeth, R. J. Jackman, A. J. Black, G. M. Whitesides, K. F. Jensen, *Langmuir* **2000**, *16*, 8495-8500.

[11]   T. Paik, H. Yun, B. Fleury, S. H. Hong, P. S. Jo, Y. T. Wu, S. J. Oh, M. Cargnello, H. Yang, C. B. Murray, C. R. Kagan, *Nano Lett.* **2017**, *17*, 1387-1394.

[12]   J. Yoon, S.-M. Lee, D. Kang, M. A. Meitl, C. A. Bower, J. A. Rogers, *Advanced Optical Materials* **2015**, n/a-n/a.

[13]   J. H. Ahn, H. S. Kim, K. J. Lee, S. Jeon, S. J. Kang, Y. G. Sun, R. G. Nuzzo, J. A. Rogers, *Science* **2006**, *314*, 1754-1757.

[14]   E. Kim, Y. N. Xia, G. M. Whitesides, *J. Am. Chem. Soc.* **1996**, *118*, 5722-5731.

[15]   S. S. Williams, S. Retterer, R. Lopez, R. Ruiz, E. T. Samulski, J. M. DeSimone, *Nano Lett.* **2010**, *10*, 1421-1428.

[16]   Y. Zhang, C. W. Lo, J. A. Taylor, S. Yang, *Langmuir* **2006**, *22*, 8595-8601.

[17]   R. Sreenivasan, K. K. Gleason, *Chem. Vapor Depos.* **2009**, *15*, 77-90.

[18]   C. P. Tan, H. G. Craighead, *Materials* **2010**, *3*, 1803-1832.

[19]   X. Z. Xie, L. Rieth, S. Merugu, P. Tathireddy, F. Solzbacher, *Applied Physics Letters* **2012**, *101*, 5

.

[20]   G. Mordi, S. Jandhyala, C. Floresca, S. McDonnell, M. J. Kim, R. M. Wallace, L. Colombo, J. Kim, *Applied Physics Letters* **2012**, *100*, 3.

[21]   A. M. Mahmoud, A. J. Bergren, N. Pekas, R. L. McCreery, *Adv. Funct. Mater.* **2011**, *21*, 2273-2281.

[22]   P. Kovacik, G. d. Hierro, W. Livernois, K. K. Gleason, *Materials Horizons* **2015**, *2*, 221-227.

[23]   A. M. Coclite, R. M. Howden, D. C. Borrelli, C. D. Petruczok, R. Yang, J. L. Yague, A. Ugur, N. Chen, S. Lee, W. J. Jo, A. D. Liu, X. X. Wang, K. K. Gleason, *Adv. Mater.* **2013**, *25*, 5392-5422.

[24]   K. K. S. Lau, K. K. Gleason, *Macromolecules* **2006**, *39*, 3688-3694.

[25]   Y. Mao, K. K. Gleason, *Langmuir* **2004**, *20*, 2484-2488.

[26]   H. G. Pryce Lewis, J. A. Caulfield, K. K. Gleason, *Langmuir* **2001**, *17*, 7652-7655.
[27]   K. K. S. Lau, K. K. Gleason, *Macromolecules* **2006**, *39*, 3695-3703.

[28]   S. Yoo, J.-H. Kim, M. Shin, H. Park, J.-H. Kim, S.-Y. Lee, S. Park, *Science Advances* **2015**, *1*, e1500101.

[29]   C. M. Parlett, K. Wilson, A. F. Lee, *Chem Soc Rev* **2013**, *42*, 3876-3893.

[30]   B. R. Sveinbjörnsson, R. A. Weitekamp, G. M. Miyake, Y. Xia, H. A. Atwater, R. H. Grubbs, *PNAS* **2012**, *109*, 14332-14336.

[31]   O. D. Velev, E. W. Kaler, *Adv. Mater.* **2000**, *12*, 531-534.

[32]   J. G. Werner, G. G. Rodriguez-Calero, H. D. Abruna, U. Wiesner, *Energy Environ. Sci.* **2018**, *11*, 1261-1270.

[33]   F. Zhang, T. Y. Liu, M. Y. Li, M. H. Yu, Y. Luo, Y. X. Tong, Y. Li, *Nano Lett.* **2017**, *17*, 3097-3104.

[34]   A. H. Lu, F. Schüth, *Adv. Mater.* **2006**, *18*, 1793-1805.

[35]   S. H. Park, Y. N. Xia, *Adv. Mater.* **1998**, *10*, 1045-+.

[36]   G.-R. Yi, J. H. Moon, S.-M. Yang, *Chemistry of Materials* **2001**, *13*, 2613-2618.

[37]   T. Y. Liu, F. Zhang, Y. Song, Y. Li, *J. Mater. Chem. A* **2017**, *5*, 17705-17733.

[38]   M. Stefik, S. Guldin, S. Vignolini, U. Wiesner, U. Steiner, *Chemical Society Reviews* **2015**, *44*, 5076-5091.

[39]   M. C. Orilall, U. Wiesner, *Chemical Society Reviews* **2011**, *40*, 520-535.

[40]   G. J. d. A. A. Soler-Illia, E. L. Crepaldi, D. Grosso, C. Sanchez, *Current Opinion in Colloid & Interface Science* **2003**, *8*, 109-126.

[41]   C. M. Bates, F. S. Bates, *Macromolecules* **2017**, *50*, 3-22.

[42]   F. S. Bates, G. H. Fredrickson, *Phys. Today* **1999**, *52*, 32-38.

[43]   E. W. Cochran, C. J. Garcia-Cervera, G. H. Fredrickson, *Macromolecules* **2006**, *39*, 2449-2451.

[44]   D. P. Song, Y. Lin, Y. Gai, N. S. Colella, C. Li, X. H. Liu, S. Gido, J. J. Watkins, *J. Am. Chem. Soc.* **2015**, *137*, 3771-3774.

[45]   Y. Deng, J. Liu, C. Liu, D. Gu, Z. Sun, J. Wei, J. Zhang, L. Zhang, B. Tu, D. Zhao, *Chem. Mater.* **2008**, *20*, 7281-7286.

[46]   Y. Meng, D. Gu, F. Q. Zhang, Y. F. Shi, H. F. Yang, Z. Li, C. Z. Yu, B. Tu, D. Y. Zhao, *Angew. Chem.-Int. Edit.* **2005**, *44*, 7053-7059.

[47]   Y. Deng, Y. Cai, Z. Sun, D. Gu, J. Wei, W. Li, X. Guo, J. Yang, D. Zhao, *Adv. Funct. Mater.* **2010**, *20*, 3658-3665.

[48]   Z. Qiang, Y. H. Guo, H. Liu, S. Z. D. Cheng, M. Cakmak, K. A. Cavicchi, B. D. Vogt, *ACS Appl. Mater. Interfaces* **2015**, *7*, 4306-4310.

[49]   A. B. Chang, T. P. Lin, N. B. Thompson, S. X. Luo, A. L. Liberman-Martin, H. Y. Chen, B. Lee, R. H. Grubbs, *J Am Chem Soc* **2017**, *139*, 17683-17693.

[50]   T. P. Lin, A. B. Chang, S. X. Luo, H. Y. Chen, B. Lee, R. H. Grubbs, *ACS Nano* **2017**, *11*, 11632-11641.

[51]   Yan Xia, Bradley D. Olsen, Julia A. Kornfield, R. H. Grubbs, *J Am Chem Soc* **2009**, *131*, 18525-18532.

[52]   D. P. Song, G. Jacucci, F. Dundar, A. Naik, H. F. Fei, S. Vignolini, J. J. Watkins, *Macromolecules* **2018**, *51*, 2395-2400.

[53]   D. P. Song, A. Naik, S. K. Li, A. Ribbe, J. J. Watkins, *J. Am. Chem. Soc.* **2016**, *138*, 13473-13476.

[54]   D. P. Song, C. Li, W. H. Li, J. J. Watkins, *ACS Nano* **2016**, *10*, 1216-1223.

[55]   D.-P. Song, S. Shahin, W. Xie, S. Mehravar, X. Liu, C. Li, R. A. Norwood, J.-H. Lee, J. J. Watkins, *Macromolecules* **2016**, *49*, 5068-5075.

[56]   D.-P. Song, C. Li, N. S. Colella, X. Lu, J.-H. Lee, J. J. Watkins, *Advanced Optical Materials* **2015**, *3*, 1169-1175.

[57]   K. Zhang, X. P. Han, Z. Hu, X. L. Zhang, Z. L. Tao, J. Chen, *Chemical Society Reviews* **2015**, *44*, 699-728.

[58]   B. Gyenes, D. A. Stevens, V. L. Chevrier, J. R. Dahn, *Journal of the Electrochemical Society* **2015**, *162*, A278-A283.

[59]   D. R. Rolison, L. F. Nazar, *Mrs Bulletin* **2011**, *36*, 486-493.

[60]   M. Armand, J. M. Tarascon, *Nature* **2008**, *451*, 652-657.

[61]   N. Nitta, F. X. Wu, J. T. Lee, G. Yushin, *Mater Today* **2015**, *18*, 252-264.

[62]   S. Goriparti, E. Miele, F. De Angelis, E. Di Fabrizio, R. P. Zaccaria, C. Capiglia, *J. Power Sources* **2014**, *257*, 421-443.

[63]   B. Scrosati, J. Garche, *J. Power Sources* **2010**, *195*, 2419-2430.

[64]   J. M. Tarascon, M. Armand, *Nature* **2001**, *414*, 359-367.

[65]   A. M. Stephan, *European Polymer Journal* **2006**, *42*, 21-42.

[66]   J. Y. Song, Y. Y. Wang, C. C. Wan, *J. Power Sources* **1999**, *77*, 183-197.

[67]   S. Choi, T. W. Kwon, A. Coskun, J. W. Choi, *Science* **2017**, *357*, 4.

[68]   R. R. Kohlmeyer, A. J. Blake, J. O. Hardin, E. A. Carmona, J. Carpena-Nunez, B. Maruyama, J. D. Berrigan, H. Huang, M. F. Durstock, *J. Mater. Chem. A* **2016**, *4*, 16856-16864.

[69]   L. A. Riley, A. S. Cavanagh, S. M. George, Y. S. Jung, Y. Yan, S.-H. Lee, A. C. Dillon, *ChemPhysChem* **2010**, *11*, 2124-2130.

[70]   F. Gardea, B. Glaz, J. Riddick, D. C. Lagoudas, M. Naraghi, *ACS Appl. Mater. Interfaces* **2015**, *7*, 9725-9735.

[71]   Z. G. Xue, D. He, X. L. Xie, *J. Mater. Chem. A* **2015**, *3*, 19218-19253.

[72]   L. Z. Long, S. J. Wang, M. Xiao, Y. Z. Meng, *J. Mater. Chem. A* **2016**, *4*, 10038-10069.

[73]   R. J. Sengwa, P. Dhatarwal, S. Choudhary, *Current Applied Physics* **2015**, *15*, 135-143.

[74]   R. J. Sengwa, P. Dhatarwal, S. Choudhary, *Electrochimica Acta* **2014**, *142*, 359-370.

[75]   V. Augustyn, P. Simon, B. Dunn, *Energy Environ. Sci.* **2014**, *7*, 1597-1614.

[76]   P. Simon, Y. Gogotsi, B. Dunn, *Science* **2014**, *343*, 1210.

[77]   P. Simon, Y. Gogotsi, B. Dunn, *Science* **2014**, *343*, 1210-1211.

[78]   J. W. Long, B. Dunn, D. R. Rolison, H. S. White, *Chemical Reviews* **2004**, *104*, 4463-4492.

[79]   J. W. Long, D. R. Rolison, *Accounts of Chemical Research* **2007**, *40*, 854-862.

[80]   B. Sun, H. D. Asfaw, D. Rehnlund, J. Mindemark, L. Nyholm, K. Edström, D. Brandell, *ACS Appl. Mater. Interfaces* **2018**, *10*, 2407-2413.

[81]   A. A. Talin, D. Ruzmetov, A. Kolmakov, K. McKelvey, N. Ware, F. El Gabaly, B. Dunn, H. S. White, *ACS Appl. Mater. Interfaces* **2016**, *8*, 32385-32391.

[82]   D. R. Rolison, J. W. Long, J. C. Lytle, A. E. Fischer, C. P. Rhodes, T. M. McEvoy, M. E. Bourga, A. M. Lubers, *Chemical Society Reviews* **2009**, *38*, 226-252.

[83]   H. G. Zhang, X. D. Yu, P. V. Braun, *Nat. Nanotechnol.* **2011**, *6*, 277-281.

[84]   N. S. Ergang, J. C. Lytle, K. T. Lee, S. M. Oh, W. H. Smyrl, A. Stein, *Adv. Mater.* **2006**, *18*, 1750-+.

[85]   D. McNulty, E. Carroll, C. O'Dwyer, *Advanced Energy Materials* **2017**, *7*, 8.

[86]   X. R. Wang, G. Yushin, *Energy Environ. Sci.* **2015**, *8*, 1889-1904.

[87]   P. H. L. Notten, F. Roozeboom, R. A. H. Niessen, L. Baggetto, *Adv. Mater.* **2007**, *19*, 4564-4567.

[88]   S. K. Cheah, E. Perre, M. Rooth, M. Fondell, A. Harsta, L. Nyholm, M. Boman, T. Gustafsson, J. Lu, P. Simon, K. Edstrom, *Nano Lett.* **2009**, *9*, 3230-3233.

[89]   K. Sun, T. S. Wei, B. Y. Ahn, J. Y. Seo, S. J. Dillon, J. A. Lewis, *Adv. Mater.* **2013**, *25*, 4539-4543.

[90] K. Dokko, J. Sugaya, H. Nakano, T. Yasukawa, T. Matsue, K. Kanamura, *Electrochemistry Communications* **2007**, *9*, 857-862.

[91] M. Tormen, E. Sovernigo, A. Pozzato, M. Pianigiani, M. Tormen, *Microelectronic Engineering* **2015**, *141*, 21-26.

[92] S. H. Ahn, L. J. Guo, *ACS Nano* **2009**, *3*, 2304-2310.

[93] J. C. Love, L. A. Estroff, J. K. Kriebel, R. G. Nuzzo, G. M. Whitesides, *Chemical Reviews* **2005**, *105*, 1103-1169.

[94] M. Leitgeb, D. Nees, S. Ruttloff, U. Palfinger, J. Gotz, R. Liska, M. R. Belegratis, B. Stadlober, *ACS Nano* **2016**, *10*, 4926-4941.

[95] J. Y. Park, N. R. Hendricks, K. R. Carter, *Langmuir* **2011**, *27*, 11251-11258.

[96] M. T. Li, H. Tan, L. Chen, J. Wang, S. Y. Chou, *J. Vac. Sci. Technol. B* **2003**, *21*, 660-663.

[97] S. H. Ko, I. Park, H. Pan, C. P. Grigoropoulos, A. P. Pisano, C. K. Luscombe, J. M. J. Frechet, *Nano Lett.* **2007**, *7*, 1869-1877.

[98] S. H. Lee, N. Y. Ha, *Optics Express* **2011**, *19*, 21803-21808.

[99] X. Yu, J. T. Pham, C. Subramani, B. Creran, Y. C. Yeh, K. Du, D. Patra, O. R. Miranda, A. J. Crosby, V. M. Rotello, *Adv. Mater.* **2012**, *24*, 6330-6334.

[100] Y. G. Y. Huang, W. X. Zhou, K. J. Hsia, E. Menard, J. U. Park, J. A. Rogers, A. G. Alleyne, *Langmuir* **2005**, *21*, 8058-8068.

[101] K. Y. Suh, Y. S. Kim, H. H. Lee, *Adv. Mater.* **2001**, *13*, 1386-1389.

[102] R. Kothari, M. R. Beaulieu, N. R. Hendricks, S. K. Li, J. J. Watkins, *Chemistry of Materials* **2017**, *29*, 3908-3918.

[103] A. Vu, Y. Q. Qian, A. Stein, *Advanced Energy Materials* **2012**, *2*, 1056-1085.

[104] V. Gentili, S. Brutti, L. J. Hardwick, A. R. Armstrong, S. Panero, P. G. Bruce, *Chemistry of Materials* **2012**, *24*, 4468-4476.

[105] A. K. Rai, L. T. Anh, J. Gim, V. Mathew, J. Kang, B. J. Paul, J. Song, J. Kim, *Electrochimica Acta* **2013**, *90*, 112-118.

[106] H. Lindstrom, S. Sodergren, A. Solbrand, H. Rensmo, J. Hjelm, A. Hagfeldt, S. E. Lindquist, *Journal of Physical Chemistry B* **1997**, *101*, 7717-7722.

[107] M. Roberts, P. Johns, J. Owen, D. Brandell, K. Edstrom, G. El Enany, C. Guery, D. Golodnitsky, M. Lacey, C. Lecoeur, H. Mazor, E. Peled, E. Perre, M. M. Shaijumon, P. Simon, P. L. Taberna, *J. Mater. Chem.* **2011**, *21*, 9876-9890.

[108] X. Y. Yu, H. B. Wu, L. Yu, F. X. Ma, X. W. Lou, *Angew. Chem.-Int. Edit.* **2015**, *54*, 4001-4004.

[109] J. H. Liu, J. S. Chen, X. F. Wei, X. W. Lou, X. W. Liu, *Adv. Mater.* **2011**, *23*, 998-1002.

[110] G. Q. Zhang, H. B. Wu, T. Song, U. Paik, X. W. Lou, *Angew. Chem.-Int. Edit.* **2014**, *53*, 12590-12593.

[111] H. S. Liu, Z. H. Bi, X. G. Sun, R. R. Unocic, M. P. Paranthaman, S. Dai, G. M. Brown, *Adv. Mater.* **2011**, *23*, 3450-+.

[112] W. Xu, Z. Y. Wang, Z. D. Guo, Y. Liu, N. Z. Zhou, B. Niu, Z. J. Shi, H. Zhang, *J. Power Sources* **2013**, *232*, 193-198.

[113] S. J. Park, Y. J. Kim, H. Lee, *J. Power Sources* **2011**, *196*, 5133-5137.

[114] J. S. Chen, X. W. Lou, *Chemical Science* **2011**, *2*, 2219-2223.

[115] J. Wang, Y. K. Zhou, B. Xiong, Y. Y. Zhao, X. J. Huang, Z. P. Shao, *Electrochimica Acta* **2013**, *88*, 847-857.

[116] N. A. Kaskhedikar, J. Maier, *Adv. Mater.* **2009**, *21*, 2664-2680.

[117] D. Y. Pan, S. Wang, B. Zhao, M. H. Wu, H. J. Zhang, Y. Wang, Z. Jiao, *Chemistry of Materials* **2009**, *21*, 3136-3142.

[118] A. Ferris, B. Reig, A. Eddarir, J.-F. Pierson, S. Garbarino, D. Guay, D. Pech, *ACS Energy Letters* **2017**, *2*, 1734-1739.

[119] N. D. Petkovich, B. E. Wilson, S. G. Rudisill, A. Stein, *ACS Appl. Mater. Interfaces* **2014**, *6*, 18215-18227.

[120] N. A. Kyerementeng, T. Brousse, D. Pech, *Nat. Nanotechnol.* **2017**, *12*, 7-15.

[121] H. Xia, Q. Y. Xia, B. H. Lin, J. W. Zhu, J. K. Seo, Y. S. Meng, *Nano Energy* **2016**, *22*, 475-482.

[122] W. Wei, G. Oltean, C. W. Tai, K. Edstrom, F. Bjorefors, L. Nyholm, *J. Mater. Chem. A* **2013**, *1*, 8160-8169.

[123] M. Letiche, E. Eustache, J. Freixas, A. Demortiere, V. De Andrade, L. Morgenroth, P. Tilmant, F. Vaurette, D. Troadec, P. Roussel, T. Brousse, C. Lethien, *Advanced Energy Materials* **2017**, *7*, 12.

[124] E. Cohen, S. Menkin, M. Lifshits, Y. Kamir, A. Gladkich, G. Kosa, D. Golodnitsky, *Electrochimica Acta* **2018**, *265*, 690-701.

[125] C. Y. Liu, E. I. Gillette, X. Y. Chen, A. J. Pearse, A. C. Kozen, M. A. Schroeder, K. E. Gregorczyk, S. B. Lee, G. W. Rubloff, *Nat. Nanotechnol.* **2014**, *9*, 1031-1039.

[126] H. Ning, J. H. Pikul, R. Zhang, X. Li, S. Xu, J. Wang, J. A. Rogers, W. P. King, P. V. Braun, *Proceedings of the National Academy of Sciences* **2015**, *112*, 6573-6578.

[127] H. S. Min, B. Y. Park, L. Taherabadi, C. L. Wang, Y. Yeh, R. Zaouk, M. J. Madou, B. Dunn, *J. Power Sources* **2008**, *178*, 795-800.

[128] K. Yoshima, H. Munakata, K. Kanamura, *J. Power Sources* **2012**, *208*, 404-408.

[129] B. B. Jiang, Y. J. He, B. Li, S. Q. Zhao, S. Wang, Y. B. He, Z. Q. Lin, *Angew. Chem.-Int. Edit.* **2017**, *56*, 1869-1872.

[130] Q. Zhao, Z. Q. Zhu, J. Chen, *Adv. Mater.* **2017**, *29*, 25.

[131] B. Jiang, C. Han, B. Li, Y. He, Z. Lin, *ACS Nano* **2016**, *10*, 2728-2735.

[132] M. R. Beaulieu, N. R. Hendricks, J. J. Watkins, *Acs Photonics* **2014**, *1*, 799-805.

[133] F. Dundar Arisoy, K. W. Kolewe, B. Homyak, I. S. Kurtz, J. D. Schiffman, J. J. Watkins, *ACS Appl. Mater. Interfaces* **2018**, *10*, 20055-20063.

[134] S. Li, A. Kazemi-Moridani, Y. Zhou, I. R. Howell, R. Kothari, J.-H. Lee, J. J. Watkins, *ACS Appl. Mater. Interfaces* **2018**.

[135] I. R. Howell, B. Giroire, A. Garcia, S. Li, C. Aymonier, J. J. Watkins, *J. Mater. Chem. C* **2018**, *6*, 1399-1406.

[136] B. C. Gross, J. L. Erkal, S. Y. Lockwood, C. P. Chen, D. M. Spence, *Anal. Chem.* **2014**, *86*, 3240-3253.

[137] W. Li, Y. Zhou, I. R. Howell, Y. Gai, A. R. Naik, S. Li, K. R. Carter, J. J. Watkins, *ACS Appl. Mater. Interfaces* **2018**.

[138] A. Laumann, M. Bremholm, P. Hald, M. Holzapfel, K. T. Fehr, B. B. Iversen, *Journal of the Electrochemical Society* **2012**, *159*, A166-A171.

[139] H. Lee, B. P. Lee, P. B. Messersmith, *Nature* **2007**, *448*, 338-U334.

[140] L. Lutterotti, *Nuclear Instruments & Methods in Physics Research Section B-Beam Interactions with Materials and Atoms* **2010**, *268*, 334-340.

[141] H. Berg, J. O. Thomas, W. Liu, G. C. Farrington, *Solid State Ionics* **1998**, *112*, 165-168.

[142] Z. M. Liu, N. Q. Zhang, K. N. Sun, *J. Mater. Chem.* **2012**, *22*, 11688-11693.

[143] T. L. Christiansen, E. D. Bojesen, M. Sondergaard, S. Birgisson, J. Becker, B. B. Iversen, *Crystengcomm* **2016**, *18*, 1996-2004.

[144] H. A. Barnes, *Journal of Rheology* **1989**, *33*, 329-366.

[145] Q. Feng, Y. Miyai, H. Kanoh, K. Ooi, *Langmuir* **1992**, *8*, 1861-1867.

[146] J. T. Hu, Y. Jiang, S. H. Cui, Y. D. Duan, T. C. Liu, H. Guo, L. P. Lin, Y. Lin, J. X. Zheng, K. Amine, F. Pan, *Advanced Energy Materials* **2016**, *6*, 8.

[147] Y. L. Liu, K. L. Ai, L. H. Lu, *Chemical Reviews* **2014**, *114*, 5057-5115.

[148] H. Gulley-Stahl, P. A. Hogan, W. L. Schmidt, S. J. Wall, A. Buhrlage, H. A. Bullen, *Environmental Science & Technology* **2010**, *44*, 4116-4121.

[149] B. J. Sparks, E. F. T. Hoff, L. P. Hayes, D. L. Patton, *Chemistry of Materials* **2012**, *24*, 3633-3642.

[150] H. Lee, S. M. Dellatore, W. M. Miller, P. B. Messersmith, *Science* **2007**, *318*, 426-430.

[151] Y. S. Zhu, F. X. Wang, L. L. Liu, S. Y. Xiao, Z. Chang, Y. P. Wu, *Energy Environ. Sci.* **2013**, *6*, 618-624.

[152] B. Reeja-Jayan, N. Chen, J. Lau, J. A. Kattirtzi, P. Moni, A. D. Liu, I. G. Miller, R. Kayser, A. P. Willard, B. Dunn, K. K. Gleason, *Macromolecules* **2015**, *48*, 5222-5229.

[153] E. Kazyak, K. H. Chen, K. N. Wood, A. L. Davis, T. Thompson, A. R. Bielinski, A. J. Sanchez, X. Wang, C. M. Wane, J. Sakamoto, N. P. Dasgupta, *Chemistry of Materials* **2017**, *29*, 3785-3792.

[154] A. M. Gaikwad, G. L. Whiting, D. A. Steingart, A. C. Arias, *Adv. Mater.* **2011**, *23*, 3251-+.

[155] D. Pech, M. Brunet, H. Durou, P. H. Huang, V. Mochalin, Y. Gogotsi, P. L. Taberna, P. Simon, *Nat. Nanotechnol.* **2010**, *5*, 651-654.

[156] M. F. El-Kady, V. Strong, S. Dubin, R. B. Kaner, *Science* **2012**, *335*, 1326-1330.

[157] J. Lin, C. G. Zhang, Z. Yan, Y. Zhu, Z. W. Peng, R. H. Hauge, D. Natelson, J. M. Tour, *Nano Lett.* **2013**, *13*, 72-78.

[158] M. Beidaghi, C. L. Wang, *Adv. Funct. Mater.* **2012**, *22*, 4501-4510.

[159] J. I. Hur, L. C. Smith, B. Dunn, *Joule* **2018**, *2*, 1187-1201.

[160] W. Li, T. L. Christiansen, C. Li, Y. Zhou, H. Fei, A. Mamakhel, B. B. Iversen, J. J. Watkins, *Nano Energy* **2018**, *52*, 431-440.

[161] V. Di Noto, S. Lavina, G. A. Giffin, E. Negro, B. Scrosati, *Electrochimica Acta* **2011**, *57*, 4-13.

[162] S. R. Gowda, A. L. M. Reddy, M. M. Shaijumon, X. B. Zhan, L. J. Ci, P. M. Ajayan, *Nano Lett.* **2011**, *11*, 101-106.

[163] C. S. Choi, J. Lau, J. Hur, L. Smith, C. L. Wang, B. Dunn, *Adv. Mater.* **2018**, *30*, 6.

[164] C. P. Rhodes, J. W. Long, M. S. Doescher, J. J. Fontanella, D. R. Rolison, *Journal of Physical Chemistry B* **2004**, *108*, 13079-13087.

[165] M. B. Sassin, J. W. Long, J. M. Wallace, D. R. Rolison, *Materials Horizons* **2015**, *2*, 502-508.

[166] N. Chen, B. Reeja-Jayan, J. Lau, P. Moni, A. D. Liu, B. Dunn, K. K. Gleason, *Materials Horizons* **2015**, *2*, 309-314.

[167] F. Pignanelli, M. Romero, R. Faccio, A. W. Mombru, *Journal of Physical Chemistry B* **2017**, *121*, 6759-6765.

[168] K. Chan, K. K. Gleason, *Langmuir* **2005**, *21*, 8930-8939.

[169] L. C. Bradley, M. Gupta, *Langmuir* **2015**, *31*, 7999-8005.

[170] E.-H. Kil, H.-J. Ha, S.-Y. Lee, *Macromolecular Chemistry and Physics* **2011**, *212*, 2217-2223.

[171] H. Duan, Y.-X. Yin, X.-X. Zeng, J.-Y. Li, J.-L. Shi, Y. Shi, R. Wen, Y.-G. Guo, L.-J. Wan, *Energy Storage Materials* **2018**, *10*, 85-91.

[172] D. Ruzmetov, V. P. Oleshko, P. M. Haney, H. J. Lezec, K. Karki, K. H. Baloch, A. K. Agrawal, A. V. Davydov, S. Krylyuk, Y. Liu, J. Y. Huang, M. Tanase, J. Cumings, A. A. Talin, *Nano Lett.* **2012**, *12*, 505-511.

[173]   A. J. Pearse, T. E. Schmitt, E. J. Fuller, F. El-Gabaly, C. F. Lin, K. Gerasopoulos, A. C. Kozen, A. A. Talin, G. Rubloff, K. E. Gregorczyk, *Chemistry of Materials* **2017**, *29*, 3740-3753.

[174]   M. Forsyth, D. R. MacFarlane, A. J. Hill, *Electrochimica Acta* **2000**, *45*, 1243-1247.

[175]   D. R. MacFarlane, F. Zhou, M. Forsyth, *Solid State Ionics* **1998**, *113*, 193-197.

[176]   C. A. Angell, *Annual Review of Physical Chemistry* **1992**, *43*, 693-717.

[177]   S. Seki, A. B. H. Susan, T. Kaneko, H. Tokuda, A. Noda, M. Watanabe, *Journal of Physical Chemistry B* **2005**, *109*, 3886-3892.

[178]   B. K. Wheatle, N. A. Lynd, V. Ganesan, *ACS Macro Lett.* **2018**, 1149-1154.

[179]   J. R. Dygas, B. Misztal-Faraj, Z. Floljanczyk, F. Krok, M. Marzantowicz, E. Zygadlo-Monikowska, *Solid State Ionics* **2003**, *157*, 249-256.

[180]   E. A. Jackson, M. A. Hillmyer, *ACS NANO* **2010**, *7*, 3548-3553.

[181]   S. Yoo, J.-H. Kim, M. Shin, H. Park, J.-H. Kim, S.-Y. Lee, S. Park, *Science Advances* **2015**, *e1500101*.

[182]   L. Zhao, Y. Zhang, L. B. Huang, X. Z. Liu, Q. H. Zhang, C. He, Z. Y. Wu, L. J. Zhang, J. Wu, W. Yang, L. Gu, J. S. Hu, L. J. Wan, *Nat Commun* **2019**, *10*, 1278.

[183]   F. Zhang, T. Liu, M. Li, M. Yu, Y. Luo, Y. Tong, Y. Li, *Nano Lett* **2017**, *17*, 3097-3104.

[184]   Y. Lin, X. Wang, G. Qian, J. J. Watkins, *Chemistry of Materials* **2014**, *26*, 2128-2137.

[185]   M. C. Orilall, U. Wiesner, *Chemical Society reviews* **2011**, *40*, 520-535.

[186]   J. Tang, T. Wang, R. R. Salunkhe, S. M. Alshehri, V. Malgras, Y. Yamauchi, *Chem. Eur. J.* **2015**, *21*, 17293-17298.

[187]   M. Stefik, S. Guldin, S. Vignolini, U. Wiesnerd, U. Steinere, *Chem Soc Rev* **2015**, *44*, 5076-5091.

[188]   Y. Fang, Y. Ni, S. Y. Leo, C. Taylor, V. Basile, P. Jiang, *Nat Commun* **2015**, *6*, 7416.

[189]   C. Li, N. S. Colella, J. J. Watkins, *ACS applied materials & interfaces* **2015**, *7*, 13180-13188.

[190] O. D. Velev, E. W. Kaler, *Advanced Materials* **2000**, *12*, 531-534.

[191] K. Hou, W. Ali, J. Lv, J. Guo, L. Shi, B. Han, X. Wang, Z. Tang, *J Am Chem Soc* **2018**, *140*, 16446-16449.

[192] J. Wei, Z. Sun, W. Luo, Y. Li, A. A. Elzatahry, A. M. Al-Enizi, Y. Deng, D. Zhao, *J Am Chem Soc* **2017**, *139*, 1706-1713.

[193] Y. Meng, D. Gu, F. Zhang, Y. Shi, H. Yang, Z. Li, C. Yu, B. Tu, D. Zhao, *Angew Chem Int Ed Engl* **2005**, *44*, 7053-7059.

[194] M. Zhang, L. He, T. Shi, R. Zha, *Chemistry of Materials* **2018**, *30*, 7391-7412.

[195] Y. Guo, B. G. P. van Ravensteijn, W. K. Kegel, *Macromolecules* **2019**.

[196] S. A. Johnson, P. J. Ollivier, T. E. Mallouk, *Science* **1999**, *283*, 963-965.

[197] T. Liu, F. Zhang, Y. Song, Y. Li, *J. Mater. Chem. A* **2017**, *5*, 17705-17733.

[198] Y. Deng, J. Wei, Z. Sun, D. Zhao, *Chem Soc Rev* **2013**, *42*, 4054-4070.

[199] Y. Zhai, Y. Dou, D. Zhao, P. F. Fulvio, R. T. Mayes, S. Dai, *Adv Mater* **2011**, *23*, 4828-4850.

[200] N. S. Ergang, J. C. Lytle, K. T. Lee, S. M. Oh, W. H. Smyrl, A. Stein, *Advanced Materials* **2006**, *18*, 1750-1753.

[201] A. Vu, Y. Qian, A. Stein, *Advanced Energy Materials* **2012**, *2*, 1056-1085.

[202] G.-R. Yi, J. H. Moon, S.-M. Yang, *Chem. Mater.* **2001**, *13*, 2613-2618.

[203] Y. Gai, D.-P. Song, B. M. Yavitt, J. J. Watkins, *Macromolecules* **2017**, *50*, 1503-1511.

[204] H. Fei, B. M. Yavitt, G. Kopanati, J. J. Watkins, *J. Polym. Sci., Part B: Polym. Phys.* **2019**, *57*, 691–699.

[205] Weiyin Gu, June Huh, SungWoo Hong, Benjamin R. Sveinbjornsson, Cheolmin Park, Robert Howard Grubbs, T. P. Russell, *ACS NANO* **2013**, *7*, 2551-2558.

[206] D. P. Song, C. Li, W. Li, J. J. Watkins, *ACS Nano* **2016**, *10*, 1216-1223.

[207] G. M. Miyake, V. A. Piunova, R. A. Weitekamp, R. H. Grubbs, *Angewandte Chemie* **2012**, *124*, 11408-11410.

[208] SungWoo Hong, Weiyin Gu, June Huh, Benjamin R. Sveinbjornsson, Gajin Jeong, Robert Howard Grubbs, T. P. Russell, *ACS Nano* **2013**, *7*, 9684-9692.

[209] A. L. Liberman-Martin, C. K. Chu, R. H. Grubbs, *Macromolecular rapid communications* **2017**, *38*, 1700058-1700073.

[210] J. Bolton, T. S. Bailey, J. Rzayev, *Nano letters* **2011**, *11*, 998-1001.

[211] R. Fenyves, M. Schmutz, I. J. Horner, F. V. Bright, J. Rzayev, *Journal of the American Chemical Society* **2014**, *136*, 7762-7770.

[212] L. Zhang, H. B. Wu, X. W. Lou, *Advanced Energy Materials* **2014**, *4*, 11.

[213] H. Fei, B. M. Yavitt, G. Kopanati, J. J. Watkins, *Journal of Polymer Science Part B: Polymer Physics* **2019**.

[214] X. Wang, R. D. Tilley, J. J. Watkins, *Langmuir* **2014**, *30*, 1514-1521.

[215] V. R. Tirumala, A. Romang, S. Agarwal, E. K. Lin, J. J. Watkins, *Advanced Materials* **2008**, *20*, 1603-1608.

[216] V. R. Tirumala, V. Daga, A. W. Bosse, A. Romang, J. Ilavsky, E. K. Lin, J. J. Watkins, *Macromolecules* **2008**, *41*, 7978-7985.

[217] V. K. Daga, E. R. Anderson, S. P. Gido, J. J. Watkins, *Macromolecules* **2011**, *44*, 6793-6799.

[218] V. K. Daga, J. J. Watkins, *Macromolecules* **2010**, *43*, 9990-9997.

[219] Y. Luo, B. Kim, D. Montarnal, Z. Mester, C. W. Pester, A. J. McGrath, G. Hill, E. J. Kramer, G. H. Fredrickson, C. J. Hawker, *Journal of Polymer Science Part A: Polymer Chemistry* **2016**, *54*, 2200-2208.

[220] M. J. B. Park, Joona; Harada, Tamotsu; Char, Kookheon; Lodge, Timothy P., *Macromolecules* **2004**, *37*, 9064-9075.

[221] Jarosław Paturej, Sergei S. Sheiko, Sergey Panyukov, M. Rubinstein, *Science Advances* **2016**, *2*, e1601478.

[222] Lewis J. Fetters, David J. Lohse, S. T. Milner, *Macromolecules* **1999**, *32*, 6847-6851.

[223] T. H. K. Thomas, T. C., *Journal of Polymer Science: Part A-2* **1969**, *7*, 537-549.

[224] N. Zheng, J. Hou, H. Zhao, J. Wu, Y. Luo, H. Bai, J. A. Rogers, Q. Zhao, T. Xie, *Adv Mater* **2019**, *31*, e1807326.

[225] X.-Y. Yang, L.-H. Chen, Y. Li, J. Claire Rooke, C. Sanchez, B.-L. Su, *Chem Soc Rev* **2017**, *46*, 481-558.

[226] H. Sai, K. Wee Tan, K. Hur, E. Asenath-Smith, R. Hovden, Y. Jiang, M. Riccio, D. A. Muller, V. Elser, L. A. Estroff, S. M. Gruner, U. Wiesner, *Science* **2013**, *341*, 530-534.

[227] Y. Zhu, S. Murali, M. D. Stoller, K. J. Ganesh, W. Cai, P. J. Ferreira, A. Pirkle, R. M. Wallace, K. A. Cychosz, M. Thommes, D. Su, E. A. Stach, R. S. Ruoff, *Science* **2011**, *332*, 1537-1541.

[228] J. Wang, S. Kaskel, *J. Mater. Chem.* **2012**, *22*, 23710.

[229] K. A. Cychosz, X. Guo, W. Fan, R. Cimino, G. Y. Gor, M. Tsapatsis, A. V. Neimark, M. Thommes, *Langmuir* **2012**, *28*, 12647-12654.

[230] G. M. Zhou, D. W. Wang, F. Li, L. L. Zhang, N. Li, Z. S. Wu, L. Wen, G. Q. Lu, H. M. Cheng, *Chemistry of Materials* **2010**, *22*, 5306-5313.

[231] I. H. Son, J. H. Park, S. Kwon, S. Park, M. H. Rummeli, A. Bachmatiuk, H. J. Song, J. Ku, J. W. Choi, J. M. Choi, S. G. Doo, H. Chang, *Nature Communications* **2015**, *6*, 8.

[232] B. Liang, Y. P. Liu, Y. H. Xu, *J. Power Sources* **2014**, *267*, 469-490.

[233] M. Ko, S. Chae, J. Ma, N. Kim, H. W. Lee, Y. Cui, J. Cho, *Nature Energy* **2016**, *1*.

[234] M. Winter, J. O. Besenhard, M. E. Spahr, P. Novak, *Adv. Mater.* **1998**, *10*, 725-763.

[235] E. Frackowiak, S. Gautier, H. Gaucher, S. Bonnamy, F. Beguin, *Carbon* **1999**, *37*, 61-69.

[236] T. B. Schon, B. T. McAllister, P. F. Li, D. S. Seferos, *Chemical Society Reviews* **2016**, *45*, 6345-6404.

[237] E. J. Son, J. H. Kim, K. Kim, C. B. Park, *J. Mater. Chem. A* **2016**, *4*, 11179-11202.

[238] N. Patil, A. Aqil, F. Ouhib, S. Admassie, O. Inganas, C. Jerome, C. Detrembleur, *Adv. Mater.* **2017**, *29*, 9.

[239] Z. Q. Zhu, M. L. Hong, D. S. Guo, J. F. Shi, Z. L. Tao, J. Chen, *J. Am. Chem. Soc.* **2014**, *136*, 16461-16464.

[240] A. Ahmad, Q. H. Meng, S. Melhi, L. J. Mao, M. Zhang, B. H. Han, K. Lu, Z. X. Wei, *Electrochimica Acta* **2017**, *255*, 145-152.

[241]   Z. Q. Luo, L. J. Liu, Q. Zhao, F. J. Li, J. Chen, *Angew. Chem.-Int. Edit.* **2017**, *56*, 12561-12565.

[242]   T. Liu, K. C. Kim, B. Lee, Z. M. Chen, S. Noda, S. S. Jang, S. W. Lee, *Energy Environ. Sci.* **2017**, *10*, 205-215.

[243]   K. Pirnat, G. Mali, M. Gaberscek, R. Dominko, *J. Power Sources* **2016**, *315*, 169-178.